HYBRID DIFFUSE OPTICS FOR TRANSLATIONAL ONCOLOGY AND NANOBIOPHOTONICS: TOWARDS A THERANOSTIC APPROACH FOR EMERGING CANCER THERAPIES

MIGUEL ADRIÁN MIRELES NÚÑEZ

Medical Optics Group

ICFO - Institut de Ciències Fotòniques
UPC - Universitat Politècnica de Catalunya

July 2018

SUPERVISOR:
Prof. Turgut Durduran

CO-SUPERVISOR:
Dr. Johannes Johansson

IN CLOSE COLLABORATION WITH:
Prof. Romain Quidant
Prof.. Oriol Casanovas

DECLARATION

I hereby declare that, except where specific reference is made to the work of others, the contents of this dissertation are original and have not been submitted in whole or in part for consideration to any other degree or qualification of this or any other university.

Barcelona, July 2018

Miguel Adrián Mireles Núñez

ABSTRACT

A pre-clinical mouse model of human clear cell renal cell carcinoma (ccRCC) was employed as a method to study the prognostic and theranostic potential of two, non-invasive, deep tissue, diffuse optical techniques, namely broadband diffuse reflectance spectroscopy (DRS) and diffuse correlation spectroscopy (DCS). In doing so, new algorithms and methods were developed to improve the robustness and applicability of the technology and a vision is presented for its clinical translation.

Hemodynamic biomarkers such as the total hemoglobin concentration (THC), blood oxygen saturation (SO_2) and blood flow (BFI) that were measured in a longitudinal and quantitative fashion from deep tissue layers (> 2 mm) were used to predict the outcome of an antiangiogenic therapy, Sunitinib therapy. Hemodynamic biomarkers were shown to be useful for treatment planning prior to the onset of the therapy and, at an early stage (few days), as predictors of the therapy outcome.

The second part of this work focused on another emerging class of treatments based on the nanobiophotonics as a complementary tool for improving other cancer therapies. The specific needs for the optimization of plasmon photo-thermal therapy based on customized gold nanorods was studied. Based on that, it was hypothesized that the combination of DCS and DRS would enable dose planning and *in vivo* on-line evaluation of the treatment effects. As a means to reach this goal, this work has shown that DRS/DCS can, estimate the *in vivo* PEGylated gold nanorod (AuNR-PEG) concentration and detect their accumulation and clearance from the tissues in a longitudinal manner. Furthermore, it was shown that the injection of AuNRs-PEG do not al-

ter the tumor hemodynamics and, that, had there been any alterations, we could monitor its effects.

All these studies were done with a contact probe which was previously validated but was also shown to cause some systematic effects. A proof-of-concept, scanning, non-contact system was developed and validated as a future tool to overcome these limitations.

Overall, this work contributed to bridge some of the gaps in translational oncology towards the development of personalized cancer therapies.

RESUMEN

La información hemodinámica de un modelo animal fue obtenida de manera no invasiva y longitudinal por medio de un sistema hibrido que combina las técnicas de espectroscopia de reflectancia y correlación difusa en una sonda de contacto; donde algunos de los factores que afectan la adquisición y el procesamiento de los datos fueron resueltos a través de un algoritmo desarrollado para este fin. Esta información fue obtenida en dos campos de investigación, la oncología traslacional y la nanobiofotónica.

En el campo de la oncología traslacional, la información hemodinámica fue monitoreada ‘opticamente durante la administración de terapia antiangiogénica, permitiendo predecir desde las mediciones previas al tratamiento, la resistencia intrínseca de los tumores al tratamiento. Además, se observó que los cambios en los parámetros hemodinámicos al día tres de iniciado el tratamiento están correlacionados con el pronóstico post-terapéutico. En el campo de la nanobiofotónica, los parámetros hemodinámicos y la concentración de nanotubos de oro funcionalizados (AuNRs-PEG) fueron cuantificados simultáneamente. Se demostró que la concentración de AuNRs-PEG estimada por medio de las tecnicas de optica difusa es proporcional a la obtenida por métodos comerciales para la cuantificación *ex vivo* de oro en tejidos. Además, la hemodinámica se mantuvo estable aun con AuNRs-PEG circulando en la sangre, demostrando que no hay interacción entre dichos parámetros.

De manera adicional, se introdujo la versión de no contacto de este sistema como un método potencial para la obtención de información hemodinámica en futuras aplicaciones.

En general, este trabajo contribuye a cubrir algunas de las necesidades en los campos de la oncología traslacional y la nanobiofotónica, con vistas al desarrollo de terapias teranosticas contra el cáncer.

CONTENTS

LIST OF FIGURES

LIST OF TABLES

ACRONYMS

CDE	Correlation diffusion equation
g_1	Normalized electric field autocorrelation function
g_2	Normalized intensity autocorrelation function
μ_a	Absorption coefficient
$\mu_s^{'}$	Reduced scattering coefficient
μ_s	Scattering coefficient
μ_{eff}	Effective attenuation coefficient
α	Fraction moving scatterers
D_b	Brownian diffusion coefficient
τ	Correlation time
g	Anisotropy factor
A_0	Reduced scattering coefficient at the reference wavelength
b	Scattering power
l_{tr}	Transport mean-free path
ρ^{DRS}	Source detector-separation for DRS technique
ρ^{DCS}	Source-detector separation for DCS technique
Φ	Photon fluence rate
D	Photon diffusion coefficient

S	Source power density
DE	Diffusion equation
R_{eff}	Effective reflection coefficient
β	Mode parameter
H_2O	water
Hb	Deoxyhemoglobin
HbO_2	Oxyhemoglobin
THC	Total hemoglobin Concentration
SO_2	Oxygen saturation
BFI	Blood flow index
MFP	Mean free path
DRS	Diffuse reflectance spectroscopy
DCS	Diffuse correlation spectroscopy
HAC	Hierarchical agglomerative clustering
LSPR	Localize Surface Plasmon Resonance
PEG	Polyethylene glycol
AuNRs-PEG	PEGylated gold nanorods
PPTT	Plasmon-based Photo-Thermal Therapy
SNR	Signal-to-Noise Ratio
S_r	Spatial resolution
MPS	Mononuclear phagocytic system

1 INTRODUCTION

My work spanned multiple disciplines and collaborations between institutions and has been focused on the development and application of two, non-invasive, deep tissue, diffuse optical techniques, namely broadband diffuse reflectance spectroscopy (DRS) and diffuse correlation spectroscopy (DCS) for pre-clinical research on treatments of clear cell renal cell carcinoma (ccRCC). DRS and DCS are near-infared light-based techniques capable of retrieving non-invasive, longitudinal and quantitative hemodynamic information, such as the total hemoglobin concentration (THC), blood oxygen saturation (SO_2) and blood flow (BFI) from deep tissue layers (> 2mm). Our group has previously developed a platform based on contact DRS/DCS [1, 2] and I have developed new, robust algorithms that are tuned for the research described in this monograph (Chapter 4). Furthermore, I have introduced the concept of a non-contact device which overcomes certain limitations of the existing approach and validated it in pilot studies (Chapter 7).

The induction of vascular changes in the tumor as a treatment [3] is one such important avenue [4, 5] where international research efforts are being carried out including those by our collaborators [5–8]. In this work, I have focused on pre-clinical othoxenograft clear cell renal cell carcinoma (ccRCC) mouse model which is a model utilized in our collaboration.

ccRCC is an important model to study and develop new strategies for clinical translation due to the typically late and incidental detection of ccRCC [9, 10]. The mainstream therapeutic approach for ccRCC is the radical or partial surgical resection of the kidney - nephrectomy - due to the large tumor volume; however, this approach is often times discarded since the tumor has already invaded the surrounding vital

organs (i.e liver) [11]. Chemotherapy is another therapeutic strategy [12–15], however, it only modestly improves the progression-free survival rate ($\approx$ 7%) due to drug resistance. Moreover, ccRCC is also resistant to radiation and weakly sensitive to immunotherapeutic agents, translating into a 40% of tumor relapse after surgical resection [10].

A newer approach for ccRCC treatment is based on the selective blockage of the tumor cell proliferation pathways [4, 16] by targetting the vascular endothelial growth factor (VEGF) [3, 17]. These antiangiogenic therapies aim to inhibit the formation of new vasculature - angiogenesis - in the tumor; creating a nutrient-depleted environment to eliminate the cancer cells. Among the multiple antiangiogenic drugs, Sunitinib [18, 19] has been successfully employed in pre-clinical models [20–22] and even translated to the clinics as the first-line of treatment for ccRCC [23] demonstrating an enhanced progression-free survival ($\approx$ 18%) in patients [24].

Even though these approaches have lead to an increase in the survival-rate, eventual tumor relapse has been observed due high rates of drug resistance. Further optimization of Sunitinib treatment is still needed to reduce the number of non-responding or poorly responding patients [8, 25] and I have studied the potential of DRS/DCS for pre-treatment planning and for early prognosis, i.e. the prediction of the outcome. Our studies (Chapter 5) have shown that DRS and DCS combination provide promising biomarkers for both purposes and further research may enable their clinical translation.

Another emerging class of treatments are based on the nanobiophotonics as a complementary tool for improving other cancer treatment strategies [26–28]. For our purposes, we have focused (Chapter 6) on the development of plasmon photo-thermal therapies (PPTT) [29] as a means to enhance the therapy-derived vascular changes; thus potentially leading to a more efficient treatment. PPTT works by applying a plasmonic agent to the region of interest and then delivering light (either non-invasively or invasively) to create local heating [30–32]. PPTT with gold nanoparticles [33], here explored for PEGylated

gold nanorods (AuNRs-PEG), is particularly interesting due to their enhanced light absorption at their localized surface plasmon resonance (LSPR). This effect turns them into efficient nanosources of heat for PPTT [29, 34]

PPTT with gold nanoparticles is still at its infancy. Their geometry, their surface chemistry and production methods should still be optimized but this is not the focus of this work. In parallel to these efforts, it is imperative to develop means for treatment planning, for example, to define the injection dose and the treatment light power density and duration. Our hypothesis is that the local tissue hemodynamics would provide a means to develop a model for dosimetry. The treatment light power density and duration are trickier and decades of photodynamic therapy (PDT) [35] and experience with DRS [36, 37], DCS [38] and DRS/DCS [39, 40] in that context has allowed us to hypothesize that on-line monitoring of tumor physiology before, during and after therapy could be critical.

I have introduced these methods into research on the same ccRCC models mentioned above and have demonstrated that DRS/DCS can estimate the peak *in vivo* AuNR-PEG concentration and detect their accumulation and clearance from the tissues in a longitudinal manner. Furthermore, I have shown that the injection of AuNRs-PEG do not alter the tumor hemodynamics and, that, had there been any alterations, we could monitor its effects.

Overall, this work has introduced and demonstrated a new approach for pre-clinical research on a relevant cancer model with a potential pathway for near-term clinical translation. The following chapters provide the physical background to diffuse optics, detail the instrumentation and the algorithms and showcase the key studies that I have conducted during my Ph.D. research.

2 LIGHT-TISSUE INTERACTIONS

In this work, light is used to quantitatively recover information about tissues including the chromophore concentrations (e.g water H_2O, oxy- HbO_2 and deoxy- Hb hemoglobin) and the blood flow (BFI) [41]. This information arise from the photon propagation and interaction with the biological tissue components. Those effects are modeled as a diffusive process [42, 43] governed by three main light-tissue interactions: **reflection**, **absorption** and **scattering**.

In general, when light is shone into a turbid media (e.g. biological tissue), photons will interact with the media [44, 45]. Some weakly interacting photons would get reflected outside from the tissue surface and escape to air. Others will enter the tissue and propagate through it, experiencing a strong interaction with the structures in the medium. Those photons can either be absorbed, scattered or both by the tissue components. Due to the multiple scattering events, some photons would be able to travel deep into the tissue before reaching its surface and escape. Those outcoming photons that have interacted with the tissue will carry quantitative information about the medium (Figure 2.1).

2.1 LIGHT-TISSUE ABSORPTION INTERACTION

Light absorption depends on the tissue constituent concentrations [42, 47]. The main absorbing components in tissue, in our wavelengths of interest, are the deoxy- (Hb) and oxy- (Hb) hemoglobin and water (H_2O), however, depending on the interrogated tissue type (e.g. breast), the lipid content may also become a relevant chromophore to be considered. The absorption spectrum of the above-mentioned main

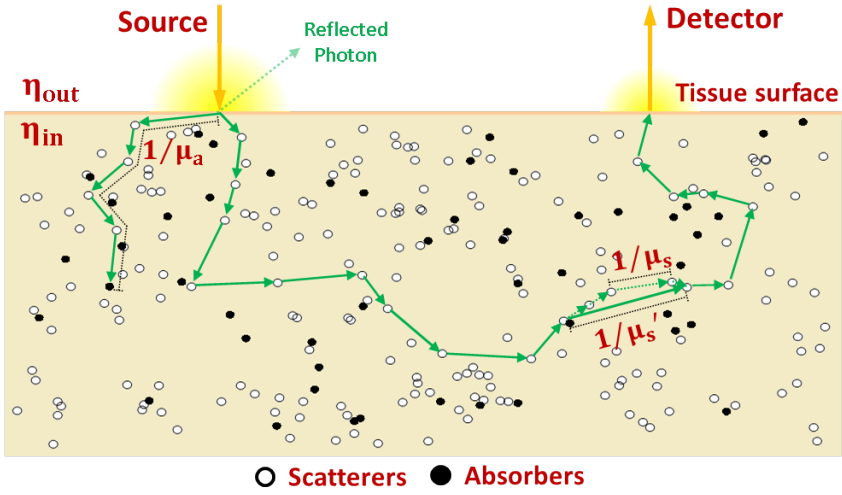

Figure 2.1: Light-tissue interactions. Photons launched into a turbid media might be reflected outside whereas some others might interact with the tissue scatterers (hollow circles) and absorbers (filled circles). The outcoming photons may carry information about the media. That information is given by the absorption (μ_a) and reduced scattering (μ_s') coefficients. This illustration is inspired by [46].

tissue chromophores presents a wavelength range, often referred as the "physiological window" [48], where their absorption coefficient is relatively low. This transparency window, shown in Figure 2.2, spans from 600-1000 nm, covering the NIR-IR region.

The light absorption depends on the relative absorption [cm^{-1}] or the molar extinction coefficient [cm^{-1} M^{-1}] of a given chromophore $\epsilon(\lambda)$ and its relative [%] or molar [M] concentration c respectively. The total light absorption at a given wavelength can be quantified through the absorption coefficient $\mu_a(\lambda)$ [cm^{-1}] as:

$$\mu_a(\lambda) = log(10) \cdot \sum_{i=1}^{n} \epsilon_i(\lambda) c_i \tag{2.1}$$

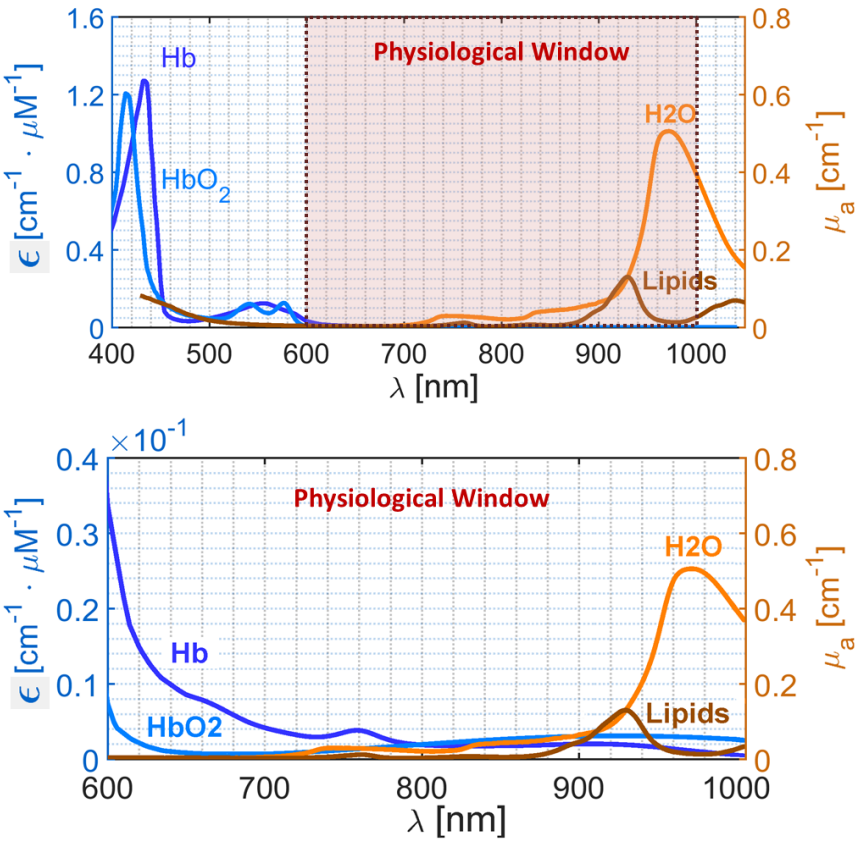

Figure 2.2: The physiological near-infrared window. The main tissue choromopores the deoxy- (Hb) and oxy- (HbO_2) hemoglobin (250 - 650 nm [49], 650 - 1042 nm [50, 51]) and the water (H_2O) [50] and lipids [52] exhibits a relatively low absorption band (600-1000 nm) in the NIR-IR region. This spectral band is often utilized for harvesting deep tissue information through diffusive light.

Representing the mean inverse length at which the propagated photons gets absorbed in tissue.

From the gathered light, the native tissue chromophore concentrations such as the Hb [μM] and HbO_2 [μM], the water [%] and lipids [%] can be computed [53]. Besides, the tissue hemodynamic parameters

such as the total hemoglobin concentration (THC [μM] = $Hb + HbO_2$) and tissue oxygen saturation ($SO_2[\%] = {}^{HbO_2}/_{(Hb+HbO_2)}$), can be inferred from the estimated chromophore concentrations.

2.2 LIGHT-TISSUE SCATTERING INTERACTION

Photons that enter the tissue undergo several directionality changes while propagating. Each of those changes is known as a scattering event and occur when the photon hits a biological structure and change its propagation angle. Therefore, it can be stated that the tissue structural characteristics define the light-tissue scattering interactions [54]. The distance traveled by a photon between each scattering event is known as the mean free path (MFP), and it is in the order of hundreds of μm. In this context, two scattering models - the Rayleigh and Mie scattering - have been proposed for describing such interactions [55].

The scattering process is modeled by an angular function, which is used to describe the probability distribution of the scattered photons. This function is known as the anisotropy factor $g = \langle cos\theta \rangle$, which represents the scattered photon probability distribution in terms of the average cosine of the scattering angle θ [56]. The closer to unity, the more probable it is for a photon to be scattered in the forward direction. In general, biological tissues exhibit anisotropy values ranging between 0.8 and 0.9 [57]. Due to this fact, biological tissue has been shown to adhere mainly to the Mie scattering approximation since it describes anisotropic scattering processes [55][1].

In general, the scattering coefficient (μ_s [cm^{-1}]) is defined as the inverse of the mean free path. We also define the reduced scattering coefficient ($\mu_s^{'}$ [cm^{-1}]) as

$$\mu_s^{'} = \mu_s(1 - g) \ . \tag{2.2}$$

1 The Rayleigh scattering explains mainly the isotropic part of the photon scattering, which is often negligible during the scattering processes in biological tissues

Representing the inverse length at which, the directionality of the photon propagation in tissue has been randomized due to the multiple scattering events. Since the light-tissue scattering interaction has been shown to be a wavelength dependent process, the reduced scattering coefficient can further be defined in terms of the Mie scattering model as:

$$\mu_s^{'}(\lambda) = A_0\Big(\frac{\lambda}{\lambda_0}\Big)^{-b} \tag{2.3}$$

where λ_0 represents a reference wavelength for normalization (785 nm in our case), and the A_0 term represents the reduced scattering coefficient at the reference wavelength. In addition, the transport mean free path ($l_{tr} = 1/\mu_s^{'}$ [cm^{-1}]) can be defined as an analogous to the mean free path.

2.3 PHOTON DIFFUSION EQUATION

The propagation of a recently entered photon in tissue presents a small directional dependence as introduced earlier. The biological tissue is assumed to be a highly scattering media (e.g. $\mu_s^{'} >> \mu_a$), hence the photon experience multiple scattering events while propagating. When the photon has traveled a distance beyond one transport mean free path ($l_{tr} = 1/\mu_s^{'}$) its directional dependence gets randomized, describing a diffusive process. Under this assumptions, the photon propagation can be modeled by an isotropic point source located at one l_{tr} distance inside the tissue while considering that the tissue is homogeneous and hence, scattering is rotationally symmetric. The radially expanding light from the isotropic source, can be modeled by the photon diffusion equation (DE) [58–60] as:

$$\nabla \cdot [D(r)\nabla\Phi(r,t)] - v\mu_a(r)\Phi(r,t) - \frac{\partial}{\partial t}\Phi(r,t) = -vS(r,t) \tag{2.4}$$

where the photon fluence rate [2] (Φ) [W cm^{-2}] represents the light power per area radially expanding outwards from an isotropic source located at (r,t), the source power density term (S) [W cm^{-3}] represents the total power per volume element propagating radially outwards from the same position and D(r) = $v/3(\mu_s'(r)+\mu_a(r))$ [cm^2 s^{-1}] is the photon diffusion coefficient [3].

The photon diffusion equation (Equation 2.4) describes the photon propagation in a turbid media (e.g. biological tissue) as a diffusive process. It relates the source power (S) to the fluctuations in the photon fluence rate (Φ) due to the intrinsic tissue optical properties.

2.3.1 *Source power types*

The source term in the above introduced photon diffuse equation (Equation 2.4) models the injected photons into the tissue. These photons are expected to interact with the tissue components and hence, when collected at a certain distance from the source location, they would carry quantitative information about the media. In this regard, several approaches have been explored for delivering light to the tissue, each of them constituting a different diffuse optical technique (Figure 2.3) aiming to recover the tissue hemodynamic information through the estimation of the optical properties of the probed media.

The time-domain method (Figure 2.3c) [62–65], also known as Time-Resolved Spectroscopy - TRS, utilize a narrow time pulsed laser ($\approx$ 100 ps) as a light source for injecting photons into the tissue. The detected signal at a certain distance from the source consists of a broadening pulse resolved over time. The slope of the collected pulse is linked

2 It can also be represented by the photon energy concentration $\Gamma(r,t)$, which is directly proportional to the photon fluence rate through $\Gamma(r,t) = v\Phi(r,t)$

3 It has been shown [61] that the photon diffusion coefficient D(r) can be simplified to $D(r) = v/3(\mu_s'+\mu_a) \approx v/3\mu_s'$. The transformed absorption-independent diffusion coefficient demonstrated better agreement with respect to the complete one between the Monte Carlo simulations and the diffusion theory.

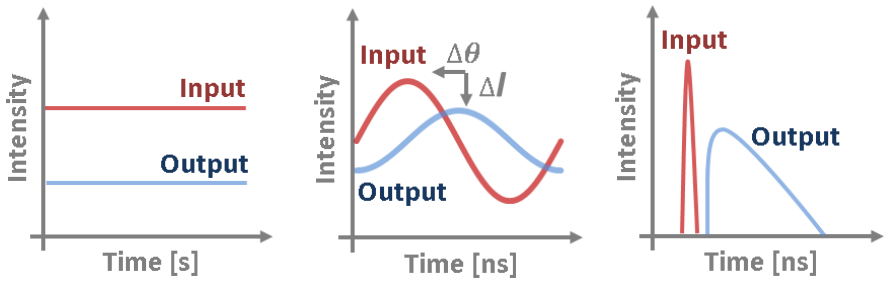

(a) Continuous-wave **(b)** Frequency-domain **(c)** Time-domain

Figure 2.3: Diffuse optical methods based on the source type. a) The CW technique measures the light intensity decay at a given distance; b) The frequency-domain technique measures the light intensity change and the phase-shift in frequency at a certain distance when using an intensity modulated light source; c) The time-domain technique measures the broadening over time of the collected signal at a given distance when a pulsed light is used as a source. This illustration is inspired by [41]

to the absorption coefficient of the medium due to the time-of-flight of the photon inside the tissue. The scattering coefficient would be responsible for the pulse intensity decay and broadening due to the multiple scattering events. In this manner, decoupling of the tissue optical properties is achieved.

In the frequency-domain method (Figure 2.3b) [66–70], commonly referred as Frequency-Domain Spectroscopy - FDS, an intensity modulated laser source between 100 MHz to 1GHz is employed for launching photons to the tissue. As a result, a diffusive wave oscillating at the same modulation frequency of the source would propagate inside the tissue. The detected signal at a certain distance from the source would then be modulated in intensity and frequency by the tissue optical properties. The tissue absorption coefficient would modify the intensity of the collected wave whereas the scattering coefficient would be linked to the phase shift of the signal with respect to the original light source frequency modulation. By identifying both features, the disentanglement of the tissue optical properties is achieved.

On the other hand, continuous-wave method (Figure 2.3a) [71–75], also known as steady-state spectroscopy or diffuse reflectance spectroscopy - DRS, utilize a continuous-wave source for illuminating the tissue. The detected signal at a certain distance from the source would be intensity decreased due to the combined effect of both the absorption and scattering coefficients. Therefore, the continuous-wave technique measures the effective attenuation coefficient $\mu_{eff} = \sqrt{3\mu_s'\mu_a}$, often called k or k_r, where the optical properties of the medium appear linked in a multiplicative fashion; thus, decoupling the contribution of each optical property to the decrease in intensity is not possible to achieve. To overcome this limitation, the spectral shape of the collected intensity is resolved when employing a broadband light source. In this manner, the light intensity decay can be spectrally associated to the absorption coefficient of the tissue components times their concentration, whereas the scattering coefficient can be modeled by the Mie scattering approximation. In this form, the contributions of the absorption and scattering coefficients to the intensity decrease at a certain distance can be decoupled.

The estimation of the tissue hemodynamics through any of the above listed diffuse optical methods is of great interest for monitoring and assessing the performance of novel therapeutic approaches, in particular in the translational oncology and nanobiophotonics fields. However, most of the research in those fields is carried out on pre-clinical mouse models due to their genetic similarities with humans [76, 77] that allows the translation of the recovered results into human therapeutic approaches. In this work, a pre-clinical clear cell renal cell carcinoma (ccRCC) orthoxenograft mouse model is utilized to evaluate the tissue hemodynamic changes as a response to cancer therapeutic approaches. These types of pre-clinical models are being particularly challenging due to the requirement of short detection distances (between 0.2 to 0.5 cm) for collecting optical data from the implanted tumors, which usual size is about 1 cm^3.

In this regard, although the TRS and FDS techniques collect a higher amount of information with respect to the continuous wave device, and therefore are more suitable to discern between the absorption and scattering contributions, their application in a pre-clinical mouse model turns to be hindered. The fact of acquiring optical information at short source-detector separations limits the capacity of both techniques to quantify accurately the pulse broadening and the phase-shift with respect to the original signal, respectively. Hence providing unreliable results about the probed tissue hemodynamics. To overcome this issue, costly and bulky instrumentation can be employed for increasing the electronics sensitivity to such a small signal changes; nevertheless, portability and affordability features might not be addressed.

In contrast, the continuous-wave spectroscopy technique (from now on referred as DRS technique) does not suffer from any of these limitations since it based on the light intensity decay information. Given the fact that this parameter at any wavelength decays exponentially over distance, the intensity variations even at short source-detector separations result suitable to be detected albeit with relative complexity in the data post-processing. In addition, its instrumentation turns out to be simple and inexpensive.

Based on those reasons, in this work the employment of a DRS approach represents as a suitable solution for our purposes. In the following sections, the solution to the photon diffuse equation under the assumption of a DRS approach, would be introduced.

2.3.2 *Boundary conditions*

In our case, the data acquisition is based on the collection of back-reflected light from the tissue. Hence, a realistic tissue geometry to consider is the planar interface as shown in Figure 2.4. In this geometry, a semi-infinite turbid tissue with a refractive index n_{in} spans to infinity in the x-y plane, and from z = 0 to infinity in the z-direction. The tissue is bounded on the top part by a different media, commonly

air, with a different refractive index (n_{out}). Here, the z = 0 value represents the interface between both media.

Due to multiple scattering events, some photons would be able to reach the tissue surface and be scattered back into the tissue due to the index of refraction mismatch. Some others would escape from the tissue to the external media and will never re-enter. Thus, boundary conditions are needed to be taken into account to model those effects [78, 79]. To this end, the fluence rate (Φ) is Taylor expanded to the first order around the boundary (z = 0) in the so-called extrapolated-zero boundary condition [78].

$$\Phi(z) = \Phi(0) + \frac{\partial \Phi}{\partial z} z = \Phi(0) + \frac{\partial \Phi(0)}{\partial z} z \xrightarrow{z = -z_b} \Phi(z = -z_b) = 0 \quad (2.5)$$

This expansion results into a zero-crossing point for the fluence rate located at a distance z_b outside the tissue. This distance is given by

$$z_b = 2D \cdot \left(1+R_{eff}/1-R_{eff}\right) \quad (2.6)$$

where the effective reflection coefficient R_{eff} accounts for the index of refraction mismatch between the tissue and air, hence modeling photons that would be reflected outwards and inwards the tissue.

$$R_{eff} \approx -1.440 \cdot \left(n_{in}/n_{out}\right)^{-2} + 0.710 \cdot \left(n_{in}/n_{out}\right)^{-1} + 0.0636 \cdot \left(n_{in}/n_{out}\right) + 0.668 \quad (2.7)$$

The inclusion of the extrapolated-zero boundary condition (Equation 2.6) provides the feasibility to use the method of images to obtain an analytical solution to the photon diffusion equation. In this method, the detected light arise from the superposition of a virtual isotropic source and a virtual sink. The virtual source would be located at one transport mean free path inside the medium ($z = l_{tr}$). The sink would be placed at a distance $z = -(2z_b + l_{tr})$ outside the tissue as shown in Figure 2.4.

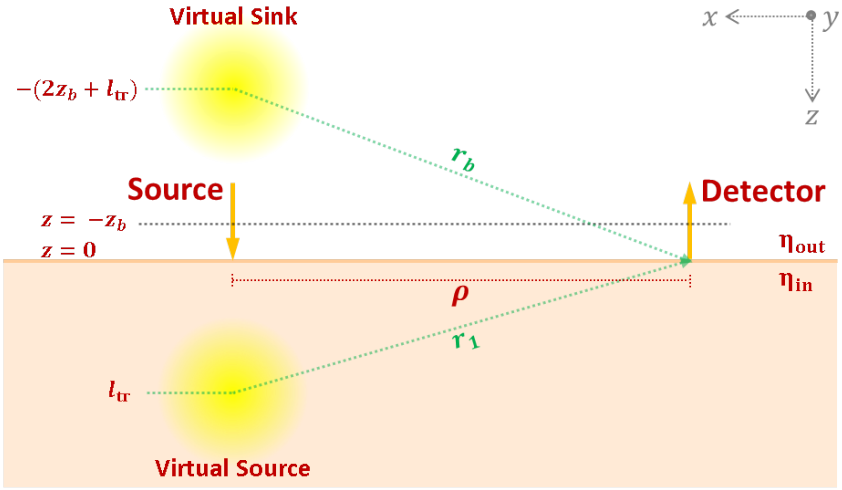

Figure 2.4: Extrapolated zero-bounday condition in a semi-infinite geometry. Photons injected by a real source placed at the tissue surface (z = 0) that propagates inside a turbid media and that are detected at a ρ distance, are modeled as a diffusive process. To this end a virtual isotropic light source is placed at $z = l_{tr}$ distance inside the medium and a virtual sink is located at a distance $z = -(2z_b + l_{tr})$ outside the medium. The placement of both virtual images satisfies the zero crossing point $z = -z_b$ condition. The virtual source-detector separations are given by the distances r_1 and r_b. This illustration is inspired by [80].

2.3.3 *Diffuse reflectance spectroscopy*

The diffusion equation (DE) (Equation 2.4) in a homogeneous media can be written in the form

$$\hat{A}\Phi(r,t) = -\frac{vS(r,t)}{D(r)} \tag{2.8}$$

where $\hat{A} = \nabla^2 + \partial/\partial t - v\mu_a$.

In the DRS scenario, no variations in the fluence rate ($\Phi(r,t)$) over time are assumed. Moreover, when assuming a semi-infinite geometry, the fluence rate must fall to zero when r tends to infinity due to light losses derived from multiple scattering and absorption events. To address this conditions, the term $\hat{A}\Phi(r,t)$ is integrated over time [81]. This integral represents an overdamped spherical wave radiating from a single intensity point source located at r.

Under these assumptions, the solution to Equation 2.4 can be derived from its Green's function [82, 83]. Nevertheless, such solution must satisfy the extrapolated-zero boundary condition (Section 2.3.2). Therefore, the Green's function solution $G(\lambda, \rho^{DRS})$ to the photon diffusion equation for a given light wavelength (λ) at a given source-detector separation (ρ^{DRS}) is depicted as the superposition of the virtual source and sink images of the real source [41] as shown in Figure 2.4.

$$G(\lambda, \rho^{DRS}) = \frac{v}{4\pi D}\left[\frac{exp(-k(\lambda)r_1)}{r_1} - \frac{exp(-k(\lambda)r_b)}{r_b}\right] \tag{2.9}$$

with

$$k(\lambda) = \sqrt{3\mu_s^{'}(\lambda)\mu_a(\lambda)}$$
$$r_1 = \sqrt{(z - l_{tr})^2 + \rho^2}$$
$$r_b = \sqrt{(z + 2z_b + l_{tr})^2 + \rho^2}$$

Equation 2.9 represents the spatial exponential decay of light at a given wavelength (λ) that propagates in a medium with specific optical properties $\mu_s^{'}(\lambda)$ and $\mu_a(\lambda)$. Here, the term $k(\lambda)$ represents the previously introduced effective attenuation coefficient, whereas the terms r_1 and r_b denotes the distances from the virtual source and sink images

to the detector respectively when the real isotropic source is located at position $z = 0$ [4].

2.4 CORRELATION DIFFUSION EQUATION

Beyond the static information addressed from the diffuse propagated photons in tissue, the dynamic information is also accessible from the same diffusing light. In general, when coherent light is shine to a diffusive medium (e.g. biological tissue), the scattering particles that compose it develop and emit light fields in all directions which intensity is feasible to be detected. However, since tissue is composed by moving scatterers - mainly the red blood cells (RBC) -, speckles are formed at the tissue surface due to the interference of light caused by the changes in the photon path lengths derived from the particles movement; hence creating relative light phase shifts. As a result, intensity fluctuations are recovered at the detector and provide access to the tissue dynamic information through the computing of the electric field temporal autocorrelation function.

In this context, dynamic light scattering (DLS) measurements [84–86] of a single or few scattering events (i.e. laser doppler flowmetry (LDF) [87–89]) can provide information about the tissue blood flow; however, the recovered information would be limited to superficial tissues (< 1 mm). On the other hand, the multiple scattering approach envision the propagation of the electric field autocorrelation function through the medium in each scattering event; thus providing deep tissue information (> 2mm). These interactions can be modeled as a diffusive process, analogous to the DE, through the correlation diffusion equation CDE [90–92].

4 Location $z = 0$ represents the tissue-air interface. A $z > 0$ value represents the light source located inside the tissue. A $z < 0$ refers to the source placement above the tissue surface.

$$\big[-\nabla \cdot (D)\nabla + v\mu_a + \frac{1}{3} v\mu_s' k_0^2 \alpha \langle \Delta r^2(\tau) \rangle \big] G_1(r,\tau) = vS(r) \qquad (2.10)$$

Here the term $k_0 = {}^{2\pi}/_{\lambda}$ refers to the wavenumber inside the medium. The $\langle \Delta r^2(\tau) \rangle$ term represents the mean-square displacement of the moving scatterers over the correlation time (τ) whereas α represents the fraction of these scatterers in tissue.

The CDE (Equation 2.10) differs from the DE in the inclusion of the term $k_0^2 \alpha \langle \Delta r^2(\tau) \rangle$ which accounts for the light decorrelation due to the dynamics of the medium. In this regard, the term D_b [$cm^2\ s^{-1}$] has been recently described in the literature [93–96] to be better described by the shear-induced diffusion of the main moving scatterers in tissue, the red blood cells (RBCs).

2.4.1 *Diffuse correlation spectroscopy*

Following similar steps as the diffusion equation (Section 2.3), a Green's function solution to the CDE (Equation 2.10) for a semi-infinite geometry is given by:

$$G_1(\rho^{DCS}, \tau) = \frac{v}{4\pi D} \Big(\frac{exp[-K(\tau) r_1]}{r_1} - \frac{exp[-K(\tau) r_b]}{r_b} \Big) \qquad (2.11)$$

where the decorrelation term $K(\tau) = \sqrt{3\mu_s'\mu_a + 6k_0^2 \mu_s'^2 \alpha D_b \tau}$ represents the dynamic information of the medium and the distances r_1 and r_b are similar those defined in Section 2.3.3.

Equation 2.11 describes the dynamics of the medium through the temporal electric field autocorrelation function G_1 at a given correlation time (τ) detected at a ρ^{DCS} distance from the light source. Nevertheless, it is experimentally challenging to measure the electric field. Instead, detectors are able to measure the unnormalized intensity autocorrelation function (G_2) which can be defined as:

$$G_2 = \langle I(r,t)\rangle \cdot \langle I(r,t+\tau)\rangle \tag{2.12}$$

The measured unnormalized electric field (G_1) and the unnormalized intensity autocorrelation function (G_2) are linked through the Siegert relation [97]

$$G_2 = \langle I\rangle^2 + \beta|G_1|^2 \tag{2.13}$$

where $\beta \approx 0.5$ is a system-dependent constant that is affected by the number of detected speckles through a single-mode fiber, the laser stability and coherence length [46, 98–100]. Furthermore, by taking advantage of the knowledge about the β parameter, estimated from the early values of the autocorrelation function ($\lim_{\tau\to 0}$), the normalized intensity autocorrelation function can be calculated. The normalized electric field (g_1) and intensity (g_2) autocorrelation functions can be defined similarly. The Siegert relation can then further be define analogous to the unnormalized versions to link both normalized autcorrelation functions as:

$$g_2 = 1 + \beta|g_1|^2 \tag{2.14}$$

Following this line, the solution to the CDE can be defined as:

$$g_1(\rho^{DCS},\tau) = \frac{\left(\frac{exp[-K(\tau)r_1]}{r_1} - \frac{exp[-K(\tau)r_b]}{r_b}\right)}{\left(\frac{exp[-K(\tau=0)r_1]}{r_1} - \frac{exp[-K(\tau=0)r_b]}{r_b}\right)} \tag{2.15}$$

2.5 MODELING THE DIFFUSE OPTICAL TECHNIQUES IN THE SEMI-INFINITE MEDIUM APPROACH

The theoretical solutions to the steady-state diffuse reflectance (Equation 2.9) and correlation spectroscopies (Equation 2.15) have been de-

fined in Sections 2.3.3 and 2.4.1 respectively. Both equations are modeled by a set of parameters (ρ,μ_a,$\mu_s^{'}$ and D_b) that described the theoretical forward model solution. In this section the impact of each of those parameters on the corresponding diffuse optical technique will be explored.

2.5.1 *Diffuse reflectance spectroscopy*

The theoretical diffuse reflectance in the continuous-wave (also known as steady-state) approach exhibits and spatial and spectral dependence. The spatial dependence is related to the source-detector separation ρ^{DRS} (Figure 2.5a), where for longer distances the reflected light intensity decay exponentially. This behavior can be explained by the increased probability for a further propagated photon to be absorbed due to multiple scattering events. The spectral dependence is given by the absorption (μ_a) and scattering ($\mu_s^{'}$) coefficients of the turbid media (e.g. biological tissue) represented in a manifold of wavelengths by the absorption spectrum of each tissue chromophore (Equation 2.1) and the Mie scattering approximation (Equation 2.3) respectively.

The primary tissue chromophores are the oxy- (HbO_2) and deoxy- (Hb) hemoglobin and water (H_2O), thus in the steady-state approach, changes in the absorption coefficient (μ_a) may arise from variations in the concentration of those chromophores (Figure 2.5). The spectral changes due to the Hb content mainly contribute to spectral changes in the short wavelength range ($\approx$ 650 - 800 nm). Nevertheless, a significant contribution over the whole reflectance spectrum is observed (Figure 2.5b). On the other hand, spectral variations due to changes in the HbO_2 concentration are mainly affecting the long wavelength range ($\approx$ 800 - 1000 nm), although the reflectance spectrum at the short wavelength gets also affected (Figure 2.5c). The aforementioned spectral variations may be explained by the spectral features of the hemoglobin composites along the whole physiological window. Regarding the H_2O changes, its primary effect is observed at the spectral

range spanning from 800 - 1000 nm (Figure 2.5d) due to the weak absorption features along the shorter wavelengths (≈ 600 - 800 nm).

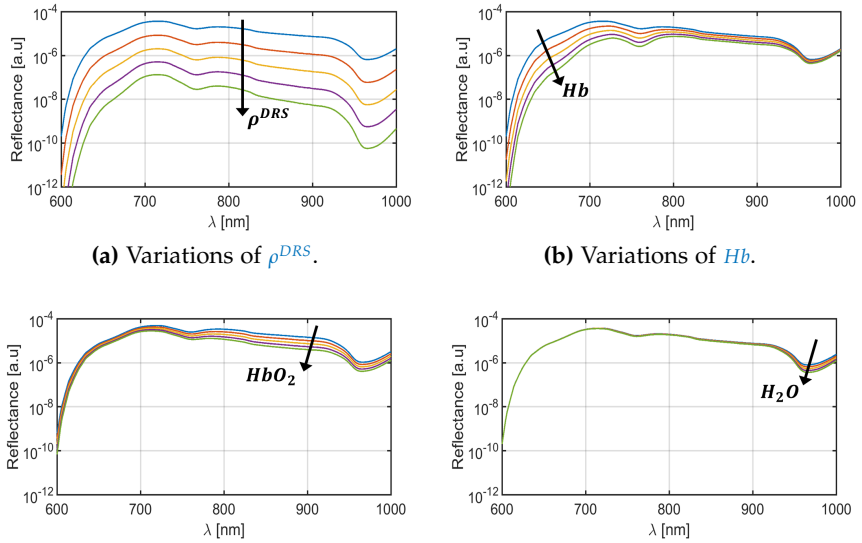

(a) Variations of ρ^{DRS}. **(b)** Variations of Hb.

(c) Variations of HbO_2. **(d)** Variations of H_2O.

Figure 2.5: Spatial dependence and spectral variations in the reflectance signal due to changes in the absorption coefficient: a) Varying the source-detector separation between 2.5 cm to 4.5 cm in steps of 0.5 cm; b) Varying the deoxy- hemoglobin content between 20 μM to 60 μM in steps of 10 μM; c) Varying the oxy- hemoglobin content between 60 μM to 100 μM in steps of 10 μM and d) Varying the water content between 70% to 90% in steps of 5%.

Furthermore, the oxy - HbO_2 and deoxy - Hb hemoglobin are linked to the tissue hemodynamic parameters through the total hemoglobin concentration (THC $[\mu\text{M}] = Hb + HbO_2$) and the tissue oxygen saturation ($SO_2[\%] = {}^{HbO_2}/_{(Hb+HbO_2)}$) parameters. Therefore variations in any of the hemoglobin components might affect the tissue hemodynamic parameters and hence the spectral shape of the collected reflectance spectrum (Figure 2.6).

In this regard, changes in the total hemoglobin content (THC) might have a global impact in the reflectance intensity (Figure 2.6a), due to the higher amount of blood and therefore increased tissue absorption. On the other hand, variations in the tissue oxygen saturation (SO_2) (Figure 2.6b) may have an impact mainly on the short wavelength range ($\approx$ 600 - 800 nm). However, variations at the long wavelengths might be significant depending on the blood content.

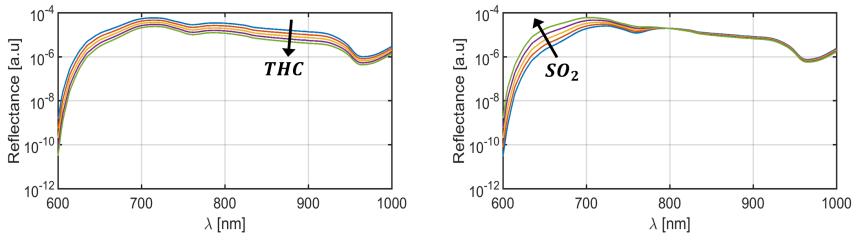

(a) Variations of THC content. **(b)** Variations of SO_2 content.

Figure 2.6: Spectral variations due to changes in the tissue hemodynamics: a) Varying the THC content between 80 μM to 120 μM in steps of 10 μM; b) Varying the SO_2 content between 70% to 90% in steps of 5%.

The reduced scattering coefficient (Equation 2.3), approximated by the Mie scattering model, is composed by the scattering coefficient (A_0) and the scattering power (b). Thus, spectral changes in the reflectance spectrum due to the variations on the scattering coefficient (Figure 2.7) are explained by the parameters mentioned earlier.

An increment in the scattering coefficient (Figure 2.7a) would be observed as a reflectance intensity reduction due to the increase of scattering events experienced by a photon while propagating. On the other hand, the variations in the scattering power coefficient (Figure 2.7b) have few impacts in the spectral shape of the reflectance mainly due to the homogeneous assumption of the media and hence minimum structural variations.

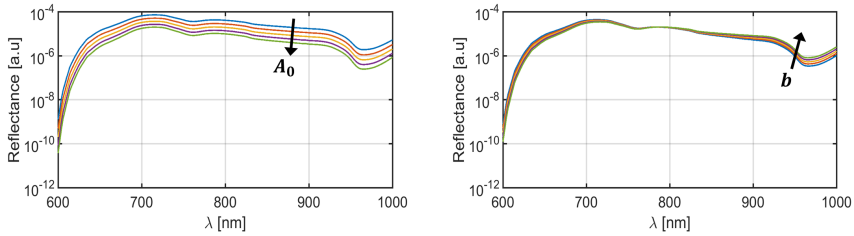

(a) Variations of A_0 parameter.

(b) Variations of b parameter.

Figure 2.7: Spectral variations due to changes in scattering coefficient: a) Varying the A_0 parameter between 8 cm^{-1} to 12 cm^{-1} in steps of 1 cm^{-1}; b) Varying the b parameter between 0.4 [a.u] to 1.2 [a.u] in steps of 0.2 [a.u].

2.5.2 *Diffuse correlation spectroscopy*

The normalized intensity autocorrelation function (Equation 2.15) in a turbid media (e.g. biological tissue) gets altered due to changes in the ρ^{DCS}, $\mu_s^{'}$, μ_a and D_b parameters. Since this technique makes use of a single wavelength light source, the here referred optical properties estimated by the steady-state diffuse reflectance spectroscopy, are those at the same source wavelength. Therefore, they are subjected to the changes mentioned above (Section 2.5.1) due to the multiple parameters that intervene in their building (Equation 2.1 and Equation 2.3).

In this section, the global changes (arising from any variation source) in each of the optical properties coefficients are explored and presented in Figures 2.8a and 2.8b.

Variations in the absorption coefficient will cause, on average, shorter interaction time of the photons with the medium. Therefore the collected signal would arise mainly from the less interacting photons with the tissue, which are those that have traveled shorter distances. Those photons correspond to the superficially propagated photons showing longer correlation times (Figure 2.8a), although their dynamic information would be related mostly to the superficial tissue layers. On

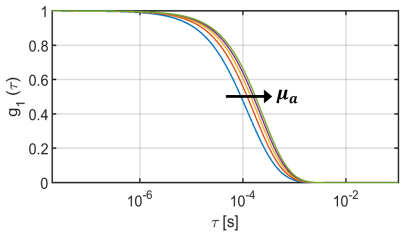

(a) Variations of μ_a parameter.

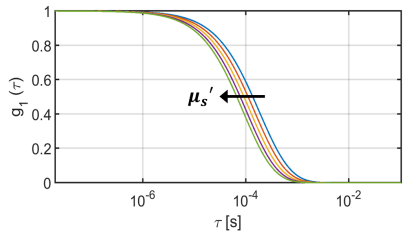

(b) Variations of $\mu_s^{'}$ parameter.

Figure 2.8: Variations in the normalized intensity autocorrelation (g_1) due to changes in the absorption and scattering coefficients: a) Varying the μ_a parameter between 0.01 cm^{-1} to 0.09 cm^{-1} in steps of 0.02 cm^{-1}; b) Varying the $\mu_s^{'}$ parameter between 8 cm^{-1} to 12 cm^{-1} in steps of 1 cm^{-1}.

the other hand, changes in the reduced scattering coefficient cause a more significant amount of scattering events. Therefore, photons spend more time on average into the medium and decorrelates at short time periods (Figure 2.8b). However, their dynamic information is related mainly to the deeper tissue layers due to multiple scattering events.

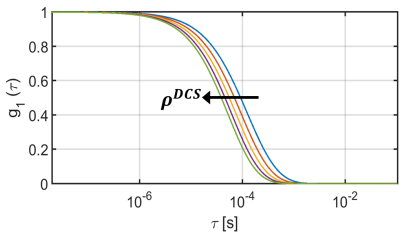

(a) Variations of ρ^{DCS} parameter.

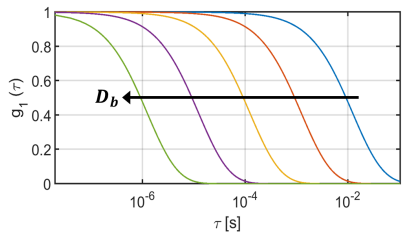

(b) Variations of D_b parameter.

Figure 2.9: Variations in the normalized intensity autocorrelation (g_1) due to changes in the source-detector separation and flow terms: a) Varying the ρ^{DRS} parameter between 2.5 cm to 4.5 cm in steps of 0.5 cm; b) Varying the D_b parameter between 1 x 10^{-12} cm^2 s^{-1} to 1 x 10^{-8} cm^2 s^{-1} in steps of 0.25 x 10^{-8} cm^2 s^{-1}.

When increasing the source-detector separation ρ^{DCS}, the intensity autocorrelation function g_1 tends to decorrelates faster (Figure 2.9a) due to the increased average time spent by a photon into the media. This effect is analogous to the above-mentioned increase in the reduced scattering coefficient. In addition, variations in the D_b parameters results into earlier decorrelation times (Figure 2.9b) due to an increase in the dynamics of the probed medium. In biological tissues, those dynamic changes arise mainly from the blood flow index (BFI $= \alpha D_b$).

3

CONTACT HYBRID DEVICE: INSTRUMENTATION & DATA COLLECTION

In the last decades, continuous-wave broadband diffuse reflectance spectroscopy (DRS) devices for measurements on small animals have been designed based on the original principal by Wilson et. al. [101]. These type of devices have been validated to accurately recover the optical properties of the probed media [71, 102]. Besides, broadband DRS devices have been applied for acquiring tissue hemodynamic information *in vivo* from pre-clinical [36, 103–106] and human [107, 108] models. More recently, hybrid devices combining broadband diffuse reflectance and correlation spectroscopies (DRS/DCS) have been employed for accessing both the static and dynamic tissue hemodynamic information from the probed volume in several applications [109–111]. In this chapter, a contact hybrid broadband DRS/DCS device developed by Farzam et. al. [1] for retrieving optical data at short source-detector separations (< 0.5 cm) from small animals is described. In this work, this device is employed for acquiring information from a pre-clinical orthoxenograft mouse model of clear cell renal cell carcinoma (ccRCC).

3.1 INSTRUMENTATION

The hybrid DRS/DCS system (Figure 3.1) combines both techniques into a contact hand-held probe for data collection. The medium is assessed by physical contact with the probe at the surface. A detailed description of the system is presented in the following sections.

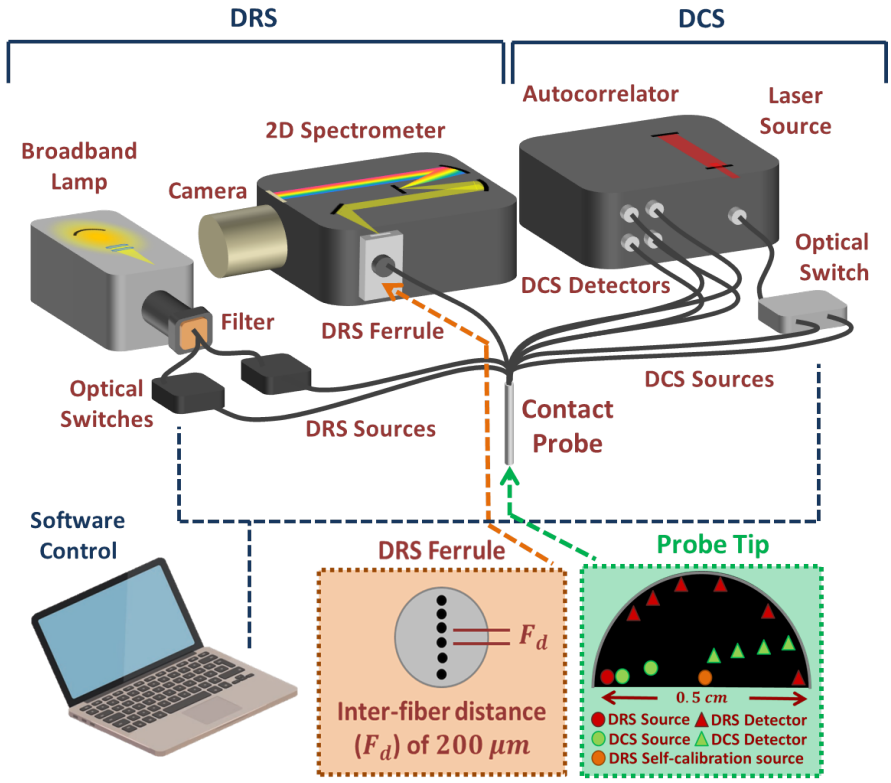

Figure 3.1: Hybrid DRS/DCS system and probe. The light is delivered to the tissue through the corresponding source fibers of each technique and collected in a multi-distance scheme from by the corresponding detection fibers. The detected light is processed by the corresponding device (either the two-dimensional spectrometer for DRS technique or the autocorrelator board for the DCS technique) for recording the data. The post-processing of the optical data is performed for obtaining the tissue optical properties, directly linked to the tissue hemodynamic information. The probe tip (green square) shows the distribution of the sources and detectors. For further details see [1]

3.1.1 *Diffuse reflectance spectroscopy system*

The DRS system consists of a broadband continuous lamp (QTH source model 66499, lamp model 6334NS, Oriel Instruments, Newport Corporation, USA) as a source of light. The outcoming light is filtered by a long-pass filter (FSQ-OG515, Newport Corporation, USA) to avoid second order diffraction light from wavelengths below the 500 nm. The filtered light is coupled to a multi-mode 400 μm core 2-Fiber Y-Bundle (BFY400HS02, Thorlabs GmbH, Germany) for guiding the light to a set of two software-controlled optical switches (SH-200-55-550,OZ Optics, Canada). Each optical switch output is plugged to a multi-mode 400 μm core fibers (FG365LEC NA = 0.22, Thorlabs GmbH, Germany). These two fibers are embedded into a pen-like probe with a semicircular tip shape (Figure 3.1) and employed as sources. The light is delivered to the media at two strategic positions:

1. The main source at the edge of the planar side of the probe (red dot in Figure 3.1)
2. The calibration source at the center of the planar side of the probe (yellow dot in Figure 3.1)

A set of six multi-mode 400 μm core fibers (WF200/220/245, NA = 0.28, CeramOptec GmbH, Germany) are located at the circumference of the probe tip for collecting the backscattered light (red triangles in Figure 3.1). When the light is delivered through the main source position, the detection fibers are located at distances (ρ^{DRS}) ranging from 0.25 to 0.5 cm. When light is injected into the tissue through calibration source position, the detection fibers are located equidistant at 0.25 cm. This configuration allows us to further account for the light emission and collection efficiency among fibers for self-calibrating the system.

The end tip of the detection fibers consists of a ferrule that sorts them into a linear array (orange square in Figure 3.1). The inter-fiber

separation is of 200 μm. The ferrule is plugged and aligned to the entrance slit of a two-dimensional spectrometer (Acton InSight-EFP, Princeton Instruments, USA). Once inside the spectrometer, the light from each collection fiber is decomposed into its wavelength components utilizing a 150 $^{grooves}/_{mm}$ diffraction grating and imaged by a CCD camera (PIXIS: 400B-eXcelon, 1340 x 400 pixels, Princeton Instruments, USA). These specifications allow us to obtain a multi-distance and multi-wavelength image with a 5 nm and 500 μm spectral and a spatial resolution respectively. The inter-fiber separation (200 μM) guarantees inter-signal crosstalk of less than 1%, over the whole wavelength range (λ) from 550 to 1050 nm. For details of the set-up and the reasoning for the arrangement of the fibers see [1].

3.1.2 *Diffuse correlation spectroscopy system*

The DCS device employs a 785 nm long coherence length (meters) laser as a light source (DL785-120-SO, 120mW, CrystaLaser, USA). The outcoming light from the laser is coupled to a multi-mode 400 μm core fiber (FG365LEC NA = 0.22, Thorlabs GmbH, Germany), which is plugged to the input of a software controlled 1x3 (one input, three outputs) optical switch (FSM-1by3, Piezosystem Jena, USA). For our purposes, only two outputs of the optical switch are employed. Each of the two selected outputs, are connected to a multi-model 400 μm core fiber (FG365LEC NA = 0.22, Thorlabs GmbH, Germany). These two fibers are then employed as light sources at two different locations (green circles in Figure 3.1) for reaching a multi-distance detection scheme equivalent to DRS. The output power of each fiber is attenuated with a 6 dB attenuator to deliver $\approx$ 30 mW light power to the tissue.

A set of four single-mode 5.6 μm core fibers (SM800-5.6-125, Thorlabs GmbH, Germany) are employed for collecting multi-distance back scattered coherent light from the tissue. These fibers are plugged into a four-channel custom built DCS system. This device employs a sin-

gle photon counting avalanche photodiode (SPCM-AQRH-14, Excelitas Technologies, USA) as a detector per each channel. The output is fed into a correlator board (Correlator.com, New Jersey, USA) to obtain a normalized intensity autocorrelation function (g_2) from each channel. When using the first source location, four source-detector separations ranging from 0.39 to 0.5 cm are achieved. By using the second source location, another set of four source-detector separations ranging from 0.25 to 0.36 cm are obtained. Therefore, a total of eight source-detector separations ranging from 0.25 to 0.5 cm are addressed, which overlaps with the DRS source-detection separations.

3.2 DATA COLLECTION

The DRS and DCS data acquisition is software controlled and performed in a tandem fashion. The control software synchronizes the switch on and off of the proper light source depending on the data type to be acquired (DRS or DCS). By activating the corresponding optical switch, the light is delivered to the tissue at the desired location through the corresponding source fiber. In addition, the software selects the device to be employed for capturing data, either the spectrometer (e.g. DRS data) or the autocorrelator device (e.g. DCS data). A schematic describing the timing for the data acquisition of both techniques is shown in Figure 3.2.

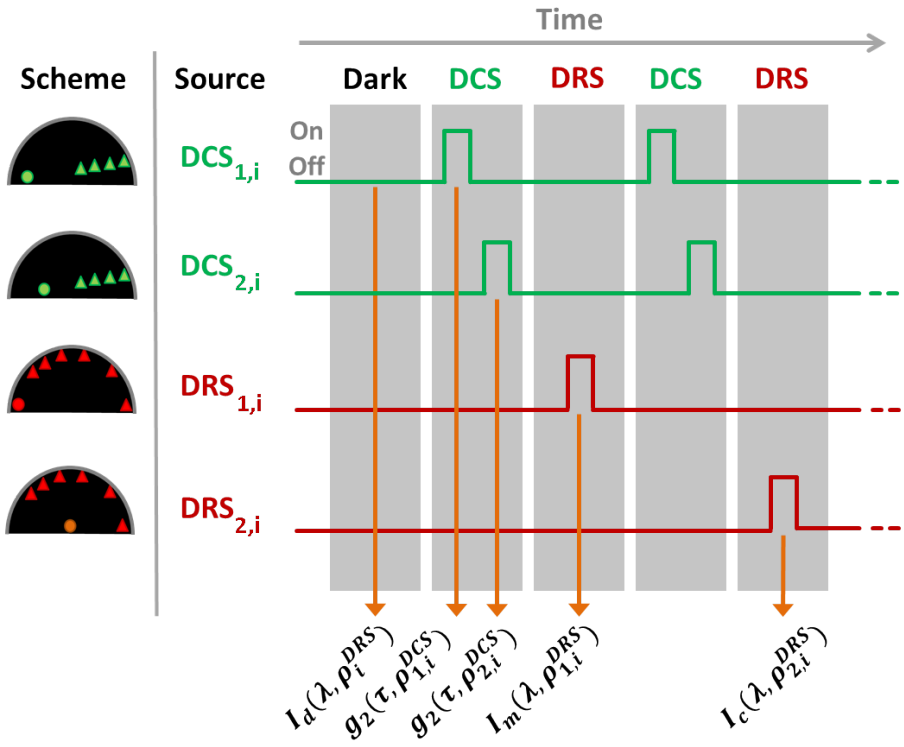

Figure 3.2: The hybrid DRS/DCS data acquisition timeline. As a first step, the dark intensity $I_d(\lambda, \rho^{DRS})$ is acquired with the camera shutter closed, then the DCS signals from the first ($g_2(\tau, \rho_{1,i}^{DCS})$) and second ($g_2(\tau, \rho_{2,i}^{DCS})$) source are acquired over the i^{th} detection fiber. Afterwards, the DRS data from the main source location is collected ($I_m(\lambda, \rho_{1,i}^{DRS})$) over at the detections fibers (i). A second set of DCS signals from both sources are obtained and later, the DRS data from the calibration source is gathered ($I_c(\lambda, \rho_{2,i}^{DRS})$) through the same detection fibers (i). This procedure is repeated for acquiring one dark image, eleven DCS files and ten DRS images (five from each source location).

3.2.1 *DRS data collection*

For the DRS data acquisition a set of three images are stored (Figure 3.3):

1. The dark intensity ($I_d(\lambda, \rho_i^{DRS})$): Records the counts read by the CCD sensor when isolated from any incoming light by keeping the camera shutter closed (Figure 3.3a).

2. The main source intensity ($I_m(\lambda, \rho_{1,i}^{DRS}$): Image of the reflected light when the main source position is employed for injecting light into the tissue. Since the detection fibers (i) are located at different distances from the main source position, the exponential decay of light over distance is resolved (Figure 3.3b).

3. The calibration source intensity ($I_c(\lambda, \rho_{2,i}^{DRS}$): Image of the reflected light when the calibration source position is employed for injecting light into the tissue. Since the fibers (i) are located equidistant from the calibration source position, the differences in light collection efficiency among fibers are recovered (Figure 3.3c).

In the DRS data acquisition, a set of five images per source (main and calibration) and one single dark image is recorded. The repeated images allow us to further average over repetitions for improving the Signal-to-Noise Ratio (SNR). The acquired set of images are later be processed for recovering the tissue optical properties (μ_a and $\mu_s^{'}$), and hence the tissue hemodynamic information.

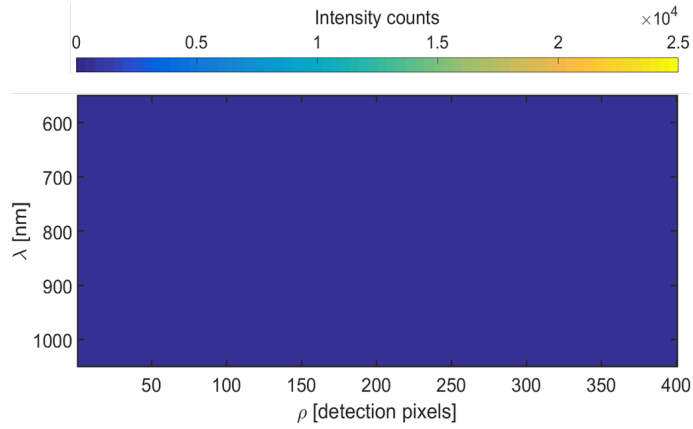

(a) $I_d(\lambda, \rho_i^{DRS})$

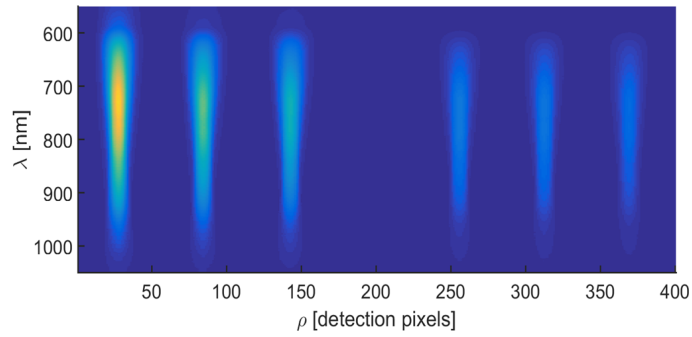

(b) $I_m(\lambda, \rho_{1,i}^{DRS})$

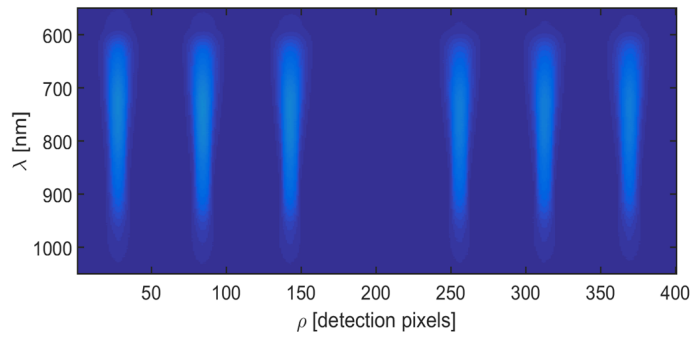

(c) $I_c(\lambda, \rho_{2,i}^{DRS})$

Figure 3.3: The set of images collected by the DRS device. A set of six fibers at different source-detector distances are employed to collected the back reflected light intensity and imaged by a CCD camera. a) The light intensity when the the camera shutter is closed; b) The light intensity when the main source is occupied and c) The light intensity when the calibration source is occupied

3.2.2 *DCS data collection*

For the DCS data acquisition, a text file containing eight tabulated intensity autocorrelation curves (four from each source) as well as the shared time delay vector (τ) is stored. Given the fact that the DCS signals are self-normalized with respect to their light intensity, the dependence of the correlation curve to the detection distance (ρ^{DCS}) is recovered by using a multi-distance detection scheme as modeled previously in Figure 2.9a in Section 2.5.2. An illustration of a representative set of real DCS collected normalized intensity autocorrelation curves (g_2) is shown in Figure 3.4.

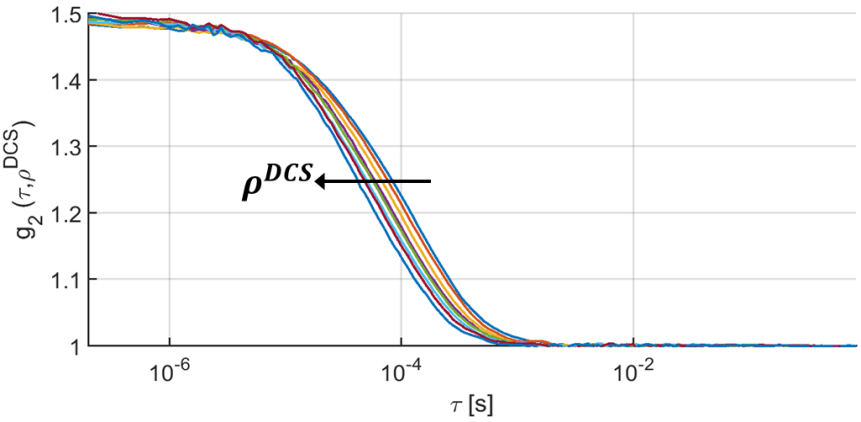

Figure 3.4: The set of normalized intensity autocorrelation functions (g_2) collected by the DCS device. The dependance of the decorrelation time of the signal with respect to the source-detector separation is illustrated, the longest the source-detector separation the fastest the intensity autocorrelation function decay.

In the DCS data acquisition a total of eleven files, containing eight normalized intensity autocorrelation curves each, were recorded. The repeated normalized intensity autocorrelation curves provide the feasibility to average over repetitions for improving the signal-to-noise ratio (SNR).

4 CONTACT HYBRID DEVICE: DATA PROCESSING

The previously described contact hybrid broadband diffuse reflectance and correlation spectroscopies (DRS/DCS) device (Chapter 3) has been designed for acquiring information from pre-clinical mouse models [1]. In this work, I have further improved the algorithms that were previously utilized in data analysis [2, 112] to adapt it to the complexity of the hypotheses introduced in this work (see Chapter 5 and 6). Therefore, in particular, this more elaborate algorithm allowed me to overcome or identify some artifacts which are generated by three main factors: the instrumental noise, the physiological heterogeneities and the limitations of the physical models.

- The instrumental issues are associated with the multi-fiber scheme for delivering and collecting light. In the DRS device, the disparity for light emission and collection among fibers is represented by a set of *coupling coefficients* for each source-detector pair. Those discrepancies are hence embedded into the gathered signals and contribute in a different amount to each detected signal [113]. This problem has been partially minimized in our previous work [2, 112]. On the other hand, since the DCS technique provides normalized autocorrelation curves, it is insensitive to the inter-fiber differences.

- The physiological issues such as the tissue heterogeneity (e.g. chaotic microvasculature, cysts, hemorrhages or necrosis), morphology (e.g. curvature of the surface) and skin features (e.g. hair or creases) affects the recovered set of signals in a different manner. For the DRS technique, the resolved exponential intensity decay over distance gets altered due to the heterogeneities in

the absorption coefficients among the paths followed by photons before being collected. In addition, the fiber-tissue mismatch due to the tissue morphology and skin features gets embedded into the previously mentioned *coupling coefficients* as an offset value. On the other hand, the autocorrelation curves collected by the DCS device would be disrupted in shape and shifted in time due to the tissue heterogeneities.

- The physical modeling issue affects both DRS and DCS techniques during the data post-processing. In the DRS technique, two main artifacts are observed: a) The collection of optical data at the limit of the diffusion regime ($\rho^{DRS}_{shortest} \approx 1/\mu_s'$) and b) The inherent crosstalk between the optical parameters (μ_s' and μ_a) and within the tissue chromophores (e.g Hb, HbO_2 and H_2O). In the DCS technique, the crosstalk between the β and D_b parameters with the μ_s' recovered from DRS hinders the proper recovery of the tissue dynamic information (e.g. blood flow).

The cumulative effect of the aforementioned set of issues limits the accurate recovery of the tissue static and dynamic information through the optical properties. To overcome this limitation, an algorithm aiming to minimize the impact of each contributing issues in each diffuse optical technique was developed. In the next sections, detailed explanation of the algorithms is provided. Alternative methods were also suggested by us [2, 114] and others [106, 115, 116] to reconstruct accurate information from the probed medium.

4.1 DRS DATA PROCESSING

To accurately recover the tissue optical properties, the artifacts described above have to be accounted for to minimize their impact. To this end, each of those issues was independently addressed by means of a developed algorithm for processing the collected DRS data. As a result, an optimum set of data referring to the lesser influenced signals

by those artifacts was recovered. The optimum selected data was then employed for reconstructing the tissue optical properties.

The developed algorithm consists of four main steps:

1. Data calibration and normalization.
2. Selection of optimum signal ratios.
3. Derivative spectroscopy and dynamic selection of optimal wavelengths.
4. Objective functions for estimating the optical properties

4.1.1 *Data calibration and normalization*

Due to the multi-fiber scheme of the contact probe (Figure 4.1) explained in Section 3.1.1, a set of *coupling coefficients* represents the inter-fiber differences for light emission and collection. Those differences are inherently embedded into the measured signals. The presence of those coefficients, modify the exponential light intensity decay recovered over multiple distances. Therefore their calibration is of utmost importance to match the theoretical light intensity decay.

Under the assumption of a semi-infinite homogeneous medium, the DRS data with the set of associated *coupling coefficients* is represented as:

1. Dark intensity: $I_d(\lambda, \rho_i^{DRS})$
2. Main source intensity: $S_1(\lambda)D_i(\lambda)I_m(\lambda, \rho_{1,i}^{DRS})$
3. Calibration source intensity: $S_2(\lambda)D_i(\lambda)I_c(\lambda, \rho_{2,i}^{DRS})$

Here the *source coupling coefficients* $S_1(\lambda)$ and $S_2(\lambda)$ refers to the light emission efficiency over wavelengths of the main and the calibration

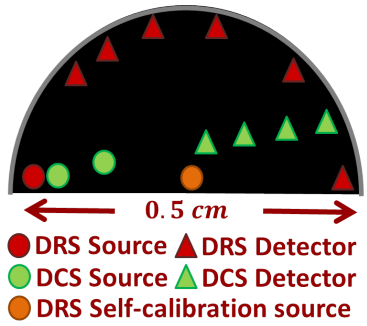

Figure 4.1: A schematic of the contact DRS/DCS probe. The DRS/DCS data is collected at several source-detector separations when light is shine through the corresponding source location. For the DRS technique, when the main source is used - red dot -, light is collected at distances ranging from 0.2 to 0.5 cm from the source, whereas when the self-calibration source - yellow dot -, data is collected equidistant (0.5 cm) from the source. On the other hand, DRS data is collected at several distances - green triangles - from the sources locations - green circles - that alternates to gather optical information at source-detector distances ranging from 0.2 to 0.5 cm.

source fibers respectively. The term $D_i(\lambda)$ refers to the *detector coupling coefficients* which represents the light collection efficiency of the i^{th} detection fiber.

The dark intensity is subtracted from both the main and the calibration source intensities, as a first step, to account for any background light as:

$$S_1(\lambda)D_i(\lambda)I_m^{'}(\lambda,\rho_{1,i}^{DRS}) = S_1(\lambda)D_i(\lambda)I_m(\lambda,\rho_{1,i}^{DRS}) - I_d(\lambda,\rho_i^{DRS})$$
$$S_2(\lambda)D_i(\lambda)I_c^{'}(\lambda,\rho_{2,i}^{DRS}) = S_2(\lambda)D_i(\lambda)I_c(\lambda,\rho_{2,i}^{DRS}) - I_d(\lambda,\rho_i^{DRS})$$

Afterwards, the division of the dark subtracted main source light intensity ($S_1(\lambda)D_i(\lambda)I_m^{'}(\lambda,\rho_{1,i}^{DRS})$) by the corresponding dark subtracted calibration source light intensity ($S_2(\lambda)D_i(\lambda)I_c^{'}(\lambda,\rho_{2,i}^{DRS})$) leads to the cancelation of the *detector coupling coefficient* represented by $D_i(\lambda)$.

The self-calibrated light intensity, $I_{sc}(\lambda,\widetilde{\rho}_i^{DRS})$ where the term $\widetilde{\rho}_i^{DRS}$ refers to the source-detector separation of the ith self-calibrated detector, is depicted as:

$$
\begin{aligned}
I_{sc}(\lambda, \widetilde{\rho}_i^{DRS}) &= \frac{S_1(\lambda) D_i(\lambda) I_m^{'}(\lambda, \rho_{1,i}^{DRS})}{S_2(\lambda) D_i(\lambda) I_c^{'}(\lambda, \rho_{2,i}^{DRS})} \\
&= \frac{S_1(\lambda) \cancel{D_i(\lambda)} I_m^{'}(\lambda, \rho_{1,i}^{DRS})}{S_2(\lambda) \cancel{D_i(\lambda)} I_c^{'}(\lambda, \rho_{2,i}^{DRS})} \\
&= \frac{S_1(\lambda) I_m^{'}(\lambda, \rho_{1,i}^{DRS})}{S_2(\lambda) I_c^{'}(\lambda, \rho_{2,i}^{DRS})}
\end{aligned}
$$

The removal of the *detector coupling coefficient* leads to a signal with a corrected light intensity exponential decay over distances. The resulting signal is then expected to be proportional to the Green's function solution to the photon diffusion equation denoted by Equation 2.9. Nevertheless, an offset factor $\Gamma(\lambda) = {}^{S_1(\lambda)}/_{S_2(\lambda)}$ composed by the *source coupling coefficients* still remains embedded into the signal, preventing their matching as shown below:

$$
I_{sc}(\lambda, \widetilde{\rho}_i^{DRS}) = \Gamma(\lambda) \frac{I_m^{'}(\lambda, \rho_{1,i}^{DRS})}{I_c^{'}(\lambda, \rho_{2,i}^{DRS})} \neq \frac{G(\lambda, \rho_{1,i}^{DRS})}{G(\lambda, \rho_{2,i}^{DRS})} \tag{4.1}
$$

To remove the $\Gamma(\lambda)$ term, a ratio between two self-calibrated signals, which I will refer to as *signal ratio*, must be considered in both sides of the Equation 4.1. Lets consider the self-calibrated signals from the i^{th} source-detector separation $\widetilde{\rho}_i^{DRS}$ for the numerator and the j^{th} source-detector separation $\widetilde{\rho}_j^{DRS}$ for the denominator. The two signals composing the ratio are expressed as:

$$
\begin{aligned}
I_{sc}(\lambda, \widetilde{\rho}_i^{DRS}) &= \Gamma(\lambda) \frac{I_m^{'}(\lambda, \rho_{1,i}^{DRS})}{I_c^{'}(\lambda, \rho_{2,i}^{DRS})} = \frac{G(\lambda, \rho_{1,i}^{DRS})}{G(\lambda, \rho_{2,i}^{DRS})} \\
I_{sc}(\lambda, \widetilde{\rho}_j^{DRS}) &= \Gamma(\lambda) \frac{I_m^{'}(\lambda, \rho_{1,j}^{DRS})}{I_c^{'}(\lambda, \rho_{2,j}^{DRS})} = \frac{G(\lambda, \rho_{1,j}^{DRS})}{G(\lambda, \rho_{2,j}^{DRS})}
\end{aligned}
$$

The light intensity ratio $I^{ratio}(\lambda, \widetilde{\rho}_i^{DRS}, \widetilde{\rho}_j^{DRS})$ of the i^{th} to the j^{th} self-calibrated signal is then expressed as:

$$I^{ratio}(\lambda, \widetilde{\rho}_i^{DRS}, \widetilde{\rho}_j^{DRS}) = \frac{\Gamma(\lambda)\dfrac{I_m^{'}(\lambda, \rho_{1,i}^{DRS})}{I_c^{'}(\lambda, \rho_{2,i}^{DRS})}}{\Gamma(\lambda)\dfrac{I_m^{'}(\lambda, \rho_{1,j}^{DRS})}{I_c^{'}(\lambda, \rho_{2,j}^{DRS})}} = \frac{G(\lambda, \rho_{2,j}^{DRS})G(\lambda, \rho_{1,i}^{DRS})}{G(\lambda, \rho_{2,i}^{DRS})G(\lambda, \rho_{1,j}^{DRS})}$$

Given the fact that the optical data at the i^{th} or j^{th} detection fibers from the self-calibration source is collected equidistant from the source location (Figure 4.1), the terms $G(\lambda, \rho_{2,i}^{DRS})$ and $G(\lambda, \rho_{2,j}^{DRS})$ in the above equation are equal and hence can be canceled, turning into:

$$I^{ratio}(\lambda, \widetilde{\rho}_i^{DRS}, \widetilde{\rho}_j^{DRS}) = \frac{\Gamma(\lambda)\dfrac{I_m^{'}(\lambda, \rho_{1,i}^{DRS})}{I_c^{'}(\lambda, \rho_{2,i}^{DRS})}}{\Gamma(\lambda)\dfrac{I_m^{'}(\lambda, \rho_{1,j}^{DRS})}{I_c^{'}(\lambda, \rho_{2,j}^{DRS})}} = \frac{G(\lambda, \rho_{1,i}^{DRS})}{G(\lambda, \rho_{1,j}^{DRS})}$$

$$I^{ratio}(\lambda, \widetilde{\rho}_i^{DRS}, \widetilde{\rho}_j^{DRS}) = \frac{\cancel{\Gamma(\lambda)}\dfrac{I_m^{'}(\lambda, \rho_{1,i}^{DRS})}{I_c^{'}(\lambda, \rho_{2,i}^{DRS})}}{\cancel{\Gamma(\lambda)}\dfrac{I_m^{'}(\lambda, \rho_{1,j}^{DRS})}{I_c^{'}(\lambda, \rho_{2,j}^{DRS})}} = \frac{G(\lambda, \rho_{1,i}^{DRS})}{G(\lambda, \rho_{1,j}^{DRS})}$$

$$I^{ratio}(\lambda, \widetilde{\rho}_i^{DRS}, \widetilde{\rho}_j^{DRS}) = \frac{I_m^{'}(\lambda, \rho_{1,i}^{DRS})I_c^{'}(\lambda, \rho_{2,j}^{DRS})}{I_m^{'}(\lambda, \rho_{1,j}^{DRS})I_c^{'}(\lambda, \rho_{2,i}^{DRS})} = \frac{G(\lambda, \rho_{1,i}^{DRS})}{G(\lambda, \rho_{1,j}^{DRS})}$$

Since the contact probe is designed with $N = 6$ source-detector pairs for collecting DRS optical data (Figure 4.1), the maximum number of calibrated ratios (with no presence of the $\Gamma(\lambda)$ term) that can be built is 36 (Figure 4.2a), denoted by Equation 4.2 and graphically expressed in Figures 4.2a and 4.2b.

$$I^{allratios}(\lambda, \tilde{\rho}_i^{DRS}, \tilde{\rho}_j^{DRS})\Big|_{j=1,i=1}^{j=N,i=N} = \frac{G(\lambda, \rho_{1,i}^{DRS})}{G(\lambda, \rho_{1,j}^{DRS})}\Big|_{j=1,i=1}^{j=N,i=N} \tag{4.2}$$

However, only 30 of them are suitable to be used since the signal ratios where $i = j$ (represented as the red diagonal and dots in Figures 4.2a and 4.2b, respectively) does not provide any information about the medium.

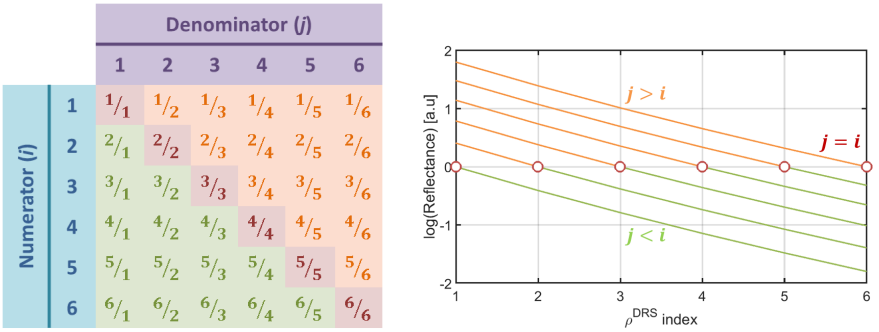

(a) Signal ratios in a matrix form.

(b) Signal ratios in a spatial form.

Figure 4.2: The complete set of signal ratios at a given wavelength: The green lower triangle in (a) and lines (b) corresponds to the signal ratios where the denominator has a high SNR and hence provides a set of signal ratios with better signal quality. On the other hand, the orange upper triangle in (a) and lines in (b) refers to the signal ratios where the denominator has low SNR due to long source-detector separations due to low light intensity levels. In red, the diagonal of the matrix in (a) and dots in (b) represents the set of signal ratios where no information is contained.

Furthermore, given the fact that the computed signal ratios are symmetric in shape [1], some of them are more suitable to be used while retaining the same amount of information as the complete set of signals. In this regard, when employing the signals coming from long detector distances, hence with lower SNR levels, as denominators (orange upper triangle and lines in Figures 4.2a and 4.2b respectively), their noise

1 The signals recovered from $I^{allratios}(\lambda,,\tilde{\rho}_i^{DRS},\tilde{\rho}_j^{DRS})$ are the inverted version of those calculated as $I^{allratios}(\lambda,\tilde{\rho}_j^{DRS},\tilde{\rho}_i^{DRS})$

gets propagated into the resulting signal ratio, therefore downgrading the signal quality. In contrast, this effect gets minimized when signals from short detector distances, thus with higher SNR levels, are used as a denominator (green lower triangle and lines in Figures 4.2a and 4.2b respectively) in the signal ratio, hence their lower noise level gets propagated into the resulting signal ratios.

In conclusion, the ensemble of 15 unique ratios, composed by the signals with higher SNR levels as denominators, contains the same amount of information as the complete set of signal ratios for describing the medium while minimizing the noise propagation.

The set of unique and calibrated signal ratios is given by:

$$I^{ratio}(\lambda, \tilde{\rho}_i^{DRS}, \tilde{\rho}_j^{DRS})\Big|_{j=1,i=j+1}^{j=N-1,i=N} = \frac{G(\lambda, \rho_{1,i}^{DRS})}{G(\lambda, \rho_{1,j}^{DRS})}\Big|_{j=1,i=j+1}^{j=N-1,i=N} \tag{4.3}$$

4.1.2 *Selection of optimum signal ratios*

The recovery of the optical properties of the probed media is highly dependent on the proper matching between the acquired optical signal and the Green's function solution to the DE. In real experimental data, this matching can be affected by several external factor and hence; the selection of the set of signal that better adjust to this condition, named as the optimum DRS signal ratios, is of utmost importance.

In the former section, a mathematical approach for removing the embedded *coupling coefficients* from the DRS signals was applied. To this end, an homogeneous media was assumed. Nonetheless, in reality biological tissues, either healthy [117] or cancerous[118–120], are heterogeneous. As a result, the gathered DRS optical data gets perturbed in both the spatial and spectral dimensions. On top of that, while performing the calibration procedure for removing the *coupling coefficients* (Section 4.1.1), the differences between signals due to the tissue heterogeneities are propagated to the resulting signal ratio. Therefore

a $\gamma_{i,j}^{ratio}(\lambda)$ term, where i and j refers to the numerator and denominator indices of the involved signals respectively, has to be associated to each of the previously defined calibrated signal ratios (Equation 4.3) to represent these issues:

$$\gamma_{i,j}^{ratio}(\lambda) I^{ratio}(\lambda, \tilde{\rho}_i^{DRS}, \tilde{\rho}_j^{DRS}) \Big|_{j=1,i=j+1}^{j=N-1,i=N} = \frac{G(\lambda, \rho_{1,i}^{DRS})}{G(\lambda, \rho_{1,j}^{DRS})} \Big|_{j=1,i=j+1}^{j=N-1,i=N} \tag{4.4}$$

The inclusion of the $\gamma_{i,j}^{ratio}(\lambda)$ term explain why the calibrated signal ratios do not match the normalized theoretical light propagation model (right side of the Equation 4.4). Thus, its contribution must be taken into account before recovering the tissue optical properties. However, in contrast with the previous calibration approach (Section 4.1.1), this term cannot be mathematically overcome since it is linked to a specific signal ratios. Hence, those ratios were the $\gamma_{i,j}^{ratio}(\lambda)$ contribution is minimum have to be targeted.

To select the optimum DRS signal ratios, a two-step method was applied:

1. The exponential decay-based selection
2. The spectral shape-based selection

A detailed description of each step is provided below.

4.1.2.1 *The exponential decay-based selection*

The propagation of any light wavelength in tissue exhibits an exponential intensity decay over distance with a well defined behavior (Equation 2.9). This feature can be exploited to detect the data points that diverge significantly from this trend due to the coupled $\gamma_{i,j}^{ratio}(\lambda)$ term. The intensity ratios where the $\gamma_{i,j}^{ratio}(\lambda)$ term impact is minimum,

and therefore closer to the theoretical light propagation model, would remain as the selected optimal data.

The identification of the optimum signal ratios is done by computing the logarithm of the multi-distance signal at a given wavelength to obtain a linear decay instead. The log-transformed data is then fitted with a linear regression model. This mechanism provides a way to assess how influential a data point from a given signal ratio is on the predicted linear model. In this manner, the impact of the $\gamma_{i,j}^{ratio}(\lambda)$ term in the spatial dimension of the calibrated signal at a given wavelength can be quantified.

The most common method to determine the influence of a point in a predicted linear model is the *Cook's distance* [121, 122], typically named only as *Cook's D*. This method aims to fit a linear regression model through the N spatially resolved observations and compare it against a refitted linear model that includes N-1 observations. A unitless score D is assigned to the i^{th} removed observation, indicating how influential that data point is for the linear regression model. This approach is repeated N times removing one observation at the time - known as bootstrapping - from the linear regression fit to assign a score to each observation.

The *Cook's D* score is defined as:

$$D(i) = \underbrace{\left[\frac{(y_N - \widehat{y}_{N(i)})^2}{p \times MSE}\right]}_{\text{"outlierness"}} \underbrace{\left[\frac{h_{N(i)}}{(1 - h_{N(i)})^2}\right]}_{\text{"extremeness"}} \tag{4.5}$$

Where y_N is the fitted response including all observations, $\widehat{y}_{N(i)}$ is the fitted response excluding the i^{th} observation, $p = 2$ is the number of coefficients in the regression model (the slope and the intercept) and the mean squared error (MSE) is defined as:

$$MSE = \frac{1}{N}\sum_{i=1}^{N}((y_N - \widehat{y}_{N(i)})^2)$$

The term $h_{N(i)}$ refers to the i^{th} Leverage value and represents the deviation of an observation from its mean value in the *x-axis* referred as the predictor variable (x)

$$h_{N(i)} = \frac{(x_N - \widehat{x}_{N(i)})^2}{\sum(x - \bar{x})} + \frac{1}{N}$$

Similar to the previously defined parameters, the x_N term refers to the x coordinates of the fitted response including all the observations, $\widehat{x}_{N(i)}$ refers to the x coordinates of the fitted response excluding the i^{th} observation, the term x is the real predictor variable in the *x-axis* and $\bar{x}$ is the mean value of the predictor variable.

The *Cook's D* score (Equation 4.5) represents the influence of a given observation in the linear regression model based on two aspects: The "*outlierness*" of the observation representing its residual value when adjusted by a linear model, and the "*extremeness*" of the same observation representing its Leverage value. These terms would be high if the i^{th} observation is unusual with respect to the rest of data points in the y or x axis, respectively.

In general, there is no standard rule to set an optimum threshold value to define an observation as influential based on its *Cook's D* score. The most common assumption is that an observation with $D \geq 1$ is quite likely to be influential whereas when $D > 0.5$ it might be influential and it is worthy to investigate further. However, the setting of a threshold value for defining an observation as influential is dependent on the nature of the problem.

The usage of the *Cook's D* approach relies on the amount of information provided to the method to fit a representative linear model of the data. In this regard, by utilizing only the unique set of signal ratios (Equation 4.4), few observations are fed into the model due to the exclusion of the symmetric ratios (orange upper triangle and lines in Figure 4.2). To surpass this limitation, the complete set of signal ratios can be fed into the method to be fit. This approach is valid

since, as mentioned earlier, there is no difference in the amount of information provided by the unique or the complete set of ratios since they are the inverted version of the other. By doing this, a total of six log-transformed data sets, one for each of the j^{th} signals employed as a denominator, analogous to those shown in Figure 4.2b, can be fed into the model.

The complete set of ratios with the coupled $\gamma_{i,j}^{ratios}(\lambda)$ term is given by:

$$\gamma_{i,j}^{ratio}(\lambda) I^{ratio}(\lambda, \widetilde{\rho}_{i,j}^{DRS}, \widetilde{\rho}_{i,j}^{DRS})\Big|_{j=1,i=1}^{j=N,i=N} = \frac{G(\lambda, \rho_{1,i}^{DRS})}{G(\lambda, \rho_{1,j}^{DRS})}\Big|_{j=1,i=j}^{j=N,i=N} \tag{4.6}$$

The computed *Cook's D* scores for each of the six data sets over every measured wavelength (λ) are expressed as $D(i, j, \lambda)$; where i and j refers to the signal employed as numerator and denominator respectively, and λ stands for the assessed wavelength.

The signal ratios that minimize the impact of the $\gamma_{i,j}^{ratio}(\lambda)$ term in the spatial dimension, named as potential signal ratios, provides a set of data that better resemble the theoretical light decay. Nevertheless, the selected signals must preserve enough information in order to obtain an accurate estimation of the tissue optical properties.

To this end, a two-level criteria aiming to assists in the selection of the potential signal ratios at each wavelength was applied:

1. Three levels of Cook's D scores.
2. Minimum percentage of selection over wavelengths

1. Three levels of Cook's D scores:

The estimated scores $D(i, j, \lambda)$ were categorized into three different threshold levels (k) according to $D \leq 0.25$, $D \leq 0.75$ and $D \leq 1.5$, each of them associated to a low, medium and high level of influence respectively. By performing this classification, the number of observations of each signal ratio (i, j) over all wavelengths (λ) belonging to a certain

influence level (k) was obtained. The results are stored in a boolean matrix $D_{th}(i,j,\lambda,k)$ that contains ones in the (i,j,λ,k) location if the $D(i,j,\lambda)$ score fulfill the k threshold level criteria and zeros otherwise.

2. Minimum percentage of selection over wavelengths:

From the thresholded boolean matrix $D_{th}(i,j,\lambda,k)$, the number of selections at a given level (k) of each observation in a signal ratio (i,j) can be counted, from which the percentage of times that it was selected with respect to the total number of wavelengths (λ) can be inferred. Moreover, the information from the D_{th} matrix can be restrained to that related to the unique set of ratios.

Since we are interested in preserving the maximum amount of information, those signal ratios with a selection percentage $\geq 95\%$ over wavelengths at each k level are retained as potentially viable. The set of signal ratios, indicated by m_k where $m_k \in i,j$, that minimize the impact of the $\gamma_{i,j}^{ratio}(\lambda)$ term in the spatial dimension at each threshold level k are referred as *spatial ratios* and expressed by:

$$I_{m_k}^{\substack{spatial \\ ratios}}(\lambda, \widetilde{\rho}_i^{DRS}, \widetilde{\rho}_j^{DRS}, k) = \gamma_{m_k}^{ratio}(\lambda) I_{m_k}^{ratio}(\lambda, \widetilde{\rho}_i^{DRS}, \widetilde{\rho}_j^{DRS}) \tag{4.7}$$

This set of data will be further employed in Section 4.1.2.2 for the determination of the optimum DRS signal ratios.

4.1.2.2 *The spectral shape-based selection*

The heterogeneous distribution of chromophore concentrations along tissue (e.g. tumor) alters the spectral shape of the collected signal. Those discrepancies are represented by the spectral contribution of the $\gamma_{i,j}^{ratio}(\lambda)$ term in the calibrated signal (Equation 4.4). However, tissue heterogeneity is not the only disruptive factor in the spectral dimension; poor signal quality and featureless signals also contribute and mislead the quantification of the tissue optical properties. The former one is cause by the lack of detected photons at long source-detector

separations; deriving into noisy signals with low signal-to-noise ratios (SNR). The second one is cause by the major contribution of scattering interactions at short source-detector separations ($\rho^{DRS} < 1/\mu_s'$), denoted few absorption events and hence shapeless collected signals.

To overcome those spectral issues simultaneously, a hierarchical agglomerative clustering (HAC) [123–126] algorithm is employed. The objective of this method is to identify the DRS signal ratios with higher spectral inter-correlation and thus, minimize the spectral contribution of the $\gamma_{i,j}^{ratio}(\lambda)$ term. Nonetheless, we remind the reader that the final goal of the entire approach is to minimize both the spatial and spectral impact of the $\gamma_{i,j}^{ratio}(\lambda)$ term. Therefore, by feeding the previously selected set *spatial ratios* (Equation 4.7), were the spatial impact of the $\gamma_{i,j}^{ratio}(\lambda)$ term is minimum in the elements denoted by m_k, into the HAC algorithm a full minimization of the contribution of the $\gamma_{i,j}^{ratio}(\lambda)$ term in both the spatial and spectral dimensions of the DRS data set is achieved at three different k levels of influence.

The algorithm aims to create clusters from the set of potential signal ratios, named as objects, based on their spectral similarities. In this manner, the featureless and noisy signal ratios will show less similarity to the rest of the signals and would be grouped in a cluster. On the other hand, the objects with higher similarity and hence less influenced in the spectral dimension by the $\gamma_{i,j}^{ratio}(\lambda)$ term, would be grouped in another cluster.

The algorithm for clustering the objects can be divided into four steps:

1. Calculate the distance between objects.
2. Group objects into clusters.
3. Determine the optimal number of clusters.
4. Selection of the best cluster.

1. Calculate the distance between objects:
The HAC algorithms relies on a distance metric to determine the similarity between pairs of objects. When the objects are represented as sets of Cartesian points (x,y), some of the distance metrics routinely used are the Minkowski, City Block or Chebychev, and the most commonly employed is the Euclidean distance. Since in our approach the *spatial ratios* ($I^{spatial}_{m_k^{ratios}}(\lambda, \widetilde{\rho}_i^{DRS}, \widetilde{\rho}_j^{DRS}, k)$) are represented as vectors over λ at each threshold level k (Section 4.1.2.1), a different approach must be considered for defining the distance metrics between objects. The linear Pearson correlation coefficient (p_{st}) [127], is a suitable mechanism for determining the grade of similarity between two vector objects. Since the HAC algorithm requires a distance metric, the *Pearson distance correlation* (d_{st}) can be defined as:

$$\begin{aligned} d_{st} &= 1 - p_{st} \\ \text{with } p_{st} &= \frac{(x_s - \bar{x_s})(x_t - \bar{x_t})'}{(\sqrt{(x_s - \bar{x_s})(x_s - \bar{x_s})'})(\sqrt{(x_t - \bar{x_t})(x_t - \bar{x_t})'})} \end{aligned} \tag{4.8}$$

Where x represents the set of signals ($I^{spatial}_{m_k^{ratios}}(\lambda, \widetilde{\rho}_i^{DRS}, \widetilde{\rho}_j^{DRS}, k)$) at a given influence level k, whereas s and t represent two different elements of the x data. The terms $\bar{x_s}$ or $\bar{x_t}$ express the mean over wavelengths of the s and t objects respectively. In Equation 4.8, the lower d_{st} values represent the stronger linear correlations between objects.

2. Group objects into clusters:
The *Pearson distance correlation* metric is employed to link pairs of objects that are close together into binary clusters (clusters made up of two objects). An *average linkage method* [128] is further employed to create higher order clusters ($\geq$ 2 objects) while avoiding bias due to short or long distance metrics. This method employs the average distance between and within all objects contained in each cluster involved in the calculation. The distance d between clusters r and s is given by:

$$d(r,s) = \frac{1}{n_r n_s} \sum_{a=1}^{n_r} \sum_{b=1}^{n_s} dist(x_{r,a}, x_{s,b})$$

Where n_r and n_s are the number of objects in each cluster. The term *dist* corresponds to the updated distance from cluster r to s. The terms $x_{r,a}$ and $x_{s,b}$ refers to the a^{th} and b^{th} object in clusters r and s respectively.

The grouping of the objects can be graphically represented by a *dendrogram*, also known as a *cluster tree* or *hierarchical tree*. The *dendrogram* (Figure 4.3) represents the relationship between all objects using branches that connect them in a multilevel scheme. The horizontal lines represent the linkage between objects whereas the height of the branch represents the distance between objects.

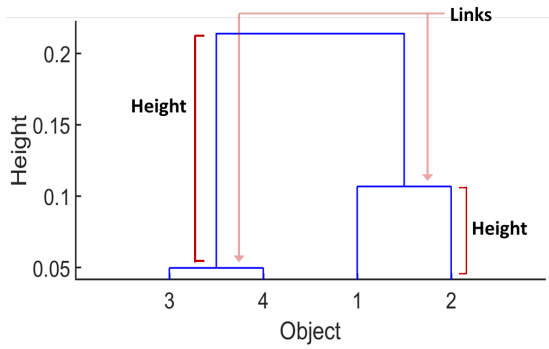

Figure 4.3: Illustration of a dendrogram. The objects are grouped into clusters based on the inter-objects distance, represented as heights. The objects corresponding to the same cluster are related through the links connecting them.

3. Determine the optimal number of clusters:

The number of clusters is defined by the height where the dendrogram tree is "cut". The choice of a proper cutting value is often ambiguous and heavily dependent on the type of data being analyzed. In this work, the Mojena stopping rule [129] is employed to determine the

most appropriate height value (*ch*) to "cut"' the dendrogram tree to obtain an optimum number of clusters. This rule was selected due to its simplicity to be implemented and its reliability to perform well in an unsupervised manner [130].

The Mojena stopping rule is defined as:

$$ch = \bar{h} + \psi s_h \tag{4.9}$$

Where $\bar{h}$ and s_h refer to the mean and standard deviation of the dendrogram heights, respectively. The term ψ is an arbitrary constant to balance the sensitivity and specificity of the selection. For our purposes, $\psi = 0.5$ was empirically selected after testing its performance in several training data sets.

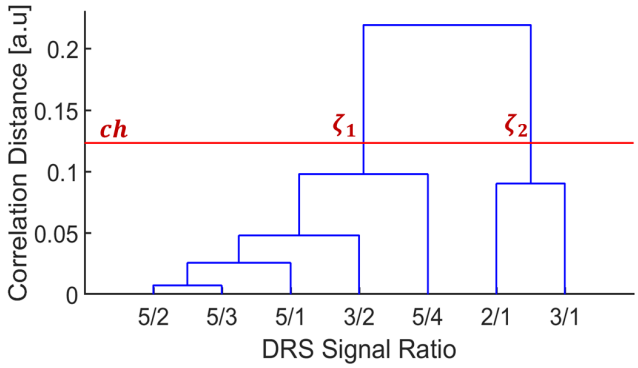

Figure 4.4: The selection of the optimum number of clusters. The potential set of signal ratios (Section 4.1.2.1) were clustered by means of HAC analysis. The optimum number of clusters (ζ) were determined through the Mojeda stopping criteria (*ch*). The first cluster (ζ_1) contain the signal ratios with the higher inter-correlation. The DRS signal ratios assigned to the second cluster ($^2/_1, ^3/_1 \in \zeta_2$) corresponds to featureless signals.

By cutting the dendrogram at the estimated *ch* value, a total of ζ optimum clusters (Figure 4.4) per threshold level k are formed. Each of the formed clusters contains a subset of the elements denoted by the m_k term.

4. Selection of the best cluster:
The proper selection of the optimum cluster, whose objects are less sensitive to the $\gamma_{i,j}^{ratio}(\lambda)$ term in the spectral dimension, is of utmost importance. To this end, the heights of all branches linking the objects in each ζ^{th} cluster of a given threshold level k are considered. We remind the reader that the height of the branch between two linked objects represents the distance between them; therefore, based on the *Pearson distance correlation* metric previously introduced, the optimum cluster will be that with the minimum average height and hence, the highest inter-object similarity.

The elements contained in the selected optimum cluster, denoted by ℓ_k, represent the optimum DRS signal ratios - the ultimate goal of this procedure - where the spatial and spectral impact of the $\gamma_{i,j}^{ratio}(\lambda)$ term is minimum at three difference influence levels k. These elements can be related to the set of *spatial ratios* (denoted by m_k) as $\ell_k \in m_k \in i, j$, where i, j stands for the set of unique signal ratios (Equation 4.4)

The optimum DRS signal ratios, named as *optimum ratios* for simplicity, are described as:

$$I_{\ell_k}^{optimum\ ratios}(\lambda, \widetilde{\rho}_i^{DRS}, \widetilde{\rho}_j^{DRS}, k) = \gamma_{\ell_k}^{ratio}(\lambda) I_{\ell_k}^{ratio}(\lambda, \widetilde{\rho}_i^{DRS}, \widetilde{\rho}_j^{DRS}) \tag{4.10}$$

Equation 4.10 allow us to obtain a different set of optimum DRS signal ratios ℓ_k, depending on the chosen level k (Section 4.1.2.1). This provides a manner to balance the data quality with respect to the number of signals (e.g. few signal ratios with high data quality or vice versa).

Therefore a global optimum set of DRS signal ratios must be determine to be employed for the rest of the data processing. In this regard, given the fact that in our setup the maximum amount of DRS signal ratios is 15 (Section 4.1.1), a minimum of 5 elements in Equation 4.10 are desired in order to balance for the data quality and the number of selected signals while preserving at least the 33% of DRS information. Therefore, since each of the k levels are associated with a low, medium

and high influence of the $\gamma_{i,j}^{ratio}$ term respectively (Section 4.1.2.1); the global optimum DRS signal ratios (I^{DRS}) can be determined by the k level with the lowest influence that contains at least 5 elements. These elements would be represented by the $\overset{*}{\ell}_k$ term.

In this manner, the global optimum DRS signal ratios can be defined as:

$$I^{DRS}(\lambda, \widetilde{\rho}_i^{DRS}, \widetilde{\rho}_j^{DRS}) = \underset{\ell_k}{I_{*}^{optimum\ ratios}}(\lambda, \widetilde{\rho}_i^{DRS}, \widetilde{\rho}_j^{DRS}, k) \tag{4.11}$$

Similarly, the indices of the selected global optimum DRS signal ratios, expressed by $\overset{*}{\ell}_k$, can be applied to the Green's function (G^{DRS}) solution to the photon diffusion equation (DE), being expressed as:

$$G^{DRS}(\lambda, \widetilde{\rho}_i^{DRS}, \widetilde{\rho}_j^{DRS}) = \underset{\ell_k}{G_{*}}(\lambda, \widetilde{\rho}_i^{DRS}, \widetilde{\rho}_j^{DRS}) \tag{4.12}$$

These set of equations contain the experimental and theoretical global optimum ratios and would be employed for recovering the tissue optical properties by fitting Equation 4.11 to Equation 4.12.

4.1.3 *Derivative spectroscopy and dynamic selection of optimum wavelengths*

Even though the optimum set of DRS signal ratios, with minimal influence (spatial and spectral) of the $\gamma_{ratio}^{ij}(\lambda)$ term, has been determined, the crosstalk issue - when the estimated value of a variable is affected by the value of another - hinders the proper retrieval of the tissue optical properties (Figure 4.5).

Historically, in the continuous-wave (CW) approach, it has been theoretically demonstrated [131] that it is impossible to uniquely separate scattering from absorption when employing a single wavelength light source. This limitation arise from the effective attenuation coefficient, $k(\lambda) = \sqrt{3\mu_s^{'}(\lambda)\mu_a(\lambda)}$, which determines the light intensity decay rate

over distance as a multiplicative factor of the optical properties (Equation 2.9). Therefore, there are multiple combinations of $\mu_s^{'}$ and μ_a coefficients that can provide a solution that minimizes the errors between the measured signal and the theoretical model.

To overcome this issue, Corlu *et. al* [132, 133] proposed the introduction of the known spectral information of the medium. With this approach, the assumption of the wavelength-dependence of the scattering (adhering to the Mie approximation) and absorption (given by the molar absorption coefficient of tissue chromophores) coefficients, in addition to the spatially resolved light intensity decay aids for better constraining the problem, hence minimizing the crosstalk between the optical properties contributions [134, 135].

However, the introduction of the spectral information of several tissue chromophores derives into the appearance of inter-chromophore crosstalk (Figure 4.5). This means that the contribution of a certain chromophore over the wavelengths can mislead the correct estimation of the others, leading to an incorrect estimation of the absorption coefficient (μ_a) and hence, an incorrect scattering coefficient ($\mu_s^{'}$) calculation.

In an effort to overcome the previous crosstalk issues, several methodologies have been studied. In this regard, the derivative spectroscopy method [106, 110, 113, 136] has demonstrated that, by computing the spectral derivative of the spatially resolved DRS signals, the scattering contribution is minimized while enhancing the absorption signal features, therefore minimizing the crosstalk between the optical properties. Moreover, by applying this approach, the spatial information of the data would be given by its shape and amplitude, therefore removing the influence of the calibration and coupling coefficient factors. Based on the above-mentioned features, this method can aid in minimizing the spatial impact of the $\gamma_{ratio}^{ij}(\lambda)$ term.

In addition to the derivative spectroscopy, the selection of wavelengths [132–135, 137] where the difference in absorption between chromophores is maximized, help for addressing the inter-chromophore

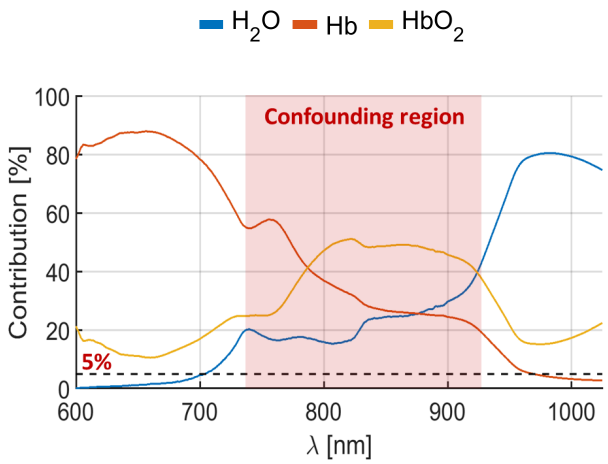

Figure 4.5: Illustration of the inter-chromophore crosstalk in a continuous-wave device: The contribution of a given chromophore over wavelengths can be strongly significant, therefore creating a *confounding region* ($\approx$ 730 - 930 nm) where the decoupling of the independent contribution of a chromophore is difficult to achieve. This effect causes a misleading estimation of the absorption coefficient (μ_a), thus deriving into an inaccurate reduced scattering coefficient (μ_s').

crosstalk. This strategy consists in a field of study by its own due to the multitude of approaches developed for achieving the best contrast between chromophores; although, in general, they all coincide in obtaining a static set of spectral bands that provide the best inter-chromophore separation. However, when monitoring longitudinal hemodynamic changes, and therefore the spectral shape of the gathered DRS signals vary over time, the employment of the same static spectral bands might not be a reliable methodology for recovering the tissue information. Furthermore, when assessing heterogeneous tissue, such as cancer tumors, the suggested spectral bands might not be useful for all regions.

In this work, a method that combines both strategies, the derivative spectroscopy and the determination of the optimum spectral bands is presented as a suitable alternative to minimize the crosstalk issue and

therefore retrieve accurate tissue optical properties. The most important characteristic of the here proposed strategy relies on the fact of finding dynamic sets of optimum wavelengths, depending on the assessed signal, that provides the best inter-chromophore contrast. This characteristic allows us to overcome the issues related to the heterogeneity of the tissue as well as the longitudinal changes in the spectral shape of the signal. Furthermore, the proposed method can be easily extended to consider other chromophores or contrast agents, providing the flexibility to be employed for multiple purposes.

The developed algorithm utilizes the previously selected set of optimum DRS signal ratios since they provide the highest amount of information while preserving the best signal quality.

As a first step, the first and second spectral derivatives of both the theoretical (Equation 4.12) and experimental (Equation 4.11) signal ratios at each signal ratio ($\overset{*}{\ell}_k$) were calculated by means of the spectral differences as follows:

$$\frac{\delta}{\delta\lambda} f(\lambda, \widetilde{\rho}_i^{DRS}, \widetilde{\rho}_j^{DRS}) = \frac{f(\lambda(s), \widetilde{\rho}_i^{DRS}, \widetilde{\rho}_j^{DRS}) - f(\lambda(s+1), \widetilde{\rho}_i^{DRS}, \widetilde{\rho}_j^{DRS})}{\lambda(s) - \lambda(s+1)} \Bigg|_{s=1}^{N_\lambda - 1}$$

$$\frac{\delta^2}{\delta\lambda^2} f(\lambda, \widetilde{\rho}_i^{DRS}, \widetilde{\rho}_j^{DRS}) = \frac{\frac{\delta}{\delta\lambda} f(\lambda(s), \widetilde{\rho}_i^{DRS}, \widetilde{\rho}_j^{DRS}) - \frac{\delta}{\delta\lambda} f(\lambda(s+1), \widetilde{\rho}_i^{DRS}, \widetilde{\rho}_j^{DRS})}{\lambda(s) - \lambda(s+1)} \Bigg|_{s=1}^{N_\lambda - 1} \tag{4.13}$$

where f refers to either the theoretical (G^{DRS}) or experimental (I^{DRS}) signals, s refers to the assessed wavelength and N_λ to the total number of wavelengths fitted (401 for the range here employed: 600 nm to 1000 nm).

The high frequency noise was removed from the spectral derivatives by means of a Savitzky-Golay filter [138] with a polynomial order $p_{sg} = 2$ and a window size $w_{sg} = 5$. The filtered signals were then fed into a non-linear least square minimization method (LSQNONLIN

with Levenberg-Marqardt algorithm, MATLAB, The MathWorks Inc., USA) in order to fit the first and the second derivatives of the theoretical model ratios (plugging Equation 4.12 into Equation 4.13) to the corresponding measured DRS signal ratios simultaneously (plugging Equation 4.11 into Equation 4.13). During this minimization method, several potential concentrations c_i for each tissue chromophore $\epsilon_i(\lambda)$ are iteratively evaluated in order to obtain an optimum absorption coefficient (μ_a) as in Equation 2.1, repeated below to remind the reader.

$$\mu_a(\lambda) = log(10) \cdot \sum_{i=1}^{n} \epsilon_i(\lambda) c_i \tag{2.1}$$

Hence, by considering the estimated absorption coefficient (μ_a) at each iteration as the total absorption over wavelengths, the percentage of contribution from each chromophore, given by its molar extinction coefficient ($\epsilon_i(\lambda)$) times its estimated concentration (c_i), at each wavelength can be calculated from the area under the curve. By exploiting this characteristic, the spectral bands where the contribution of a given chromophore is dominant with respect to the rest can be dynamically determined over the minimization procedure. In this work, the cromophores with contribution percentages higher or equal than 5% percent in a given wavelength would be considered as significant in such wavelength.

By following this procedure, the spectral bands dominated by the contribution of a single chromophore can be determined. Nevertheless, it has been observed that for the typical experimental data, there are chromophores (e.g. HbO_2) that do not dominate at any specific wavelength range; however, it is observed that they contribute together with other chromophores (e.g. Hb or H_2O) that are dominant in other spectral bands. Therefore, the optimal spectral bands (λ_{opt}) are given by those regions (Figure 4.6) where the contribution of ≤ 2 chromophores is dominant (>5%). Furthermore, the usage of the first and the second spectral derivatives simultaneously provides the capability to determine different spectral bands for a given chromophore

where its contribution is dominant in each of the spectral derivatives. These bands are denoted as $\lambda_{opt}^{\cdot}$ and $\lambda_{opt}^{\cdot\cdot}$, respectively.

4.1.4 *Objective functions for estimating the optical properties*

During the dynamic selection of the optimum spectral bands in the first and the second derivatives, a two-step fitting procedure is performed to estimate the tissue optical properties.

The first step consists on fitting the first and second derivatives in the dynamically selected optimum wavelengths for retrieving all the unknown parameters (A_0, b, c_{H_2O}, c_{Hb} and c_{HbO_2}) and therefore the tissue optical properties. However, as introduced before (Section 4.1.3) when employing the derivative spectroscopy method, the contribution of the reduced scattering coefficient ($\mu_s^{'}$) is minimum. Therefore, this steps aims to provide an accurate estimate of the absorption coefficient (μ_a) from the spectral derivative analysis.

To this end, the employed objective function is described by:

$$\chi^2 \quad = \begin{bmatrix} f_1 & f_2 \end{bmatrix}^2$$

where

$$f_1 = \sum_{s_1=1}^{\lambda_{opt}^{\cdot}} \left(\frac{\delta G^{DRS}(\lambda_{opt}^{\cdot}, \widetilde{\rho}_i^{DRS}, \widetilde{\rho}_j^{DRS})}{\delta \lambda_{opt}^{\cdot}} - \frac{\delta I^{DRS}(\lambda_{opt}^{\cdot}, \widetilde{\rho}_i^{DRS}, \widetilde{\rho}_j^{DRS})}{\delta \lambda_{opt}^{\cdot}} \right)$$

$$f_2 = \sum_{s_2=1}^{\lambda_{opt}^{\cdot\cdot}} \left(\frac{\delta^2 G^{DRS}(\lambda_{opt}^{\cdot\cdot}, \widetilde{\rho}_i^{DRS}, \widetilde{\rho}_j^{DRS})}{\delta^2 \lambda_{opt}^{\cdot\cdot}} - \frac{\delta^2 I^{DRS}(\lambda_{opt}^{\cdot\cdot}, \widetilde{\rho}_i^{DRS}, \widetilde{\rho}_j^{DRS})}{\delta^2 \lambda_{opt}^{\cdot\cdot}} \right)$$

In the second step, the reduced scattering coefficient is aimed to be recovered through the fitting of the zero derivatives over the whole wavelength range (λ) of the theoretical and experimental data. To this end, the previously obtained tissue chromophore concentrations (c_{H_2O},

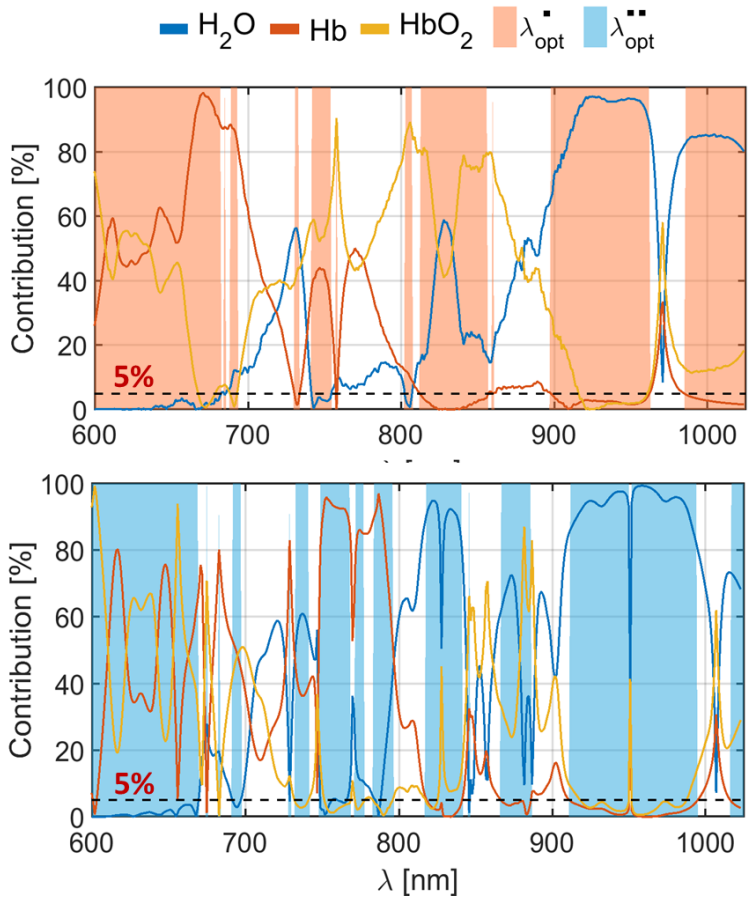

Figure 4.6: The dynamically selected optimum wavelengths. The first derivative (top) denotes a region of long wavelengths (≈ 900 - 1000 nm) dominated by the H_2O contribution, whereas in the short wavelength range (≈ 600 - 700 nm) the Hb and HbO_2 contribute similarly. However, from the middle wavelength region (≈ 800 - 850 nm) the HbO_2 contribution can be decoupled by knowing the H_2O contribution from its dominated region. Therefore, the Hb value can be decoupled from the short wavelength region. On the bottom, the chromophores contribution in the second derivative shows similar trends to the first derivative. Nevertheless, in this approach, the Hb is observed to be dominant in the middle region (≈ 700 - 800 nm), and hence, the HbO_2 can be disentangled from the short wavelength region (≈ 600 - 700 nm).

c_{Hb} and c_{HbO_2}), hence the absorption coefficient (μ_a), would be fixed. The A_0 and b parameters that conform the theoretical modeling of the reduced scattering coefficient ($\mu_s^{'}$) are then minimized through the following objective function.

$$\chi^2 = \sum_{j=1}^{\lambda} \left[G^{DRS}(\lambda, \widetilde{\rho}_i^{DRS}, \widetilde{\rho}_j^{DRS}) - I^{DRS}(\lambda, \widetilde{\rho}_i^{DRS}, \widetilde{\rho}_j^{DRS}) \right]^2 \tag{4.14}$$

After following the two-step minimization function introduced above, the optimum tissue optical properties (μ_a and $\mu_s^{'}$) minimizing the impact of the $\gamma_{i,j}^{ratio}(\lambda)$ term and the crosstalk issues can be recovered and hence; the static tissue hemodynamics (e.g. THC and SO_2) can be inferred.

4.2 DCS DATA PROCESSING

The DCS technique aims to recover the dynamic information (e.g. BFI) of a given media from the recorded light intensity fluctuations over time of a single speckle at several detection distances. Therefore, single-mode fibers, detecting two orthogonal polarization modes ($M = 2$) [46], are employed for light collection while matching the imaged speckle to the detector size. The gathered light intensity fluctuations are employed to compute the multi-distance self-normalized intensity autocorrelation functions (g_2^m where m refers to the measured signal) from which the dynamic information can be extracted. To this end, the β parameter is utilized to calculate the measured normalized electric field autocorrelation functions (g_1^m) by means of the Siegert relation (Equation 2.14). The measured electric field autocorrelation functions are then proportional to the theoretical multi-distance normalized electric field autocorrelation functions (g_1^t where t refers to the theoretical model) obtained when feeding the DRS obtained optical properties ($\mu_s^{'}$ and μ_a) along with the estimated αD_b value in Equation 2.15. In this method, a β value is calculated from the early corre-

lation times ($\lim_{\tau \to 0}$) of each of the collected g_2^m signals whereas the estimated αD_b term contains the dynamic information of the probed media (e.g. flow).

In contrast with the DRS technique, where the calibration process is crucial to cancel the differences in light emission and collection among fibers, the DCS technique does not require a calibration procedure due to the acquisition of self-normalized data. However, several artifacts similar to those of the DRS technique (Section 4.1), must be taken into account prior the recovery of the dynamic information. Those artifacts arise from the probe-tissue mismatch, the tissue heterogeneity and the crosstalk between the β and αD_b parameters.

The probe-tissue mismatch, analogous to that present in the DRS signals and arising from the tissue morphology (e.g. curvature) and skin features (e.g. hair or creases), leads to the collection of data from more than a single speckle and hence, higher order of modes ($M > 2$). Given the fact that the β parameter is inversely proportional to the number of detected modes ($\beta = 1/M$), the estimated normalized electric field autocorrelation (g_1^m) might be shifted upwards according to Equation 2.14.

Regarding the tissue heterogeneities, as introduced during the forward DCS modeling in Section 2.5.2, variations in the tissue optical properties would cause the measured normalized intensity autocorrelation function (g_2^m) to be either shifted in time due to variations in the reduced scattering coefficient (Figure 2.8b) or disrupted in shape and time due to changes in the tissue absorption coefficient (Figure 2.8a). In general, tissue heterogeneities impacts in both tissue optical properties, hence modifying the collected DCS signals in shape and time. Those variations are translated to the estimated measured g_1^m autocorrelation function.

Finally, it has been proved that simultaneous fitting of both β and αD_b parameters of a single g_1^m autocorrelation curve provides more accurate estimations of these variables [139], hence reducing their crosstalk. Although this approach has been extensively applied to extract the

dynamic information from the collected DCS signals, it is only valid under the assumption that the g_1^m function is not disrupted in time or shape, meaning that the probed media is homogeneous, a condition rarely found in tissue. Moreover, when expanding this approach to a multi-distance scheme for acquiring data, as the one here reported (Section 3.1.2), the limitations of this method become more evident. For instance, by obtaining a specific β value that places the estimated g_1^m function at an initial value of 1 (as the theoretical model in Equation 2.15), if the signal is disrupted in time or shape due to the aforesaid heterogeneities, the theoretical autocorrelation function (g_1^t) for a given αD_b value might not match the location in time of the multi-distance signals, hence providing misleading results.

To overcome these artifacts, an algorithm aiming to detect the set of DCS measured normalized intensity autocorrelation functions (g_1^m) that better resemble the theoretical solution to the correlation diffusion equation (CDE), denoted by g_1^t, for an estimated β and D_b parameters was developed.

The algorithm consists of three steps:

1. Estimation of the measured normalized electric field autocorrelation function.
2. Dynamic selection of the optimum set of DCS signals.
3. Objective function for retrieving the dynamic information.

Each of these steps is performed during a non-linear least squared minimization of both method (LSQNONLIN with a Levenberg-Marqardt algorithm, MATLAB, The MathWorks Inc., USA); therefore a dynamic estimation of the optimum values for the β and D_b parameters can be obtained in a similar manner as for the DRS data (Section 4.1.3). A detailed description of each step is provided in the following sections.

4.2.1 *Estimation of the measured normalized electric field autocorrelation function*

As previously introduced (Chapter 2) the theoretical solution to the correlation diffusion equation (Equation 2.15) is given by the normalized electric field autocorrelation function $g_1^t(\tau, \rho_i^{DCS})$, where ρ_i^{DCS} stands for the theoretical signal at the i^{th} detection distance. However, in the experimental setups, the normalized intensity autocorrelation function $g_2^m(\tau, \rho_i^{DCS})$ is measured and hence; it must be converted to the measured normalized electric field autocorrelation function by means of the Siegert relation (Equation 2.14) to match the theoretical model, for which a β_i value per each measured signal is dynamically estimated during the minimization procedure.

Once it the β_i values have been determined, the measured normalized electric field autocorrelation function (g_1^m) can be determined as:

$$g_1^m(\tau, \rho_i^{DCS}) = \sqrt{\frac{g_2^m(\tau, \rho_i^{DCS}) - 1}{\beta_i}} \tag{4.15}$$

In this manner, Equation 4.15 can be fit to the theoretical normalized electric field autocorrelation function, given by the Equation 2.15 and repeated below to remind the reader, to reconstruct the dynamic information (e.g. flow) of the probed medium..

$$g_1^t(\tau, \rho_i^{DCS}) = \frac{\left(\frac{exp[-K(\tau)r_1]}{r_1} - \frac{exp[-K(\tau)r_b]}{r_b}\right)}{\left(\frac{exp[-K(\tau=0)r_1]}{r_1} - \frac{exp[-K(\tau=0)r_b]}{r_b}\right)} \tag{2.15}$$

with

$$K(\tau) = \sqrt{3\mu_s'\mu_a + 6k_0^2\mu_s'^2\alpha D_b\tau}$$

Equation 2.15 is fed with the reduced scattering (μ_s') and absorption (μ_a) coefficients estimated previously by DRS technique, whereas the

D_b parameter is dynamically estimated, along with the β_i values, during the same minimization procedure.

4.2.2 *Dynamic selection of the optimum set of DCS signals*

In the same fashion as for the DRS data processing, the measured normalized electric field autocorrelation function (g_1^m) that better resemble the theoretical model, named as the optimum set of DCS signals, have to be determined. To be selected as optimum, the DCS signals must met two criteria simultaneously:

1. The estimated β_i value must be within the 0.48 - 0.52 range ($\approx$ 4% error)
2. The mean percentage error (MPE_{DCS}) must be $\leq$5%

If one of the generated β_i values for a given detection distance (i) is not within the acceptance range (0.48 - 0.5) previously set, that signal would be discarded during the rest of the ongoing iteration of the minimization procedure. The remaining signals, denoted as $g_1^{m'}$, are then compared to the generated theoretical solution when the D_b being evaluated is fed into the theoretical model. The error between the measured $g_1^{m'}$ and the theoretical $g_1^{t'}$ signals at the remaining detection distances (i), is calculated through the mean percentage error (MPE) function as:

$$MPE_i = \frac{1}{N_\tau}\left(\sum_{j=1}^{N_\tau}\left|1 - \frac{g_1^{m'}(\tau(j), \rho_i^{DCS}))}{g_1^{t'}(\tau(j), \rho_i^{DCS})}\right| \times 100\right)\Bigg|_{i=1}^{N_{\rho^{DCS}}} \tag{4.16}$$

where $N_{\rho^{DCS}}$ refers to the number of remaining source-detection distances and N_τ is the total number of sampled time points in the autcorrelation function.

The functions $g_1^{m'}(\tau, \rho_i^{DCS})$ with an associated MPE_i lower or equal to 5%, denoted as $\overset{*}{g}_1^m$, fulfill the two selection criteria simultaneously and hence, represents the optimum set DCS functions. These function would be dynamically chosen during each iteration of the non-linear least squared minimization process.

We note that, for this procedure, if there are no measured normalized intensity autocorrelation functions g_1^m that satisfy simultaneously the established criteria, the whole set of functions with no restrictions for the β value are considered during the minimization process. However, a mark is set to further verify the quality of the fit and retrieved values.

4.2.3 *Objective function for retrieving the dynamic information*

During the dynamic selection of the optimum functions $\overset{*}{g}_1^m(\tau, \rho_i^{DCS})$, the employed objective function for retrieving the optimum β_i and D_b values of the probed medium is given by:

$$\chi^2 = \sum_{j=1}^{N_{\rho^{DCS}}} \sum_{i=1}^{N_\tau} \left[\overset{*}{g}_1^m(\tau, \rho_i^{DCS}) - \overset{*}{g}_1^t(\tau, \rho_i^{DCS}) \right]^2 \tag{4.17}$$

Where $N_{\rho^{DCS}}$ refers to the number of remaining source-detection distances, N_τ is the total number of sampled time points in the autcorrelation function and $\overset{*}{g}_1^m$ represents the theoretical solution when the optimum i detection distances are employed. Therefore, during this procedure, a full optimization of the β_i and D_b parameters as well as the DCS signals to be used is achieved, hence allowing an accurate reconstruction of the dynamic properties of the probed media.

5

DIFFUSE OPTICS FOR ANTIANGIOGENIC THERAPY MONITORING

Angiogenesis, the development of neovasculature, is a crucial mechanism through which vascular support is provided to the growing tumor mass to supply the metabolic demand of oxygen and nutrients for its proliferation [140–142]. The newly form vessels represent a key platform for tumor cell dissemination and metastasis [143]. The angiogenesis process is stimulated in a manifold of complex signaling pathways by the tumor [144]. The expression of the vascular endothelial growth factor (VEGF) [145] constitutes one of the most relevant factors associated to the formation of blood vessels. Over the last decades, the potential inhibition of the angiogenesis process has emerged as a novel therapeutic approach for cancer treatment [5, 17], giving rise to the development of anti-angiogenic drugs [146] aiming to deprive the tumor of oxygen and nutrients through the vascular trimming.

As mentioned before, the main model employed in this thesis is the clear cell renal cell carcinoma (ccRCC). The antiangiogenic inhibitors have indeed been employed in the clinics for the treatment of clear cell renal cell carcinoma tumors [23, 147, 148]; where Sunitinib [19] stands out as one of the most efficient first line antiangiogenic drugs [149]. The need for personalization and, hence, there relevance of my study arises because although around the 70% of the patients shows primary response to antiangiogenic therapies [150], cancer cells are able to adapt to the intratumor hypoxic environment induced by the antiangiogenic therapy [151] through several resistance mechanisms [7, 8, 152, 153], leading to an eventual tumor progression [154]. Unfortunately, this often times turns into a more aggressive tumor phenotype [155]. On the other hand, the rest of the patients (around 30%)

present an intrinsic resistance to the antiangiogenic therapy, meaning that the tumor has already activate some mechanisms to evade the action of the therapeutic agent. Due to this facts, further understanding of the underlying tumor biology and predictive biomarkers of therapy resistance are urgently needed in the clinics [156, 157].

In this regard, since the targeted anti-angiogenic drugs are characterized by the blockade of multiple pro-angiogenic signals [158], including the VEGF [17], for inhibiting the formation of novel blood-vessels; the associated microvascular hemodynamic changes are hypothesized to occur as the main signature of the therapeutic effects in the tumor [3]. Furthermore, the kinetics and magnitude of those changes might be indicative of either the tumor intrinsic resistance to the antiangiogenic agents or the adaptative process developed by the tumor to become therapy resistant [159]. Therefore, monitoring of tissue physiology might provide insights about not only the therapy response at early stages but also regarding the fundamental biological processes governing the tumor resistance [157].

My study is motivated by the fact that diffuse optical techniques have been demonstrated as a set of potential tools capable to provide longitudinal and non-invasive monitoring of tissue hemodynamics in translational oncology [2, 109, 160, 161]. In this chapter, I introduce the diffuse optical methods to monitor non-invasively the longitudinal tissue hemodynamics changes in a pre-clinical ccRCC mouse model undergoing Sunitinib treatment. The recovered tumor hemodynamic changes are demonstrated to be a suitable set of potential biomarkers capable of providing early information associated not only with the final therapy effects but also with the therapy response. Furthermore, in the following sections, the prediction of therapy resistance to antiangiogenic drugs from the tumor hemodynamics estimated before treatment is deployed as a potential biomarker to bridge the gap of the oncology research to determine resistance in order to develop personalized therapeutic approaches.

5.1 METHODS AND PROTOCOLS

The animal procedures were approved by the ethical committee of the Bellvitge Biomedical Research Institute - IDIBELL (CEIC - Comité Ético de Investigaciíon Clínica del Hospital Universitario de Bellvitge) and accepted by the local Catalan government (Generalitat de Catalunya, Departament de Medi Ambient i Habitatge, Direcció General del Medi Natural, Protocol number: 4899, PI: Oriol Casanovas).

5.1.1 *Orthotopic implantation of ccRCC tumors*

A primary kidney tumor sample of clear cell renal cell carcinoma (ccRCC) from a human donor, categorized as Fuhrman grade 4/4 and pathological staging PT4, was obtained after surgical nephrectomy at Vall d'Hebron Hospital under local ethics committee's approved protocols (CEIC approvals references PR322/11 and PR[AG]240/2013). Afterwards, biopsies from the most viable region - avoiding the necrotic and hemorrhagic zones - were obtained and preserved.

A host athymic mouse (Harlan Laboratories, Spain, weight: 23.4 – 31.1 g, age: 5 weeks) underwent a surgically procedure [162, 163] for suturing one of the preserved human kidney tumor samples to the mouse left flank kidney, afterwards, the tumor was allowed to grow. Once the tumor reached a volume of $\approx$ 1500 mm^3 - about ten weeks after implantation - the host mouse was sacrificed, and the tumor was excised. The most viable part of the extracted tumor was sectioned into pieces of $\approx 2\times2\times2$ mm^3 and frozen at - 80°C for preservation. This process closely mimics the procedure described in Ref. [164] and aims to preserve the tumor stromal characteristics; hence resembling the original human tumor architecture.

The frozen tumor samples were implanted in a set (N = 37) of immunodepressed mice (Harlan Laboratories, Spain, weight: 23.4 – 31.1 g, age: 5 weeks) that were employed in the here reported work. To this end, all mice followed a surgical procedure for exposing the left kid-

ney. The preserved tumor samples from the host mouse were sutured to the exteriorized kidney; then the organ was returned to the abdominal cavity. The skin and muscles were sutured with surgical staples. Once the wound healed, the staples were removed. The tumors were left to grow to a volume of $\approx$1000 mm^3 - about seven weeks after implantation - before starting the measurements. The details about tumor implantation can be found in Ref. [7].

The human tumor resection and the preservation process was performed from physicians and biologist of Vall d'Hebron Hospital and IDIBELL. The whole procedure of the tumor implantation and growth was performed at IDIBELL facilities by technician Mar Martínez Lozano.

5.1.2 *Animal population and dosage*

A total of 37 immunodepressed male athymic nude mice (Harlan Laboratories, Spain, weight: 23.4 – 31.1 g, age: 5 weeks) were randomly assigned either to the control or treated group. The treated (N = 22) group received Sunitinib (S-8803 Sunitinib Malate, LC Labs, USA) antiangiogenic therapy in a daily basis with a dosage of 40 mg/kg/day by oral gavage. On the other hand, the control (N = 15) group received carboxymethylcellulose vehicle formulation in the same dosage and administration frequency. All the mice were treated over a period of twenty-one days in which they were fed and maintained in a specific pathogen-free (SPF) environment at the animal facility. The administration of the daily dosage was performed by PhD. Gabriela Jiménez Valerio at IDIBELL facilities.

5.1.3 *Measurement protocol*

The hybrid contact DRS/DCS device introduced in Chapter 3 was utilized for collecting the optical data. During the measurement period, mice were kept anesthetized with a mixture of isoflurane and

oxygen (4% isoflurane and 2 L/min of oxygen for induction and 2% isoflurane and 2 L/min of oxygen for maintaining) and their body temperature remained stabilized at 34°C and monitored by means of a heating blanket with a rectal temperature sensor feedback (PS-03, PhysioSuite, MouseSTAT Pulse Oximeter, Kent Scientific, USA).

The DRS/DCS data was collected from each mouse at two different locations: shoulder and tumor. In the shoulder, optical data was collected five times from the same position. In the tumor, five different positions were probed, where the last one corresponds to the probe placed at the top center of the tumor and the rest, in reference to it, to the cardinal points surrounding it. The DRS optical data was acquired at six source-detector separations ranging from 0.2 to 0.5 cm over a wavelength range from 600 to 1000 nm. The DCS data was acquired from a set of six source-detector separations ranging within the same detection range as the DRS device. The DRS/DCS data acquisition from the ten measured locations (5 in the shoulder + 5 in the tumor) lasted $\approx$ 10 minutes.

The optical data was acquired from day zero to day five and on days seven, ten, fourteen, seventeen and twenty. The day zero corresponds to the baseline measurement and to the first day of treatment; therefore the measurement days reflects the effect of the previous day of treatment.

5.1.4 *Therapy response classification*

To evaluate the anti-angiogenic therapy effect, the tumor volume from each mouse was estimated on days zero, three, seven, eleven, fourteen, seventeen and twenty through palpation (the standard preclinical method). In this regard, the treated (N = 22) group of mice showed a relatively flat trend over the time course, whereas the control (N = 13) group was observed to have a growing trend over time. However, some mice belonging to the treated group were found to have an increasing tumor volume trend, surpassing a 25% increment ($\geq$ 1250

mm^3) with respect to their initial tumor volume, even under antiangiogenic treatment which was expected to control the tumor volume. According to this criteria, the mice in the treated group were classified into two groups: the responder (N = 14) group - the tumor volume did not increase more than 25% with respect to its initial volume - and the non-responder (N = 8) group - the tumor volume increased more than 25% with respect to its initial volume - which conformed the therapy outcome group. The palpation procedure was performed by PhD. Gabriela Jiménez Valerio at IDIBELL facilities.

5.1.5 *Data processing*

In the data analysis, the water (H_2O) absorption spectrum [50] and the molar absorption coefficients of the oxy- (HbO_2) and deoxy (Hb) hemoglobin (600 - 650 nm [49], 651 - 1000 nm [50, 51]) were employed for retrieving the chromophore concentrations from all the experiments. To this end, numerical fitting was done for the A_0, b and c_i coefficients using a non-linear least square minimization method (LSQNONLIN with Levenberg-Marqardt algorithm, MATLAB, The MathWorks Inc., USA). For a detailed description of the optical data processing method, please see Section 4.1.

In the DCS optical data processing, the β and D_b parameters were numerically fit for retrieving the flow information by using the same non-linear least square minimization method (LSQNONLIN with Levenberg-Marqardt algorithm, MATLAB, The MathWorks Inc., USA) as the DRS data. For a detailed description of the optical data processing method, please see Section 4.2.

5.1.6 *The ex vivo tumor characterization & histology*

At the end of the twenty-one days of the experiment, each mouse was sacrificed and the tumor was extracted. The extracted tumor

weight (TW) and final volume (FTV) were estimated by a digital scale and water displacement in a graduated cylinder, respectively. Afterward, the tumor samples were fixed in formalin and embedded in paraffin. Several tumor slices of 4 μm were cut using a microtome system (Leica RM 2125RT, Leica Microsystems, Germany) and mounted on glass slides for histological analysis. A cluster of differentiation 31 (CD31) staining was utilized for recovering the micro vessel density (MVD) by acquiring an image of each of the five most viable regions - avoiding hemorrhagic zones - of a representative tumor slide at 20x magnification with an optical microscope (NIKON-801 DS-Ri1, NIKON, Japan). The acquired images were processed (ImageJ, National Institute of Health, USA) for estimating the micro vessel density (MVD) [$^{vessels}/_{field}$] as the number of vessels per viable field. The same procedure was repeated in a different tumor slice by applying a hematoxylin and eosin (H&E) staining for estimating the necrosis percentage (NP) as the ratio of the pixels corresponding to necrotic zones in each of the five images to the total number of pixels in the set of images multiplied by hundred. The *ex vivo* tumor samples collection and the data analysis were performed by PhD. Gabriela Jiménez Valerio at IDIBELL facilities.

5.1.7 *Statistical Analysis*

Statistical analyses were performed using the R statistical software [165]. The estimated DRS/DCS results were expressed as the mean $\pm$ standard error of the mean (SEM) over the assessed position; either the tumor or the shoulder. In Section 5.2.4.1, the pre-treatment tissue hemodynamics of the therapy groups and measured positions were statistically characterized by means of a Kruskal-Wallis test. In Section 5.2.2, a linear mixed-effect model (LME) was employed for assessing the differences in the tumor volume over days among the components of both the therapy (treated and control) and outcome (responder, non-responder and control) groups. In Section 5.2.4, a Kruskal-Wallis test

was used for statistically assessing the therapeutic effect of the *ex vivo* results obtained from the histological analysis (FTV, TW, MVD and NP). In Section 5.2.4.2, a Kruskal-Wallis test was conducted over the log-transformed tumor hemodynamic parameters (THC, SO_2 and BFI) for assessing the statistical differences among therapy outcome groups. Besides, a bootstrap test (p_{bs}) was performed to determine the validity of the statistical results.

Furthermore, the tumor hemodynamic values from each mouse in the responder and non-responder groups were transformed through a *z-score* normalization method. To this end, the data was log transformed first, then the global mean and standard deviation of a given hemodynamic parameter in both therapy outcome groups (responder and non-responder) at the shoulder position were computed. The global average shoulder value was subtracted from the mean tumor hemodynamic value of each mouse; then divided by the estimated global standard deviation. The *z-score* normalized data was then fitted by a logistic binomial regression for assessing the pre-treatment classification potential of the predicted therapy outcome by the measured tissue hemodynamics. The statistical significance of the recovered classification was validated through a bootstrap analysis (p_{bs}).

In Sections 5.2.4.3 and 5.2.4.4, a linear mixed-effects (LME) model was employed to statistically interrogate the relevance of the recovered tissue hemodynamic changes. Furthermore, the predicted values from the corresponding LME model, inherently containing the time correlation information, were employed to determine through a Kruskal-Wallis test the time point where a statistical distinction between therapy (Section 5.2.4.3) and outcome (Section 5.2.4.4) groups was achieved, respectively. Besides, in both sections, a bootstrap test (p_{bs}) was conducted to validate the recovered statistical results.

In Section 5.2.4.4, the observed plateau region in the tumor hemodynamics was determined through a paired t-test among treatment days. Finally, in Section 5.2.4.5, the Pearson's correlation coefficient was employed to quantify the linear correlation agreement between the early

changes in the tissue hemodynamics and the *ex vivo* histology results. A star indicates the statistically significant differences (*, $p < 0.05$).

5.2 RESULTS

5.2.1 *Experimental population*

A total of 37 mice, assigned either to the control or treated groups, started the experiment under the schedule and doses introduced in Section 5.1.2. During the course of the experiment, two mice belonging to the control group needed to be sacrificed on day 11 of treatment due to health conditions in accordance with the ethical protocol. The collected hemodynamic information from these mice was discarded from the results to avoid any bias. Therefore, the following results encompass the information from a total of N = 35 mice assigned to the control (N = 13) and treated (N = 22) groups.

5.2.2 *Tumor volume & therapy response*

The tumor volume assessed by palpation at different days over the experiment is shown in Figure 5.1. When evaluating the therapy effect on the tumor volume (Figure 5.1a), a statistically significant difference ($p < 0.01$) between the control (N = 13) - black line - and treated (N = 22) - red line - groups estimated was observed. On the other hand, when assessing the tumor volume from each therapy outcome group (Figure 5.1b), no statistically significant difference ($p = 0.83$) between the control and non-responder groups was observed. Besides, the responder group was found to be statistically significant different from both the control and the non-responder groups ($p < 0.01$).

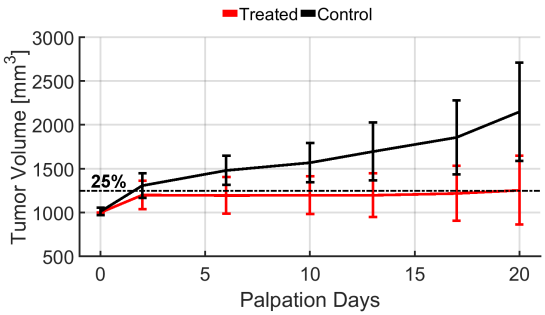

(a) Tumor volume by therapy groups

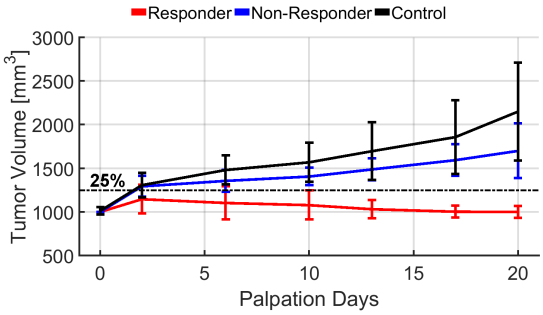

(b) Tumor volume by therapy outcome

Figure 5.1: Tumor volume over time assessed by palpation. The tumor volume assessed by palpation at several time points over the experiment. a) The tumor volume over time of the treated and control groups and b) The tumor volume over time of the treated but non-responder mice, with respect to the responder and control groups. Data is represented as the mean ± std over mice in the given group.

5.2.3 *Effects of antiangiogenic therapy in the tumor: ex vivo characterization & histology*

In Figure 5.2a, the final tumor volume (FTV) of the extracted tumor samples was observed to be statistically significant different ($p < 0.01$) between the responder - red markers - and non-responder - blue markers - groups, as well as between the responder and control - black markers - groups ($p < 0.01$). However, no statistically significant differ-

ence ($p = 0.98$) was observed between the non-responder and control groups.

In Figure 5.2b, the final tumor weight (TW) of the extracted tumor samples was observed to be statistically significant different ($p < 0.01$) between the responder and non-responder groups, as well as between the responder and control groups ($p < 0.01$). However, no statistically significant difference ($p = 0.51$) was observed between the non-responder and control groups.

In Figure 5.2c, the micro vessel density (MVD) of the extracted tumor samples was observed to be statistically significant different ($p < 0.01$) between the responder and non-responder groups, as well as between the responder and control groups ($p < 0.01$). However, no statistically significant difference ($p = 0.56$) was observed between the non-responder and control groups.

In Figure 5.2d, the necrosis percentage (NP) of the extracted tumor samples was observed to be statistically significant similar ($p \geq 0.17$) among all therapy outcome groups.

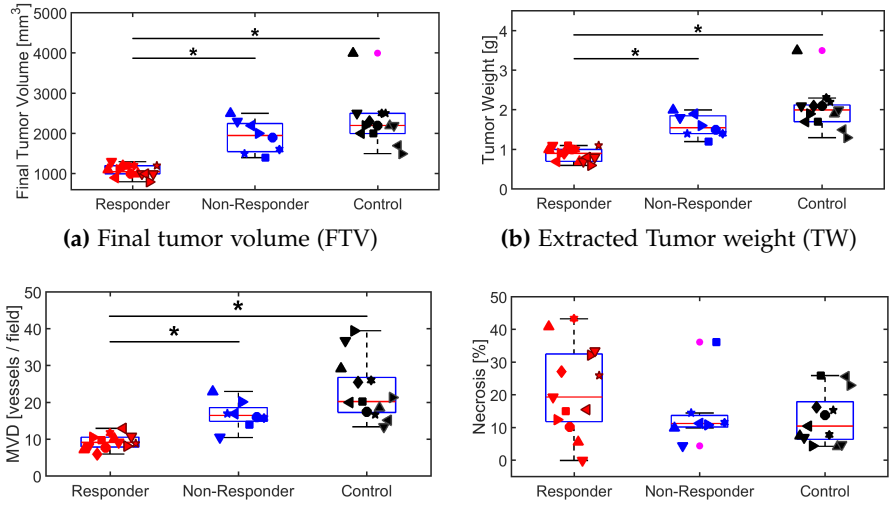

(a) Final tumor volume (FTV)

(b) Extracted Tumor weight (TW)

(c) Final micro vessel density (MVD)

(d) Final tumor necrosis percentage (NP)

Figure 5.2: Tumor *ex vivo* results: characterization & histology. The *ex vivo* recovered tumor samples demonstrates a statistically significant difference ($p < 0.01$) of the responder group with respect to the non-responder and control groups in the final tumor volume (a), tumor weight (b) and micro vessel density (c), whereas the same parameters (a,b and c) in the non-responder and control groups were observed to be statistically significant similar ($p \geq 0.51$). On the other hand, no statistically significant difference ($p \geq 0.17$) in the necrosis percentage (d) among all therapy outcome groups (responder, non-responder and control) was observed.

A summary of the tumor histology statistics among therapy outcomes is shown in Table 5.1.

Group	FTV	TW	MVD	NP
Responder - Non-Responder	<0.01	<0.01	0.01	0.50
Responder - Control	<0.01	<0.01	<0.01	0.17
Non-Responder - Control	0.98	0.51	0.56	0.98

Table 5.1: Tumor histology statistics among therapy outcomes.

5.2.4 *Tissue hemodynamics monitoring: in vivo results*

The *in vivo* retrieved tissue hemodynamics by DRS/DCS techniques at several time points and categorized by therapy (treated and control groups) and outcome (responder and non-responder groups) are described in the following sections.

5.2.4.1 *Pre-treatment tissue characterization: in vivo*

The estimated pre-treatment tissue hemodynamics (THC, SO_2 and BFI) were characterized to determine the initial distribution of the physiological parameters. In this regard, the pre-treatment tumor hemodynamics (THC: 75.71 $\pm$ 30.14 μM, SO_2: 75.05 $\pm$ 9.14 % and BFI: 2.81 $\pm$ 1.28 10^{-8} cm^2 s^{-1}) were observed to be statistically significant higher ($p \leq 0.01$) in comparison with the shoulder values (THC: 38.86 $\pm$ 5.43 μM, SO_2: 51.75 $\pm$ 4.66 % and BFI: 1.96 $\pm$ 0.94 10^{-8} cm^2 s^{-1}) as shown in Figure 5.3.

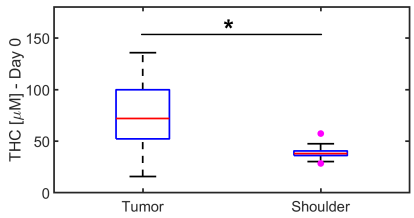

(a) Pre-treatment total hemoglobin concentration (THC)

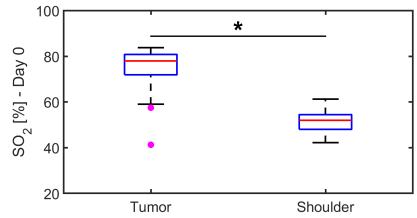

(b) Pre-treatment oxygen saturation (SO_2)

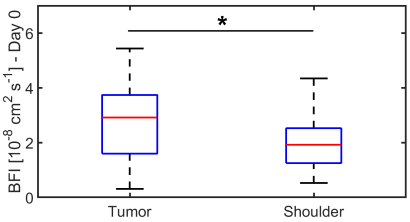

(c) Pre-treatment blood flow index (BFI)

Figure 5.3: Pre-treatment tissue hemodynamic characterization by position. The pre-treatement recovered tissue hemodynamics (THC, SO_2 and BFI) in the tumor position were observed to be statistically significant higher ($p < 0.01$) than those at the shoulder position.

On the other hand, the pre-treatment tissue hemodynamics between the treated and control groups were also investigated (Figure 5.4). In this regard, no statistically significant differences ($p \geq 0.25$) were observed between the estimated pre-treatment tumor hemodynamics (left column) of the treated (THC: 77.12 ± 26.83 μM, SO_2: 75.38 ± 6.76 % and BFI: 3.00 ± 1.20 10^{-8} cm^2 s^{-1}) and control (THC: 73.31 ± 36.09 μM, SO_2: 74.47 ± 12.49 % and BFI: 2.48 ± 1.38 10^{-8} cm^2 s^{-1}) groups. Besides, the pre-treatment shoulder hemodynamics (right column) were also noticed to be statistically significant similar ($p \geq 0.20$) between the treated (THC: 37.95 ± 4.38 μM, SO_2: 51.14 ± 4.71 % and BFI: 2.10 ± 1.00 10^{-8} cm^2 s^{-1}) and control (THC: 40.40 ± 6.77 μM, SO_2: 52.79 ± 4.58 % and BFI: 1.72 ± 0.81 10^{-8} cm^2 s^{-1}) groups.

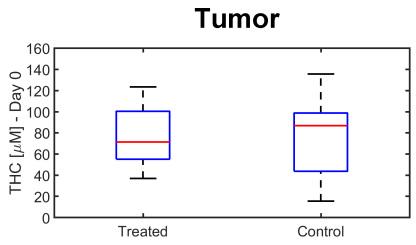

(a) Pre-treatment tumor total hemoglobin concentration (THC)

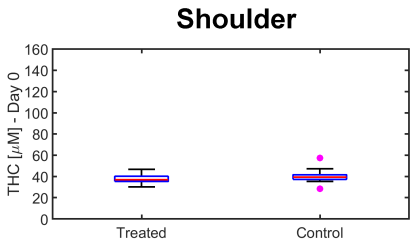

(b) Pre-treatment shoulder total hemoglobin concentration (THC)

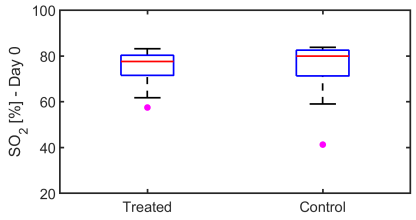

(c) Pre-treatment tumor oxygen saturation (SO_2)

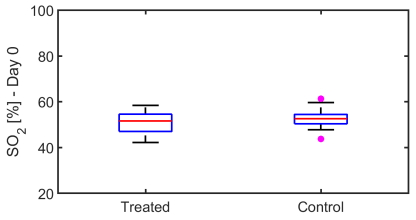

(d) Pre-treatment shoulder oxygen saturation (SO_2)

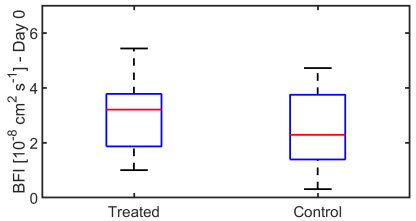

(e) Pre-treatment tumor blood flow index (BFI)

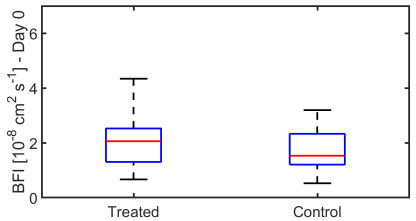

(f) Pre-treatment shoulder blood flow index (BFI)

Figure 5.4: Pre-treatment tissue hemodynamic characterization by therapy. The pre-treatement recovered tumor hemodynamics (THC, SO_2 and BFI) were observed to be statistically significant similar ($p \geq 0.25$) regardless the therapy group (treated or control) as shown in the left column; whereas the shoulder hemodynamics (right column) were observed to be statistically significant similar ($p \geq 0.20$) between the treated and control groups..

5.2.4.2 *Pre-treatment prediction of therapy outcome: in vivo results*

The estimated blood flow index (BFI) at the pre-treatment time point (day zero) in the responder group (2.56 ± 1.04 cm^2 s^{-1}) seems to be lower than that in the non-responder (3.77 ± 1.12 cm^2 s^{-1}) group. Nevertheless, the data shows a skewed distribution. To overcome this issue, the recovered BFI values were log-transformed to assess the difference between outcome groups statistically. In this regard, a statistically significant difference ($p = 0.01$), with a statistically significant bootstrap $p_{bs} < 0.05$, was observed as shown in Figure 5.5. Furthermore, no statistically significant differences were observed between any of the therapy outcome groups, either the responder or the non-responder, with respect to the control group ($p = 0.88$ and $p = 0.09$, respectively). On the other hand, the log-transformed total hemoglobin concentration (THC) values in the tumor (data not shown) did not show any statistically significant difference between the responder and non-responder group ($p = 0.17$); whereas both groups were observed to be statistically significant similar to the control group ($p = 0.77$ and $p = 0.46$, respectively). Besides, the log-transformed tumor oxygen saturation (SO_2) values were also observed to be statistically similar between the responder and non-responder groups ($p = 0.21$), whereas no statistically significant differences were noticed from any therapy outcome group - responder and non-responder - with respect to the control group ($p = 0.20$ and $p = 0.77$, respectively).

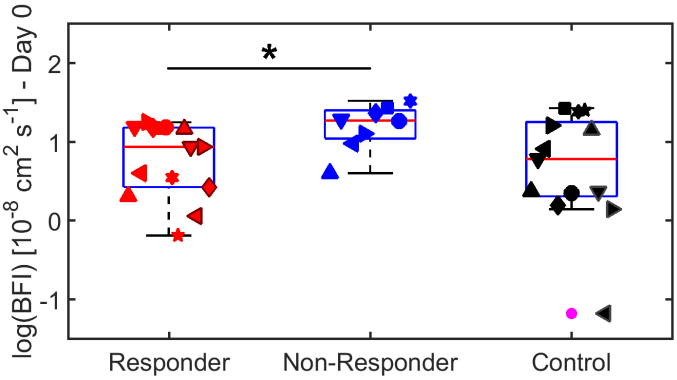

Figure 5.5: Pre-treatment discrimination of therapy outcome. The log transformed blood flow index (BFI) before starting the administration of the antiangiogenic treatment (day zero) allows for the statistical differentiation (p = 0.01) between the responder and non-responder groups.

A summary of the pre-treatment tumor hemodynamics statistics among therapy outcomes is shown in Table 5.2.

Group	log(THC)	log(SO_2)	log(BFI)
Responder - Non-Responder	0.17	0.21	0.01
Responder - Control	0.77	0.20	0.88
Non-Responder - Control	0.46	0.77	0.09

Table 5.2: Pre-treatement tumor hemodynamics statistics among therapy outcomes.

Beyond the statistical tests introduced above, the uni- and multivariate statistical analysis of the *z-score* [166] transformed tumor hemodynamics at the pre-treatment time point (Figure 5.6) were assessed. In Figure 5.6a, a statistically significant model (p = 0.01) based on the univariate tumor blood flow index shows an area under the curve (AUC) of 0.81. This results were validated by a $p_{bs} < 0.03$. On the other hand, the tumor total hemoglobin concentration (THC) and oxygen saturation (SO_2) univariate models were observed not to be sta-

tistically significant (p = 0.15 and p = 0.14, respectively); hence, the recovered AUCs were rejected. Besides, the multivariate analysis of the estimated tumor hemodynamics demonstrated a statistically significant model (p = 0.04) for the combined THC & BFI parameters (Figure 5.6b) with an AUC of 0.79. This results were validated by a $p_{bs} < 0.049$. On the other hand, the multivariate models composed by the THC & SO_2 and BFI & SO_2 were determined to be not statistically significant (p = 0.32 and p = 0.052, respectively); therefore the results from both models were discarded.

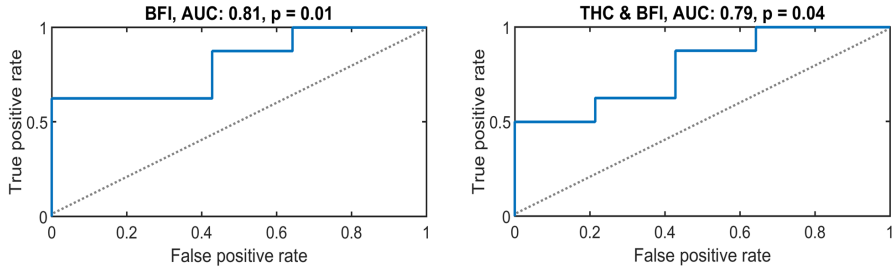

(a) AUC for univariate BFI **(b)** AUC for multivariate THC & BFI

Figure 5.6: Therapy outcome classification based on pre-treatment tumor hemodynamics. The therapy outcome classification by a binomial logistic regression of the pre-treatment tumor hemodynamics: a) The univariate binomial logistic regression model (p = 0.01 and $p_{bs} \leq 0.032$) of the tumor BFI showed an AUC of 0.81; and b) The multivariate binomial logistic regression model (p = 0.047 and $p_{bs} \leq 0.049$) of the combined tumor THC & BFI parameter showed an AUC of 0.79.

A summary of the uni- and multi- variate binomial logistic regression of the tumor hemodynamics at the pre-treatment time point for the therapy outcome classification is shown in Table 5.3.

Univariate				Multivariate			
Parameter	**AUC**	**p**	$\mathbf{p}_{bs}$	**Parameter**	**AUC**	**p**	$\mathbf{p}_{bs}$
THC	0.68	0.15	≥ 0.07	**THC & BFI**	0.79	0.047	≤ 0.049
SO_2	0.68	0.14	≥ 0.07	**THC & SO_2**	0.67	0.320	≥ 0.190
BFI	0.81	0.01	≤ 0.03	**BFI & SO_2**	0.79	0.052	≥ 0.050

Table 5.3: Pre-treatement therapy outcome classification by binomial logistic regression.

5.2.4.3 *Effect of anti-angiogenic therapy in the tissue hemodynamics: in vivo results*

The treated (N = 22) - red line - and control (N = 13) - black line - groups of mice were assessed by DRS/DCS techniques over several time points where Sunitinib therapy-derived hemodynamic changes were observed. In general, in Figure 5.7, the hemodynamic parameters (THC, SO_2 and BFI) were observed to be affected by the antiangiogenic drug in the tumor location (left column); whereas in the shoulder location (right column), no statistically significant differences were observed in any hemodynamic parameter.

In Figure 5.7a, a statistically significant difference ($p < 0.01$) between the treated and control group was observed in the total hemoglobin concentration (THC) retrieved from the tumor location over the experiment course with a statistically significant difference ($p = 0.03$, $p_{bs} \leq 0.048$) from day seven onwards. In contrast, no statistically significant difference ($p = 0.87$) in the estimated total hemoglobin concentration in the shoulder location was observed (Figure 5.7b). Furthermore, in the tumor, a mean THC value of 67.99 ± 35.06 μM was recovered from the control group, whereas the treated group showed a mean value of 47.43 ± 30.04 μM during the whole experiment. Besides, in the shoulder location, a mean THC value of 39.99 ± 8.41 μM was recovered from the control group, whereas the treated group showed a mean value of 40.41 ± 7.66 μM during the experiment.

In Figure 5.7c, a statistically significant difference ($p = 0.01$) between the treated and control group was observed in the oxygen saturation (SO_2) retrieved from the tumor location over the experiment course with a statistically significant difference ($p = 0.03$, $p_{bs} \leq 0.03$) from day ten onwards. In contrast, no statistically significant difference ($p = 0.71$) in the estimated oxygen saturation in the shoulder location was observed (Figure 5.7d). Furthermore, in the tumor, a mean SO_2 value of 73.70 ± 10.96 % was recovered from the control group, whereas the treated group showed a mean value of 70.08 ± 9.24 % during the whole experiment. Besides, in the shoulder, a mean SO_2 value of 54.11 ± 5.23 % was recovered from the control group, whereas the treated group showed a mean value of 54.41 ± 5.57 % during the experiment. Finally, in Figure 5.7e, a statistically significant difference ($p < 0.01$) between the treated and control group was observed in the blood flow index (BFI) retrieved from the tumor location over the experiment course with a statistically significant difference ($p = 0.02$, $p_{bs} \leq 0.02$) from day fourteen onwards. In contrast, no statistically significant difference ($p = 0.52$) in the estimated blood flow index in the shoulder location was observed (Figure 5.7f). Furthermore, in the tumor, a mean BFI value of 2.88 ± 1.66 [10^{-8} cm^2 s^{-1}] was recovered from the control group, whereas the treated group showed a mean value of 2.26 ± 1.42 [10^{-8} cm^2 s^{-1}] during the whole experiment. Besides, in the shoulder, a mean BFI value of 2.44 ± 1.30 [10^{-8} cm^2 s^{-1}] was recovered from the control group, whereas the treated group showed a mean value of 2.69 ± 1.37 [10^{-8} cm^2 s^{-1}] during the experiment.

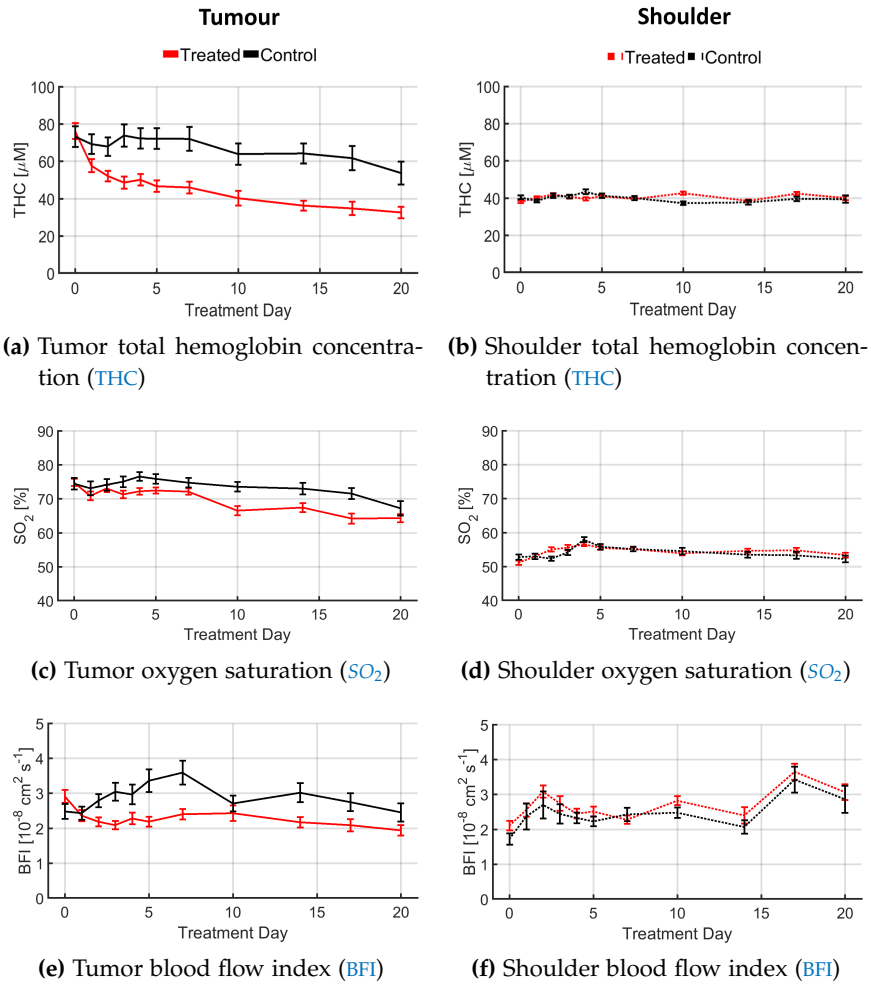

(a) Tumor total hemoglobin concentration (THC)

(b) Shoulder total hemoglobin concentration (THC)

(c) Tumor oxygen saturation (SO_2)

(d) Shoulder oxygen saturation (SO_2)

(e) Tumor blood flow index (BFI)

(f) Shoulder blood flow index (BFI)

Figure 5.7: Anti-angiogenic therapy effects on tissue hemodynamics. The *in vivo* recovered tissue hemodynamics from the treated and control groups. In general, the estimated tumor hemodynamics (THC, SO_2 and BFI) were observed to be statistically significant different ($p \leq 0.01$) from those at the shoulder. Moreover, no statistically significant differences ($p \geq 0.52$) were observed in the shoulder hemodynamics between treated and control groups.

5.2.4.4 *Therapy outcome discrimination by tissue hemodynamics: in vivo results*

Based on the palpated tumor volume over days (Figure 5.1b), the treated (N = 22) group of mice was divided into two groups according to the therapy outcome; the responders (N = 14), and the non-responders (N = 8) groups. In Figure 5.8, the tissue hemodynamics from each of these groups is shown; besides, the control group - black line - hemodynamics are also shown as a reference value.

In Figure 5.8a, no statistically significant difference ($p = 0.46$) in the tumor total hemoglobin concentration (THC) between the responder and non-responder groups was observed; hence, no statistical distinction between those outcomes was recovered at any time point ($p \geq 0.10$). In the retrieved THC values from the shoulder location (Figure 5.8b), no statistically significant difference ($p = 0.69$) was observed between the responder and non-responder groups.

In Figure 5.8c, a statistically significant difference ($p = 0.04$) in the tumor oxygen saturation (SO_2) between the responder and non-responder groups was observed over time with a statistically significant difference ($p = 0.04$, $p_{bs} \leq 0.04$) from day fourteen onwards. Moreover, the non-responder group was determined to be statistically significant similar ($p = 0.77$) to the control group. In the retrieved SO_2 values from the shoulder location (Figure 5.8d), no statistically significant difference ($p = 0.51$) was observed between the responder and non-responder groups.

In Figure 5.8e, no statistically significant difference ($p = 0.68$) in the tumor blood flow index (BFI) between the responder and non-responder groups was observed; hence, no statistical distinction was recovered at any time point ($p \geq 0.08$). In the retrieved BFI values from the shoulder location (Figure 5.8f), no statistically significant difference ($p = 0.34$) was observed between the responder and non-responder groups.

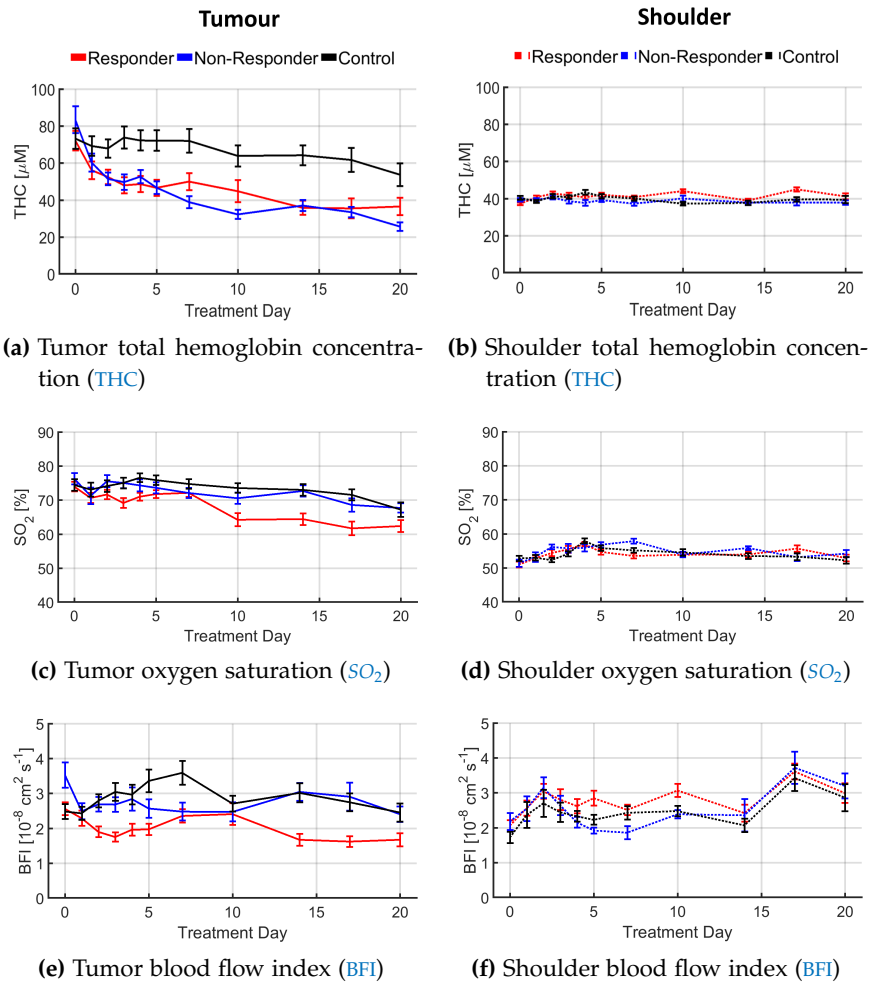

(a) Tumor total hemoglobin concentration (THC)

(b) Shoulder total hemoglobin concentration (THC)

(c) Tumor oxygen saturation (SO_2)

(d) Shoulder oxygen saturation (SO_2)

(e) Tumor blood flow index (BFI)

(f) Shoulder blood flow index (BFI)

Figure 5.8: Therapy outcome discrimination by the estimated tissue hemodynamics. The *in vivo* recovered tissue hemodynamics from the therapy outcome groups. In the tumor location (left column): The THC (a) and BFI (e) parameters of the therapy outcome group were observed to be statistically significant similar ($p = 0.46$ and $p = 0.68$ respectively) between them over the experiment time course, whereas the SO_2 (c) showed a statistically significant difference ($p = 0.04$) between responder and non-responder groups. In the shoulder location (right column): No statistically significant differences ($p \geq 0.34$) were observed in the estimated hemodynamics (b,d,f) between the responder and non-responder groups during the experiment.

5.2.4.5 *Early prediction of the therapy effect by tissue hemodynamics: in vivo results*

The *in vivo* recovered tumor hemodynamics by means of non-invasive DRS/DCS techniques, as hypothesized, were observed to be affected by the administration of the therapeutic drug which aims to create a vascular trimming, mainly, through the blockage of the VEGF receptor. Besides, the shoulder hemodynamics remained unaltered during the experiment as discussed in Sections 5.2.4.3 and 5.2.4.4. Therefore, the early noticed tumor hemodynamic changes were investigated as potential biomarkers of the therapy effects. In this regard, the change in the tumor blood flow index (BFI) at day 3 with respect to the baseline - day zero - values (Δ = Day 3 - Day 0) was observed to be correlated with the final tumor micro vessel density (R^2: 0.17, p = 0.017). In addition, the change in the tumor total hemoglobin concentration (THC) between the same time points, was observed to be associated with the extracted tumor weight (R^2: 0.15, p = 0.023), as shown in Figure 5.9.

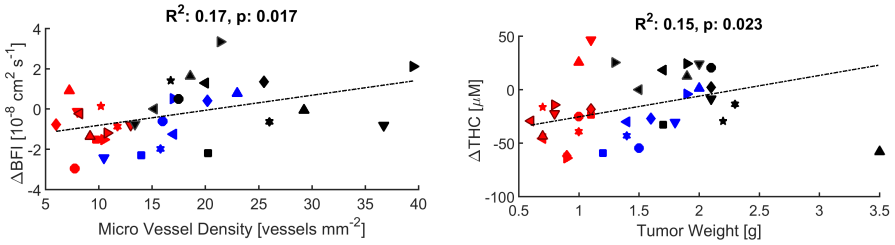

(a) Blood flow index (BFI) change

(b) Total hemoglobin concentration (THC) change

Figure 5.9: Early tissue hemodynamics changes predict the antiangiogenic therapy effect. The changes at day three after treatment (Δ = Day 3 - Day 0) of the *in vivo* recovered blood flow index (BFI) and total hemoglobin concentration (THC) parameters were observed to correlate with the *ex vivo* tumor characteristics: a) The initial tumor BFI change was observed to correlate with the histology recovered tumor micro vessel density (MVD), b) The initial tumor THC was observed to correlate with the extracted tumor weight (TW).

5.3 DISCUSSION

Diffuse optical techniques have been employed to investigate the *in vivo* tissue hemodynamic changes as response to antiangiogenic therapy administration. To this end, an advanced orthoxenograft pre-clinical mouse model of clear cell renal cell carcinoma (ccRCC) derived from a human tumor sample was employed to preserve the original tumor characteristics [162–164], hence the results here obtained are potentially translatable to the clinics.

In this experiment, tumor hemodynamic changes derived from the administration of Sunitinib [19, 149], a multitargeted receptor tyrosine kinase (RTKs) that blocks the VEGF to inhibit new blood-vessels formation [144], were demonstrated to occur as a therapeutic effect through the tissue monitoring by diffuse optical techniques DRS/DCS. These changes were then hypothesized to provide relevant insights about the tumor biology; being a set of potential biomarkers associated with the therapy response and prognosis.

In this regard, the tumor palpated volume over time (Figure 5.1a) was observed to be statistically significantly different between the treated and control groups ($p < 0.01$). Also, in some treated mice the tumor volume was not successfully controlled by the antiangiogenic agent (Sunitinib) and continue to grow during the experiment (Figure 5.1b). This behavior has been previously reported both in human [25, 167, 168] and pre-clinical [169] studies, being associated with the tumor resistance mechanisms [152].

The histological analysis of *ex vivo* tumor samples (Figure 5.2), collected from each of the therapy outcome groups, confirm the similarity between the non-responder and control groups, whereas the responder group was observed to be systematically different from the others, except in the tumor necrosis percentage (NP) parameter (Figure 5.2d). These results might arise from the fact that Sunitinib therapeutic mechanism resides on the inhibition of the neovasculature formation; hence, slowing down the tumor growth and reducing the final tumor volume

and weight. The non-responder tumors might be capable of overcoming the vascular trimming targeted by Sunitinib drug through several mechanisms of resistance [7, 152, 156] to keep generating new vasculature, leading to an increased MVD. On the other hand, the similarity in the tumor NP among therapy outcome groups might be derived from a combined effect of two factors; first, the vascular trimming in the responder group could lead to the formation of necrotic areas by depriving the tumor from nutrients carried by the blood-stream and second; the large tumor volumes of the non-responder and control groups could lead to the natural formation of necrotic regions that might reach similar necrotic percentages to those in the responder group.

Along the same lines, the *in vivo* tissue hemodynamics (THC, SO_2 and BFI) were non-invasively monitored by DRS/DCS optical techniques during the experimental period. The estimated pre-treatment tumor hemodynamic parameters were observed to be statistically significantly higher ($p \leq 0.01$) in comparison with the shoulder position (Figure 5.3). These findings might be associated with the overexpression of VEGF and other pro-angiogenic factors in the tumor, which allows the development of an extended vascular network [170]. On the other hand, the estimated pre-treatment tissue hemodynamics of the treated and control groups in the tumor and shoulder location (Figure 5.4) were observed to be statistically similar ($p \geq 0.25$ and $p \geq 0.20$, respectively), indicating the physiological similarity between and within therapy groups.

Beyond the general characterization of the pre-treatment hemodynamics of the therapy groups (treated and control), the differences between the therapy outcome groups - responder and non-responder - were of our interest as potential predictors of the tumor resistance before administration of Sunitinib drug. In this regard, the observed statistical difference between the responder and non-responder groups in the pre-treatment, log-transformed blood flow index (BFI) parameter (Figure 5.5), in addition to the recovered area under the curve

(AUC) obtained from the uni-variate BFI (AUC: 0.81, p = 0.01) parameter (Figure 5.6a) and the multi- variate THC & BFI (AUC: 0.79, p = 0.04) parameters (Figure 5.6b), provide an early prediction of the therapy outcome; with a potential impact for determining the usage of alternative therapeutic strategies in subjects with high probability to not benefit from the antiangiogenic therapeutic approach. In a different cancer model, the pre-treatment prediction of the therapy outcome based on diffuse optical measurements have been reported in patients with breast cancer undergoing adjuvant chemotherapy [171]; however, different hemodynamic parameters were observed to be predictive at the baseline time point; suggesting that these results could be disease dependent and/or therapeutic agent specific.

Regarding the *in vivo* longitudinal tissue hemodynamics monitoring, the estimated tumor hemodynamics (THC, SO_2 and BFI) from the therapy - treated and control - groups (Figure 5.7) were observed to be statistically significant different ($p < 0.01$) during the time course, whereas in the shoulder location, no statistically significant differences ($p \geq 0.52$) were recovered in any parameter. These results demonstrate the hypothesized Sunitinib-derived hemodynamic changes monitored by the diffuse optical methods a suitable tool for assessing and linking those changes to the therapeutic effects. Besides, our findings suggest the specificity of targeted antiangiogenic drugs to treat cancer regions while avoiding global vascular side-effects.

On the other hand, when assessing the longitudinal tissue hemodynamics at each of the therapy outcome - responder and non-responder - groups (Figure 5.8), the estimated tumor oxygen saturation (sO_2) was observed to provide the feasibility to statistically discriminate (p = 0.04) between the responder and non-responder groups (Figure 5.8c) over the time course from day fourteen onwards; suggesting the elevated MVD in the non-responder group as a mechanism to deploy nutrients to the tumor to continue growing even under antiangiogenic treatment.

In this regard, although the tumor total hemoglobin concentration (THC) did not provide any statistical differentiation ($p = 0.46$) among therapy outcomes over time, a decaying trend in both therapy outcome groups (responder and non-responder) was observed (Figure 5.8a), reaching a plateau region comprising from day seven of treatment onwards in both groups. This finding is in agreement with the time point reported by Zhou et. al. [172] in a pre-clinical mouse SF188V+ human glioma xenograft model treated with Sunitinib under the same dosage as the here reported work. This effect might be associated with the vascular trimming of the permeable neovasculature [145, 173] caused by the blockage of the VEGF signaling pathway. Interestingly, the tumor THC levels from the responder and non-responder groups at the plateau region, matches statistically the shoulder THC values (Figure 5.8b) in their corresponding group (responder: $p \geq 0.33$ and non-responder: $p \geq 0.48$). These results might suggest that even though the blood volume level in the tumor is comparable to that of a healthy tissue due to the vascular trimming induced by the VEGF blockage, other signaling pathways could potentially be interfering in the tumor development.

Besides these findings, the early THC change (Figure 5.9b) observed at day three with respect to day zero, the pre-treatment value, (Δ = Day 3 - Day 0) was demonstrated to correlate (R^2: 0.15, $p = 0.023$) with the extracted tumor weight (TW). These results are in agreement with the reported fractional blood volume changes associated with the therapy prognosis reported by Robinson et. al. [21] in a mouse model of 786-0 ccRCC cells, and might be indicative of the capability of a resistant tumor to adapt and continue developing even under nutrient-depleted conditions [7].

Along the same lines, the early change (Day 3) in the retrieved tumor BFI parameter with respect to the pre-treatment value (Figure 5.9a) was observed to correlate (R^2: 0.17, $p = 0.017$) with the final micro vascular density (MVD). These results are in agreement with reported findings by Huang et. al [169] in a xenograft mouse model of 786-0

ccRCC cells; where an increase in the micro vessel density in the tumor was found in Sunitinib-resistant specimens.

In general, these our findings suggest an induced trigger effect by the Sunitinib antiangiogenic therapy on the early days of treatment, being the pre-treatment THC and BFI tumor hemodynamic parameters a potential set of predictive biomarkers of the therapy outcome. However, the early changes and longitudinal monitoring of the THC, SO_2 and BFI parameters provides the feasibility to predict the final therapy effects. Overall, these results can potentially be translated to the clinics, where diffuse optical techniques have been routinely applied in patients with head and neck [174, 175], prostate [176] and breast [177, 178] cancer to evaluate their response to several therapeutic platforms.

5.4 CONCLUSION

Diffuse optical techniques have been demonstrated to be a suitable tool-box for predicting the therapeutic resistance of a tumor to antiangiogenic therapy from the pre-treatment time point. Furthermore, the longitudinal tissue hemodynamics monitoring provides not only the possibility to assess the therapeutic response over time but also to predict the ending point therapy effects from the early changes in the hemodynamic parameters. This set of features bridge the gap of the current translational oncology field by providing relevant biomarkers for predicting the therapy outcome and prognosis; being particularly relevant for the early identification of the intrinsic resistant tumors where alternative therapies might be applied in order to achieve better therapy prognosis.

6

DIFFUSE OPTICS FOR NANOMEDICAL APPLICATIONS: IN VIVO RESULTS

OVERVIEW

Inorganic nanoparticles are emerging to be promising agents for early diagnosis and less-invasive therapies due to their chemical and physical properties. Yet, their translation to the clinic has, in part, been hindered by the lack of tools to non-invasively quantify their *in vivo* concentrations at the tissues of interest. In this work, we demonstrate that diffuse optical techniques employing near-infrared light have the potential to address these needs in the specific case of gold nanoparticles due to their optical absorption properties.

As in the previous sections, an orthoxenograft mouse model of clear cell renal cell carcinoma was non-invasively assessed by near-infrared diffuse reflectance and correlation spectroscopies before and over several days following intravenous injection of polyethylene glycol-coated gold nanorods (AuNRs-PEG). This platform enables one to follow the kinetics of the AuNRs-PEG uptake by the tumor, in good quantitative agreement with *ex vivo* inductively coupled plasma mass spectroscopy. Furthermore, it allows for the simultaneous monitoring of local tissue hemodynamics and I conclude that AuNRs do not significantly alter the animal physiology. I note that the penetration depth of this current probe was few millimeters but can readily be extended to over a centimeter. This study and the methodology complements the nanomedicine toolbox providing a flexible platform, extendable to other absorbing agents and potentially translatable to human trials.

THE RELEVANCE OF GOLD NANOPARTICLES:

Over the last decades, gold nanoparticles [179, 180] have emerged as promising agents for several medical and biological applications [181–186] due to their chemical and optical properties. They are particularly interesting for applications in oncology [26, 27, 187–190] due to their small size, which allows them to passively accumulate into the tumor through the leaky neovasculature [191–194]. Furthermore, by coating their surface with certain chemistry [195, 196], a passive targeting of the tissue can be achieved by improving their biocompatibility; providing longer circulation periods in the bloodstream to allow their extravasation into the tumor. Moreover, the further functionalization of their surface with particular receptors [197–199] converts them into suitable nanovectors for deploying drug payloads [200–203] at an specific targeted location while reducing the toxicity and side-effects of the therapeutic drug. Also, one of the most relevant features of the gold nanoparticles relies on the enhanced light absorption capability at their localized surface plasmon resonance (LSPR) peak [29–32, 204, 205]. These features suggest them as efficient contrast agents for imaging tissue structures by a manifold of optical methods [206–212] but also as efficient light-to-heat converters, hence being suitable therapeutic vehicles for plasmon-based photo-thermal therapy (PPTT) [33, 34, 213]. Furthermore, their LSPR can be tuned by modifying their size and shape. In this regard, several geometries and configurations have been explored [214, 215], where the gold nanorods emerge as the most efficient morphology for PPTT applications [216].

"Theranostics", which I will use as the dual capability of a single agent (method, drug, strategy or a combination of all) for diagnostic and therapeutic applications, is an important keyword for this work [217, 218]. A theranostic approach is relevant for the usage of gold nanorods to provide early diagnosis and less-invasive therapies by improving the current cancer therapeutic approaches [28, 217]. However, the clinical translation of theranostic approaches that mainly use inva-

sive methods and/or those using distruptive agents, is often hindered by the dissimilarity of the biomarkers that are utilized. This, when coupled by the specific problems of the nanorods due to unexplored toxicity, side-effects and biological interactions of a metallic nanoagent with a biological medium (e.g. tissue) that raise concerns about their potential drawbacks [219–221]. These gaps call for the development of non-invasive and longitudinal methods for personalized dosimetry (i.e. the quantification of nanoparticles delivered to a particular location) and tumor physiology monitoring during gold nanoparticle-treatment using methodologies that are translatable to human use.

In this framework, diffuse optical techniques [41, 42] rise as a set of suitable techniques capable of bridging those gaps by providing non-invasive, quantitative and longitudinal information about the gold nanorods concentration and the tissue hemodynamics, simultaneously. In this chapter, the biodistribution of polyethylene glycol-coated gold nanorods (AuNRs-PEG) and their interaction with the tissue physiology is explored aiming to bridge the above referred gaps of the nanobiophotonics field.

6.1 METHODS AND PROTOCOLS

A general overview of our vision for the application of diffuse optical techniques DRS/DCS to nano-medicine is shown in Figure 6.1 . In general, gold nanorods are injected into a pre-clinical xenograft ccRCC mouse model and their concentration and biodistribution, along with the tissue hemodynamics, are non-invasively quantified and longitudinally monitored by DRS/DCS diffuse optical techniques, This feasibility paves the way for the development of personalized theranostic applications of nanophotonics in the biomedical field. The employed procedure was approved by the ethical committee of the Bellvitge Biomedical Research Institute - IDIBELL (CEIC - Comité Ético de Investigaciíon Clínica del Hospital Universitario de Bellvitge) and accepted by the local Catalan government (Generalitat de Catalunya,

Departament de Medi Ambient i Habitatge, Direcció General del Medi Natural, Protocol number: 4899, PI: Oriol Casanovas).

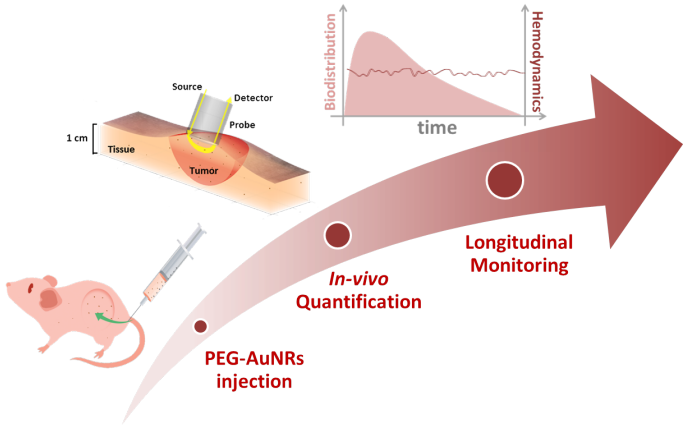

Figure 6.1: Diffuse optical techniques in the nanobiphotonics.. The *in vivo* non-invasive longitudinal quantification of the gold nanorods biodistribution and the tissue hemodynamics by hybrid DRS/DCS optical techniques set the basis for novel nanoparticle-based theranostic applications.

6.1.1 *Gold nanorods synthesis & characterization*

Gold nanorods (AuNRs) in cetyltrimethylammonium bromide (CTAB, Merck KGaA, Germany) were synthesized using a modified seed-based method [222, 223] to control their size and aspect ratio. The AuNRs suspension in CTAB was centrifuged at 14000 rpm for ten minutes at 31°C; then the excess of CTAB was removed, and the AuNRs suspension was concentrated ten times. Afterward, polyethylene glycol (PEG) (PEG, Merck KGaA, Germany) was added to the AuNRs suspension, sonicated during 30 minutes, and kept at 28°C overnight to allow the exchange of CTAB chains and PEG moieties. The PEGylated solution (AuNRs-PEG) was centrifuged to remove unbounded PEG moieties, filtered (25 mm RC syringe filter, 0,2 μm pore size, Corning Inc, NY,

USA) to discard aggregation, washed and diluted with ultra-pure water (Milli-Q) to a final concentration of 21 nM.

The resulting PEGylated gold nanorods (AuNRs-PEG) were characterized (Figure 6.2) by transmission electron microscopy (TEM) [224]. To this end, several representative samples of $\approx$ 100 AuNRs-PEG were imaged and visually analyzed (Figure 6.2a). The synthesized AuNRs-PEG showed a mean size of 40 $\pm$ 6 nm in the longitudinal axis and 11 $\pm$ 1.65 nm in the transversal axis, with an aspect ratio of 3.6 $\pm$ 0.2. Their molecular weight was of 52 MDa. The absorption spectrum of the 1:50 diluted AuNRs-PEG was obtained by UV-Vis spectroscopy (Synergy H1, BioTek Instruments, Inc., USA), resulting into a Localized Surface Plasmon Resonance (LSPR) peak at 790 $\pm$ 10 nm. The absorption coefficient of the AuNRs-PEG adjusted for concentration of the solution is shown in Figure 6.2b.

The synthesis and characterization of the AuNRs-PEG here described was carried out at ICFO facilities by Dr. Vanesa Sanz and Dr. Ignacio de Miguel.

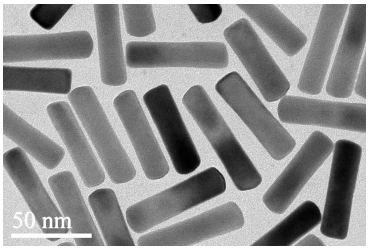

(a) TEM image of the AuNRs-PEG

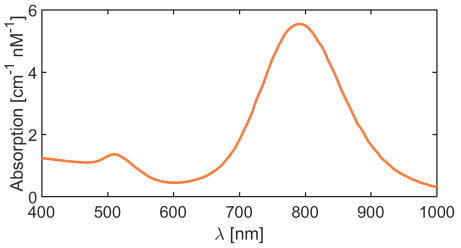

(b) AuNRs-PEG absorption coefficient

Figure 6.2: The AuNRs-PEG characterization. The physical and optical features of the synthesized AuNRs-PEG were assessed by two methods: a) A TEM image of the prepared AuNRs-PEG established a mean longitudinal axis of 40 $\pm$ 6 nm and a transversal axis of 11 $\pm$ 1.65 nm; b) The concentration adjusted absorption coefficient of AuNRs-PEG exhibit a peak absorption coefficient of 5.53 cm^{-1} nM^{-1} at 790 nm with a FWHM of 148 nm and a secondary peak absorption coefficient of 1.37 cm^{-1} nM^{-1} at 510 nm.

6.1.2 *Orthotopic implantation of ccRCC tumors*

A primary host athymic mouse underwent a surgical procedure for exteriorizing the left flank kidney. A total of $\approx 1\times10^6$ clear cell renal cell carcinoma 786O- type cells were injected into the kidney cortex; then the organ was returned to the abdominal cavity. The skin and muscle were sutured using surgical staples, and the tumor was left to grow. Once the tumor reached a volume of $\approx$ 1500 mm^3 - about three weeks after inoculation - the host mouse was sacrificed, and the tumor was excised. The most viable part of the extracted tumor - avoiding the necrotic and hemorrhagic zones - was sectioned into small pieces and frozen at - 80°C.

Afterwards, the mice here employed followed the same surgical procedure for exposing the left kidney. The preserved tumor samples from the host mouse were sutured to the exteriorized kidney; then the organ was returned to the abdominal cavity. The skin and muscles were sutured with surgical staples. Once the wound healed, the staples were removed. The tumors were left to grow to a volume of $\approx$1000 mm^3 - about two weeks after implantation - before starting the measurements. The details about tumor implantation can be found in Ref. [7].

The tumor implantation and growth procedures were carried out at IDIBELL facilities by technician Mar Martínez Lozano.

6.1.3 *Animal population and dosage*

A total of 44 immunodepressed male athymic nude mice (Harlan Laboratories, Spain, weight: 28.2 – 37.6 g, age: 5 weeks) were randomly assigned to either the *study set* or the *validation set*.

The *study set* (N = 20) was employed to longitudinally quantify the AuNR-PEG biodistribution and the tissue hemodynamics simultaneously, providing the possibility to assess their biological interactions. This set of mice was divided into two groups, the *sham* (N = 12) and the

experimental (N = 8) group which received a single tail vein injection of 100 μL of either saline solution (PBS) (0.9% NaCl, B. Braun Co., Germany) or PEGylated gold nanorods (AuNRs-PEG) suspension at 21 nM concentration, respectively. The AuNR-PEG dosage is equivalent to 109 μg of gold (around 4 mg_{gold}/kg_{mouse} or 1.01 mg_{gold}/mL_{blood}) and a total of $\approx 1.27\times10^{12}$ gold nanorods when considering their molecular weight. The animals in the *study set* were measured by DRS/DCS techniques at the baseline (72 hours pre-injection) and at several time points over the following 96 hours post-injection. A detailed explanation of the measurement protocol is given in Section 6.1.4.

The *validation set* (N = 24) was employed for two purposes, 1) To validate the *in vivo* quantified AuNR-PEG concentration by DRS/DCS techniques against the benchmark technology for *ex vivo* quantification of gold in tissue, the ICP-MS technique; and 2) To validate the ICP-MS results with the reported values in the literature. To this end, all the mice in this set received a tail vein injection of 100 μL of AuNRs-PEG at 21 nM concentration; then they were divided into two groups. The first group - named the *DRS/DCS + ICP-MS* group - aiming to validate the first purpose, was composed of mice assessed by DRS/DCS and ICP-MS techniques at 6 hours (N = 7) and 24 hours (N = 11) post-injection. The second group - named the *ICP-MS Only* group - aiming to validate the second purpose, was composed of mice assessed uniquely by ICP-MS technique at 6 hours (N = 6) post-injection.

A summary of the animal distribution in their corresponding groups is shown in Table 6.1.

	Study set		Validation set		
Group	Sham	Experimental	DRS/DCS + ICP-MS		ICP-MS Only
Injection	PBS	AuNR-PEG	AuNR-PEG	AuNR-PEG	AuNR-PEG
Time [h]	96	96	6	24	6
Population [N]	12	8	7	11	6

Table 6.1: Summary of mice groups. The *study set* consist of mice which received 100 μL of either PBS (N = 12) - named *sham* - or AuNRs-PEG (N = 8) - named *experimental* - that were measured at several time point to a maximum of 96 hours post-injection. The *validation set* consist on two groups, the *DRS/DCS + ICP-MS* group composed of mice assessed by DRS/DCS and ICP-MS techniques at 6 hours (N = 7) and 24 hours (N = 11) post-injection and by the *ICP-MS Only* group that was assessed by ICP-MS technique at 6 hours (N = 6) post-injection.

6.1.4 *Measurement protocol*

The hybrid contact DRS/DCS device introduced in Chapter 3 was utilized for collecting the optical data. During the measurement period mice were kept anesthetized with a mixture of isoflurane and oxygen (4% isoflurane and 2 L/min of oxygen for induction and 2% isoflurane and 2 L/min of oxygen for maintaining) and their body temperature remained stabilized at 34°C and monitored by means of a heating blanket with a rectal temperature sensor feedback (PS-03, PhysioSuite, MouseSTAT Pulse Oximeter, Kent Scientific, USA).

The DRS/DCS data was collected from each mouse at two different locations: shoulder and tumor. In the former one, optical data was collected twice from the same position, whereas in the tumor three different positions along the transversal axis - from the abdomen to the back - were probed. The DRS optical data was acquired at six source-detector separations ranging from 0.2 to 0.5 cm over a wavelength range from 600 to 1000 nm. The DCS data was acquired from a set of six source-detector separations ranging within the same detection range as the DRS device. The DRS/DCS data acquisition from the five measured locations (2 in the shoulder + 3 in the tumor) lasted $\approx$ five minutes.

In the *study set*, the aforesaid protocol was applied at nine time points over a period of 8 days as shown in shown in Figure 6.3. Briefly, a 72 hours pre-injection measurement was performed for acquiring the baseline values. Afterwards, the mice were injected with their corresponding agent, either PBS for the *sham* group or AuNR-PEG for the *experimental* group at the doses explained in Section 6.1.3. Then, optical data was collected a few minutes after injection (zero time point), 2.5, 6, 24, 28, 48, 72 and 96 hours post-injection.

In the *validation set*, optical data was collected from the *DRS/DCS + ICP-MS* group at 6 and 24 hrs post-injection following the above described measurement protocol.

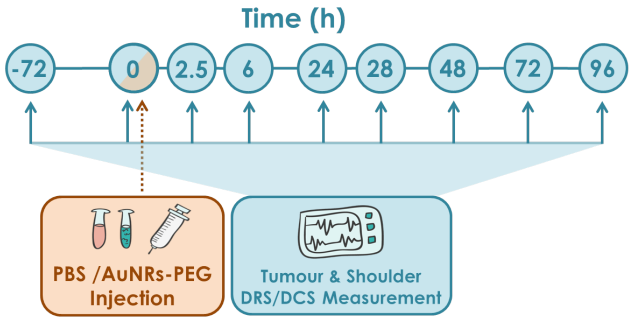

Figure 6.3: The DRS/DCS measurement protocol for resolving the AuNRs-PEG biodistribution. A baseline measurement was acquired 72 hours pre-injection, afterwards, mice were injected with their corresponding agent and measured few minutes after injection, 2.5, 6, 24, 28, 48, 72 and 96 hours post-injection. Optical data was collected twice from the same shoulder position and over three different locations along the transversal axis of the tumor. The average time for collecting data from the five measured locations was of about 7 minutes.

6.1.5 *Collection and preparation of tumor and blood samples for the ex vivo ICP-MS analysis*

The *validation set* of mice, composed of two groups, was employed for collecting tumor and blood samples for the *ex vivo* analysis.

The mice in the first group, called the *DRS/DCS + ICP-MS* group, were measured by DRS/DCS techniques; then a blood sample was extracted, and the mouse was sacrificed for excising the tumor. The collected samples were later analyzed by ICP-MS technique. This procedure was applied at 6 hours (N = 7) and 24 hours (N = 11) post-injection. In this manner both the *in vivo* and *ex vivo* information, at two different time points, was obtained from the same tissue sample. From the mice in the second group, called the *ICP-MS Only* group, blood and tumor samples were extracted at 6 hours (N = 6) post-injection and analyzed by ICP-MS technique.

In general, the total number of *ex vivo* tumor and blood samples collected at 6 and 24 hours post-injection was of N = 13 and N = 11 for each of them, respectively.

The blood samples were collected via cardiac puncture and stored in hematology tubes with ethylenediaminetetraacetic acid (EDTA) for avoiding blood coagulation. For the tumor sample collection, the skin and connective tissue covering it were removed once it was excised. The collected tumors were frozen at - 80°C with no prior chemical treatment and later divided into pieces of $\approx$ 300 mg considering a transversal cut inwards the body - from the outer layer where the skin was placed towards inside the body to account for the AuNR-PEG distribution across the tumor. The *ex vivo* samples collection and preparation was performed at IDIBELL facilities by technician Mar Martínez Lozano.

The prepared blood and tumor samples were processed at the Unitat d'Anàlisi de Metalls - Centres Científics i Tecnològics of the Universitat de Barcelona (CCiTUB) for gold quantification through an inductively coupled plasma mass spectroscopy (ICP-MS) system. This procedure briefly consists of the sample digestion and vaporization using a solution of nitric acid (HNO_3), hydrogen peroxide (H_2O_2) and hydrochloric acid (HCl). Afterward, the vaporized sample is blown through a high-temperature source for ionization (e.i. an argon torch), then the gold quantification in the vaporized sample is performed through a

mass spectrometer (Agilent 7500 CE, Agilent Technologies, Germany). The retrieved gold content in the sample is given in grams of gold per gram of sample with an estimated error of $\pm$ 5%. Further details about the ICP-MS technique can be found in the literature [225].

6.1.6 *Data processing*

In the analysis of the optical data , the water (H_2O) absorption spectrum [50] and the molar absorption coefficients of the oxy- (HbO_2) and deoxy (Hb) hemoglobin (600 - 650 nm [49], 651 - 1000 nm [50, 51]) were employed for retrieving the chromophore concentrations from all the experiments. To this end, numerical fitting was done for the A_0, b and c_i coefficients using a non-linear least square minimization method (LSQNONLIN with Levenberg-Marqardt algorithm, MATLAB, The MathWorks Inc., USA). For a detailed description of the optical data processing method, please see Section 4.1.

In the DCS data processing from any experiment, the β and D_b parameters were numerically fit for retrieving the flow information by using the same non-linear least square minimization method (LSQNONLIN with Levenberg-Marqardt algorithm, MATLAB, The MathWorks Inc., USA) as the DRS data. For a detailed description of the optical data processing method, please see Section 4.2.

6.1.7 *Statistical Analysis*

Statistical analyses were performed using the R statistical software [165]. The estimated DRS/DCS results were expressed as the mean $\pm$ standard error of the mean (SEM) over the assessed location, either the tumor or the shoulder unless indicated. A linear Deming regression [226] was employed for building the regression model for the DRS validation in Section 6.2.1. A two-sample t-test was used in the *ex vivo* tissue characterization analysis in Section 6.2.2. A linear mixed-effect

model (LME) was employed for assessing the *in vivo* biological interactions between and within mice groups in Sections 6.2.2 and 6.2.3. Finally, a paired t-test was employed for the definition of the retention period in Section 6.2.2. The statistically significant differences are indicated by a star (*, $p<0.05$).

6.2 RESULTS

6.2.1 *Validation of the in vivo AuNR-PEG concentration estimated by diffuse optical methods*

A total of 18 tumor samples were collected from the *DRS/DCS + ICP-MS* group at 6 hours (N = 7) and 24 hours (N = 11) post-injection. The mice in this group were first probed for estimating the *in vivo* AuNRs-PEG concentration by DRS/DCS techniques and then sacrificed for excising a tumor sample that was later analyzed for quantifying the *ex vivo* gold content in tissue [$\mu g_{Au}/g_{tissue}$] by the ICP-MS technique [225]. In this manner, the recovered results from both approaches in the same tumor volume can be compared. A linear Deming regression [226] method, which takes into account the differences in variability of the measured observations, was applied for determining the correlation between the measured quantities by both techniques.

A coefficient of determination, $R^2 = 0.82$ with $p < 0.01$, indicates a statistically significant linear correlation between the quantified AuNR-PEG concentration by both techniques from the same tissue volume. This result demonstrates the suitability of the DRS technique to non-invasively retrieve the *in vivo* AuNR-PEG concentration as compared to the goal standard technique. The ICP-MS values have an estimation standard deviation of $\pm$ 5%, whereas the DRS values have a standard error of the mean of $\approx$ 12.8 pM. The intercept of the linear regression at 3.08 pM (95% CI: 0.04 - 5.35), indicates the detection limit of the DRS technique.

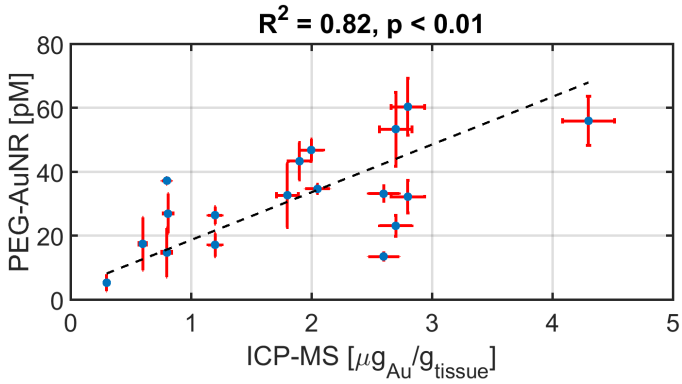

Figure 6.4: Validation of the *in vivo* retrieved AuNRs-PEG concentration. The linear Deming regression of the tumor AuNR-PEG content retrieved by ICP-MS ($\mu g_{Au}/g_{tissue}$) and DRS (pM) techniques demonstrate an agreement between both techniques for explaining the variance of the data. Results are reported as the mean ± std. The DRS data points represents the mean over three different locations measured on the tumor.

6.2.2 *Gold nanorods biodistribution: ex vivo and in vivo measurements*

In Figure 6.5, the *ex vivo* gold tissue content, estimated by the ICP-MS technique at 6 and 24 hours post-injection and expressed as the percentage of injected dose (%ID/g_{tissue}), is shown. In the tumor, no statistically significant difference (p = 0.07) between 6 hours (1.37 ± 0.82 %ID/g_{tissue}) and 24 hours (2.06 ± 0.93 %ID/g_{tissue}) post-injection was observed. On the other hand, a statistically significant decrease (p = 0.02) in the %ID/g_{tissue} circulating in the blood stream at 6 hours (10.83 ± 5.98 %ID/g_{tissue}) with respect to that at 24 hours (5.33 ± 3.50 %ID/g_{tissue}) post-injection was determined.

The *in vivo* longitudinal biodistribution of AuNR-PEG (Figure 6.6) was estimated from the DRS measured signals to resolve both the accumulation - the time length in which the AuNRs-PEG concentration has an increasing trend - and clearance - the time length in which the AuNRs-PEG concentration has a decreasing trend - periods.

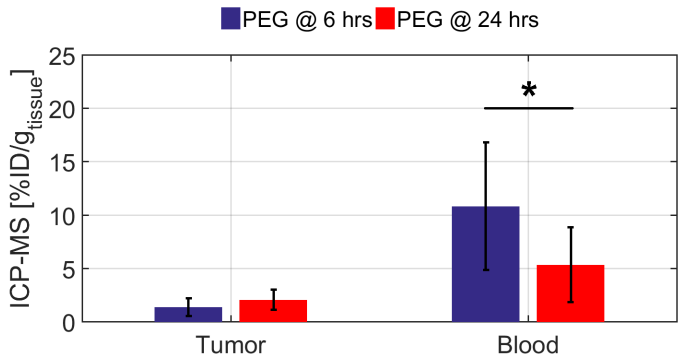

Figure 6.5: The *ex vivo* measurement of the gold nanorod biodistribution. The collected blood and tumor samples were assessed by ICP-MS technique. In the tumor, no statistically significant difference over time was observed. On the other hand, a statistically significant decrease ($p = 0.02$) in the percentage of injected dose circulating in the blood stream was determined. These results suggest that the AuNRs-PEG are cleared from the circulatory system and accumulate in other organs.

During the analysis of the collected data from the *sham* group (N = 12) - mice injected with PBS -, the AuNRs-PEG concentration was maintained as an unknown during the fitting procedure (Section 6.1.6). This approach allow us to quantify the error in the estimated AuNRs-PEG concentration when they are absent in the bloodstream. The mean value of the retrieved AuNRs-PEG concentration [pM] in the tumor was of 1.33 ± 1.99 pM, whereas in the shoulder it was of 1.56 ± 2.40 pM. These values are within the 95% confidence interval obtained during the validation procedure (Section 6.2.1). In the longitudinal analysis based on an LME model, no statistically significant differences were observed in the AuNRs-PEG concentration ($p \geq 0.9$) between and within probed locations. Besides, time was determined not to be a significant factor ($p \geq 0.9$) to the LME model; hence no statistically significant variations over time in AuNRs-PEG concentration can be inferred.

In the *experimental* group (N = 8) - mice injected with AuNRs-PEG solution -, no statistically significant differences ($p = 0.44$) between the

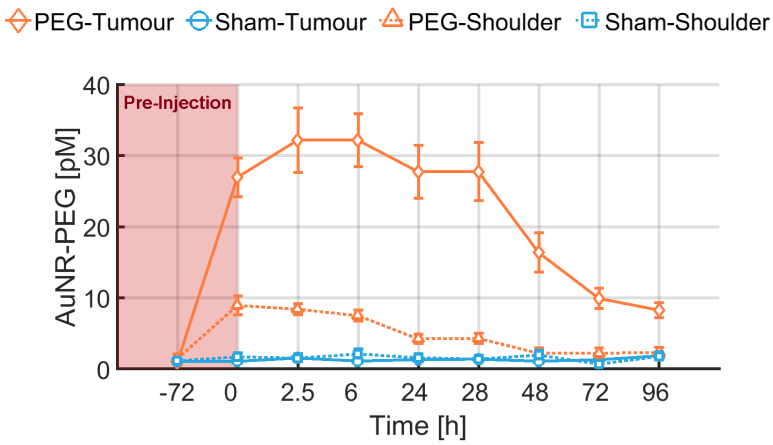

Figure 6.6: The *in vivo* measurement of the longitudinal biodistribution of AuNRs-PEG by DRS technique. The AuNRs-PEG biodistribution, recorded from the *experimental* group of mice and arising from the mean ± SEM of the measured three locations in the tumor and two in the shoulder, shows an accumulation period in both the tumor and shoulder positions, followed by a clearance stage. In the *sham* group, no trends over time were observed at any position. The maximum peak AuNR-PEG concentration in the tumor (32.19 ± 4.51 pM) registered at 2.5 hours post-injection was observed to be statistically significant different ($p < 0.01$) from that in the shoulder (8.96 ± 1.34 pM) registered few minutes post-injection (zero time point).

baseline estimated AuNR-PEG concentrations (72 hours pre-injection) at the tumor (0.89 ± 0.34 pM) and shoulder (1.44 ± 0.62 pM) was observed. The maximum peak concentration at the tumor (32.19 ± 4.51 pM), registered 2.5 hours post-injection, was observed to be statistically significant higher ($p < 0.01$) than that at the shoulder (8.96 ± 1.34 pM) which occurred few minutes post-injection. Therefore, based on those maximum peak values, an accumulation period of 2.5 hours in the tumor and a few minutes in the shoulder can be established. Furthermore, in the tumor position a retention period - the time length with no statistically significant differences in the estimated AuNR-PEG concentration - was observed ($p \geq 0.41$) between time points spanning from few minutes to 28 hours post-injection. In contrast, in the shoulder location, the retention period was not observed. During the follow-

ing time points, a clearance stage was observed at both the tumor and shoulder locations. In the tumor, the last optically assessed time point (96 hours post-injection) corresponded to the lowest estimated AuNR-PEG concentration (8.29 $\pm$ 1.04 pM) and was of about 25% of the maximum peak concentration. In the shoulder, the estimated AuNRs-PEG concentrations from 48 hours post-injection onwards were observed to be statistically similar ($p \geq 0.3$) to the baseline value. These results establish a circulation half-life time of 22 and 12 hours in the tumor and the shoulder, respectively.

6.2.3 *Gold nanorods & tissue hemodynamics: in vivo interactions*

Figure 6.7 summarizes the changes of the tissue hemodynamic parameters before and after AuNR-PEG injection. In the *study* set of mice (N = 20), the microvascular static (e.g. total hemoglobin concentration and oxygen saturation) and dynamic (e.g. blood flow index) tissue hemodynamic parameters along with the AuNR-PEG concentration where quantified from the collected DRS/DCS optical signals of the probed tissue volume. This allowed us to statistically assess the interactions between and within the estimated parameters in the *sham* (N = 12) - blue line - and *experimental* (N = 8) - orange line - groups at the shoulder - dashed line - and tumor - solid line - positions, through a linear mixed-effects model (LME).

In general, the recorded hemodynamics (THC,SO_2 and BFI) in the tumor were observed to be higher than in the shoulder, for both the *sham* or the *experimental* groups.

In Figure 6.7a, the total hemoglobin concentration - THC - in the tumor was observed to be statistically significant higher than that at the shoulder within the *experimental* group ($p^{THC}_{AuNRs-PEG} < 0.01$) with a mean $\pm$ SEM value of 108.02 $\pm$ 6.25 μM and 46.13 $\pm$ 1.07 μM, respectively. The same behavior was observed within the *sham* group ($p^{THC}_{PBS} < 0.01$) were mean $\pm$ SEM values of 108.12 $\pm$ 5.06 μM and 43.12

$\pm$ 0.91 μM were recorded at the tumor and the shoulder locations respectively.

In Figure 6.7b, the oxygen saturation - SO_2 - in the tumor was observed to be statistically significant higher than that at the shoulder within the *experimental* group ($p^{SO_2}_{AuNRs-PEG} < 0.01$) with a mean $\pm$ SEM value of 74.78 $\pm$ 1.90 % and 45.06 $\pm$ 1.91 %, respectively. The same behavior was observed within the *sham* group ($p^{SO_2}_{PBS} < 0.01$) were mean $\pm$ SEM values of 77.56 $\pm$ 1.38 % and 42.14 $\pm$ 1.06 % were recorded at the tumor and shoulder respectively.

In Figure 6.7c, the blood flow index - BFI - in the tumor was observed to be statistically significant higher than that in the shoulder within the *experimental* group ($p^{BFI}_{AuNRs-PEG} < 0.01$) with a mean $\pm$ SEM value of 5.29 $\pm$ 0.37 $cm^2\ s^{-1}$ and 2.77 $\pm$ 0.09 $cm^2\ s^{-1}$, respectively. The same behavior was observed within the *sham* group ($p^{BFI}_{PBS} < 0.01$) were mean $\pm$ SEM values of 5.43 $\pm$ 0.47 $cm^2\ s^{-1}$ and 3.11 $\pm$ 0.13 $cm^2\ s^{-1}$ were recorded at the tumor and the shoulder respectively.

For the statistical evaluation of the biological interactions between the estimated tissue hemodynamics and the AuNR-PEG, the measured physiological parameters (THC,SO_2 and BFI) from the *sham* group were utilized as reference hemodynamic values in the absence of AuNRs-PEG circulating in the body.

In this regard, the estimated tumor hemodynamics (THC, SO_2 and BFI) from the *sham* and *experimental* groups were observed to be statistically similar between them (p^{THC}_{Tumor} = 0.96, $p^{SO_2}_{Tumor}$ = 0.59 and p^{BFI}_{Tumor} = 0.83). Besides, the recovered hemodynamics from the shoulder location were also observed to be similar between the *sham* and *experimental* groups ($p^{THC}_{Shoulder}$ = 0.21, $p^{SO_2}_{Shoulder}$ = 0.26 and $p^{BFI}_{Shoulder}$ = 0.22). Furthermore, the random effect accounting for the differences in time was observed to be statistically significant relevant ($p \leq 0.03$) for the LME model in the tumor position, but not for the shoulder ($p \geq 0.1$). This result suggests a trend in the recovered tumor hemodynamics, probably derived from the high tumor growth rate.

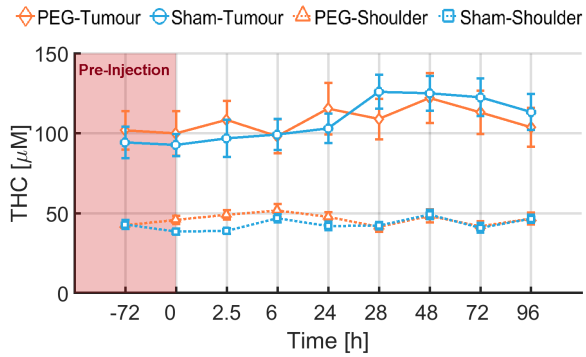

(a) Total Hemoglobin Concentration (THC).

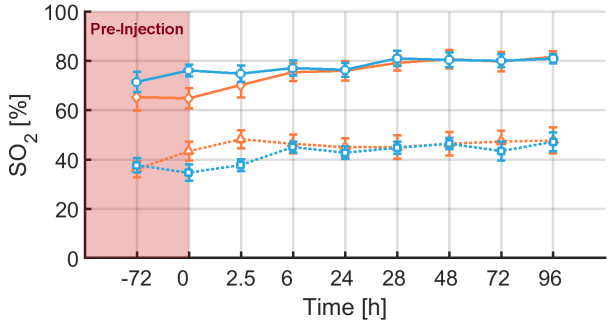

(b) Oxygen Saturation (SO_2).

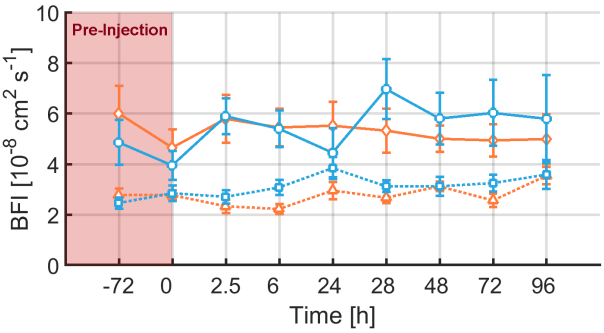

(c) Blood Flow Index (BFI).

Figure 6.7: Longitudinal tissue hemodynamics monitored by DRS/DCS techniques. The estimated tumor hemodynamics (THC, SO_2 and BFI) were statistically significant different ($p < 0.01$) from those of the shoulder (a,b and c), for both group (*sham* or *experimental*). However, no statistically significant differences neither at the tumor ($p \geq 0.59$) nor at the shoulder ($p \geq 0.21$) were observed between the *sham* and *experimental* groups.

6.3 DISCUSSION

Diffuse optical techniques have been demonstrated to be suitable tools for non-invasively quantifying the *in vivo* concentration of AuNRs-PEG, along with the tissue hemodynamics in a longitudinal fashion. This capability allows to further investigate the biological interactions between the tissue hemodynamics and the AuNRs-PEG circulating in the bloodstream; hence being promising for bridging the gap of the nanomedical field to evaluate the toxicity and side-effects of the nanoparticle-based therapies in pre-clinical studies to translate them into the clinics.

To this end, a pre-clinical renal cell carcinoma mouse model was employed to validate the *in vivo* retrieved AuNR-PEG concentration by diffuse optical methods. In this regard, the estimated concentration was observed to be in agreement (R^2 = 0.83, $p < 0.01$) with the *ex vivo* recovered results from the benchmark technology for metal quantification in tissue, the inductively coupled plasma mass spectroscopy (ICP-MS). This validation (Figure 6.4) differs from the previously reported studies [195, 214] by simultaneously quantifying the tissue hemodynamics when estimating the AuNRs-PEG concentrations. These results demonstrate the feasibility of the diffuse optical methods for quantifying the metallic contrast agent concentration in a non-invasive and longitudinal fashion and untangling the tissue microvascular hemodynamics changes.

The estimated gold content by both techniques differ due to the nature of the analyzed samples. The ICP-MS technique analyzes *ex vivo* excised tissue with a consequent loss of blood which might contain a significant fraction of the gold content during their collection. On the other hand, the *in vivo* optical measurements provide a global insight of the gold concentration by retrieving information from the probed tissue volume, accounting for the circulating AuNRs-PEG.

The collected blood and tumor samples at 6 and 24 hours post-injection (Section 6.2.2) and analyzed by the ICP-MS technique, al-

lowed us to resolve the biodistribution of AuNRs-PEG *ex vivo* (Figure 6.5). In this regard, the statistically significant decrease ($p = 0.02$) in the AuNR-PEG circulating in blood suggest their clearance from the bloodstream by the mononuclear phagocytic system (MPS) [192] and their later accumulation in the filtering organs (e.g. liver, spleen and kidney). Moreover, in the tumor, no statistically significant difference ($p = 0.07$) in the AuNRs-PEG content at the evaluated time points was observed, suggesting their accumulation and retention into the tumor tissue through the enhanced permeability and retention (EPR) effect [192, 193]. The *ex vivo* estimated biodistribution was observed to be in agreement with the AuNRs-PEG values reported by Niidome *et.al.* [195] reported in a mouse model.

Along the same lines, the AuNRs-PEG biodistribution resolved *in vivo* by diffuse optical methods (Figure 6.6) demonstrated a higher peak maximum concentration in the tumor (32.19 ± 4.51 pM) with respect to the shoulder (8.96 ± 1.34 pM). Besides, the two positions showed an accumulation period - 2.5 hours and few minutes, respectively - followed by a clearance stage. This kinetic profile of the PEG-coated gold nanorods is in agreement with the reported by Akiyama et.al. [227] in a rectum carcinoma Colon-26 mouse model. In the tumor, no statistically significant differences ($p \geq 0.41$) were observed among the estimated AuNR-PEG concentration ranging from few minutes after injection to 28 hours post-injection; hence denoting a retention period in addition to the accumulation. The retention period might be caused by the permeability of the neovasculature [192], allowing the circulating AuNRs-PEG to internalize into the tumor tissue until being cleared by the MPS system. This finding is of importance for the development of novel nanomedical applications by allowing not only a dosimetry optimization in personalized cancer therapies but also an enhanced thermal therapy outcome by optimizing the light to heat conversion by distributing it over time, providing a manner to develop potential theranostic cancer therapies. On the other hand, in the shoulder which is considered a healthy muscle tissue, the vessel

endothelial junctions were not expected to be permeable, therefore preventing the extravasation of the AuNRs-PEG into the muscle. This behavior can be observed by the recovery ($p \geq 0.41$) of the pre-treatment AuNR-PEG concentration value (1.44 ± 0.62 pM) from the 48 hours post-injection (2.24 ± 0.69 pM) onwards; suggesting that the observed AuNRs-PEG accumulation corresponded mainly to those AuNRs-PEG circulating in the bloodstream and later cleared by the MPS [192]. In addition to the previous findings in the tumor, the prevention of the internalization in the muscle provides the possibility to reduce the toxicity and side-effects associated to the therapeutic drug which may be mostly delivered to the tumor tissue.

Furthermore, the DRS/DCS optical methods were employed to non-invasively quantify the tissue hemodynamic parameters and the AuNR-PEG concentration simultaneously from the same probed tissue volume, allowing us to assess their potential interactions. In this regard, the estimated hemodynamics (THC, SO_2 and BFI) in the tumor were observed to be statistically significant higher ($p^{THC,SO_2,BFI}_{AuNR-PEG,PBS} < 0.01$) with respect to the shoulder in both the *sham* and *experimental* groups. This result is in agreement with the reported values by Menon et. al. [161] in tumor and muscle tissues of a mouse model. Moreover, no statistically significant difference ($p^{THC,SO_2,BFI}_{Tumor,Shoulder} \geq 0.21$) was observed between the recovered hemodynamics from the therapeutic groups in both tumor or shoulder. Therefore, by considering the recovered tissue hemodynamics from the *sham* group as a reference value in the absence of AuNR-PEG in the body, the statistical similarity among treatment groups allow us to conclude, in a quantitative manner, that the presence of AuNRs-PEG in the bloodstream does not alter neither the tumor nor the muscle hemodynamics of the mice. This result provide not only simultaneous monitoring of the nanoagent accumulation in a non-invasive and longitudinal fashion, but also a simultaneous insight into the biological effects it might have for a living organism, paving the way towards a safety translation of the nanoparticle-based therapies into the clinics.

6.4 CONCLUSION

In this study, the diffuse optical methods have been demonstrated to be a suitable tool for non-invasively monitoring the tissue hemodynamic information along with the AuNR-PEG concentration *in vivo* in a longitudinal and quantitative fashion using a pre-clinical ccRCC mouse model. Our methods provide relevant quantitative information about the AuNR-PEG concentration in agreement with the *ex vivo* benchmark technology for quantifying the gold content in tissue, the ICP-MS. Moreover, the *in vivo* recovered biodistribution of the AuNR-PEG in tissue was in agreement with the literature describing its kinetics at several time points; however, our approach differs from the previously reported studies by assessing simultaneously in a non-invasive and longitudinal manner both the tissue hemodynamics and the AuNR-PEG concentration from the same tissue volume. These results demonstrated that the presence of the AuNR-PEG circulating into the blood stream does not significantly alter the tumor nor the shoulder physiology, paving the way towards the development of personalized and *in vivo* monitored theranostic applications of the gold nanoparticles, with potential applications in the oncology field aiming to a future translation into the clinics. Furthermore, the proposed techniques can also be extended to several other platform that employs other organic or inorganic contrast agents with absorbing contrast.

7

NON-CONTACT SCANNING HYBRID DEVICE: *IN VITRO* & *IN VIVO* RESULTS

This Chapter is based on previously published work that I have carried out in collaboration with PhD. Johannes Johansson with data adapted with permission from Ref. [112].

Diffuse optical spectroscopies [41] have demonstrated their feasibility for non-invasively monitoring the tissue hemodynamic changes. Diffuse reflectance spectroscopy (DRS) provides information about the microvascular total hemoglobin concentration (THC), blood oxygen saturation (SO_2) and tissue chromophores concentration (e.g. H_2O and lipids). Diffuse correlation spectroscopy (DCS) [41, 92] monitors the movement of the scattering particles, mainly red blood cells in tissue, by looking at the temporal speckle intensity fluctuations generated by the interference of coherent light diffused through the medium. In tissue, this provides a blood flow index (BFI) which has been shown to be in agreement with other flowmetry techniques [228].

Contact probe-based hyperspectral DRS systems, fit the tissue chromophores concentrations (c_i) and the Mie scattering coefficients (A_0 and b) for retrieving the absorption (μ_a) and reduced scattering ($\mu_s^{'}$) coefficients of the probed medium (see Section 4.1), respectively. This technique has successfully been applied in humans, e.g. for monitoring drug concentration and hemodynamic changes derived from photodynamic therapy (PDT) [107] and for characterizing colon polyps [108]. In addition, it has also been employed in small animal research e.g. for monitoring *in vivo* tumor hemodynamics [105, 229], early assessment of therapeutic outcomes [36, 40, 104] and light dosimetry during PDT [39].

On the other hand, contact DCS systems have been implemented in small animal models, e.g. for monitoring the tissue hemodynamics during brain ischemia and concussion injuries [230, 231], monitoring chemotherapy-derived blood flow changes [160] and during hindleg occlusion and reactive hyperemia studies [232]. Furthermore, hybrid DRS/DCS systems have also been implemented to provide a complete set of hemodynamic and metabolic information from a given sample, where applications in humans [110, 233, 234] and small animals [2, 235] have been demonstrated.

Although useful for clinical and pre-clinical approaches, contact systems suffer from inherent artifacts that hinders their reliability and suitability in specific applications. Some of these artifacts are illustrated in Figure 7.1. To overcome those issues, non-contact approaches of diffuse optical techniques have been implemented. The first hybrid non-contact DCS and frequency-domain device was demonstrated in small animal experiments for monitoring the tissue hemodynamics [236, 237] and for tomographic approaches by the same group [238, 239]. The hybrid non-contact DRS and DCS (ncDRS/ncDCS) approaches have also been utilized for the monitoring of photo-dynamic therapy [40] in small animals. Following these lines, other non-contact DCS implementations have been validated on tissue-like liquid phantoms and humans during arterial cuff occlusion experiments [240]. Further applications have been demonstrated in small animal research [38, 241, 242].

Similarly, non-contact hyperspectral DRS (ncDRS) systems have also been developed and implemented for retrieving *in vivo* tissue hemodynamic information in human studies, e.g. oral imaging endoscope [243], monitoring wound healing [244] and quantification of tissue perfusion [245]. Pre-clinical animal work were also carried out [246–248].

In this chapter,I introduce a hybrid ncDRS/ncDCS device and validated on a set of tissue-mimicking liquid phantoms and *in vivo* by a dynamic study of a human fingertip hemodynamic changes during an arterial arm cuff occlusion test. Finally, the hybridized system was

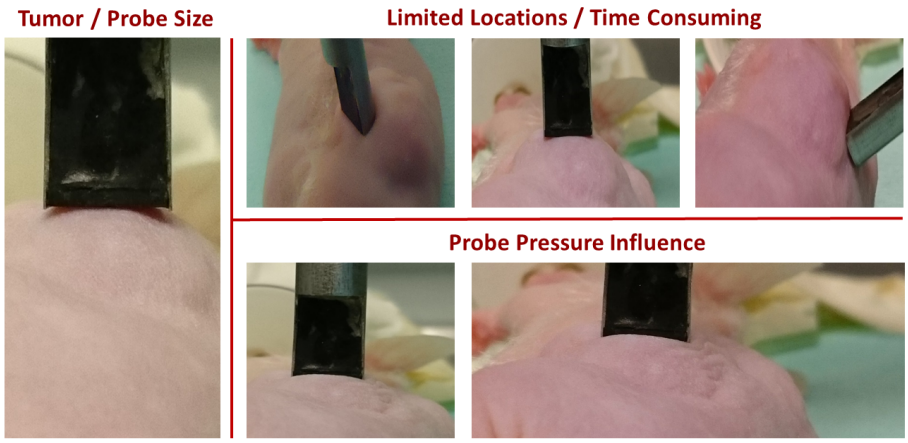

Figure 7.1: Limitations and artifacts derived from contact probe measurements. The lack of uniform contact between the probe and the probed tissue derives into a set of *coupling coefficients* associated to that misplacement in addition to poor signal quality. Furthermore, the manual placement of the probe on several positions over the tumor along with the fiber bending created during the probe placement limits the amount information that can be collected. On top of that, the pressure employed during the probe placement might cause the displacement of blood and blockage of vessels of the region, deriving into a misleading tissue hemodynamics quantification.

demonstrated to recover the tissue hemodynamic information in agreement with the contact version of the same device (Chapter 3), to this end, a group of xenograft athymic mice with ccRCC implanted tumors were assessed by both the contact and non-contact hybrid systems.

7.1 INSTRUMENTATION

A general overview of the developed non-contact scanning hyperspectral hybrid ncDRS/ncDCS device is shown in Figure 7.2. The system employs a shared source fiber and an optical path for delivering broadband or laser light to the tissue surface in a tandem fashion. The back-scattered light is collected through a shared light collection optical path for assessing the optical properties of the probed media.

A detailed description of the system is presented in the following sections.

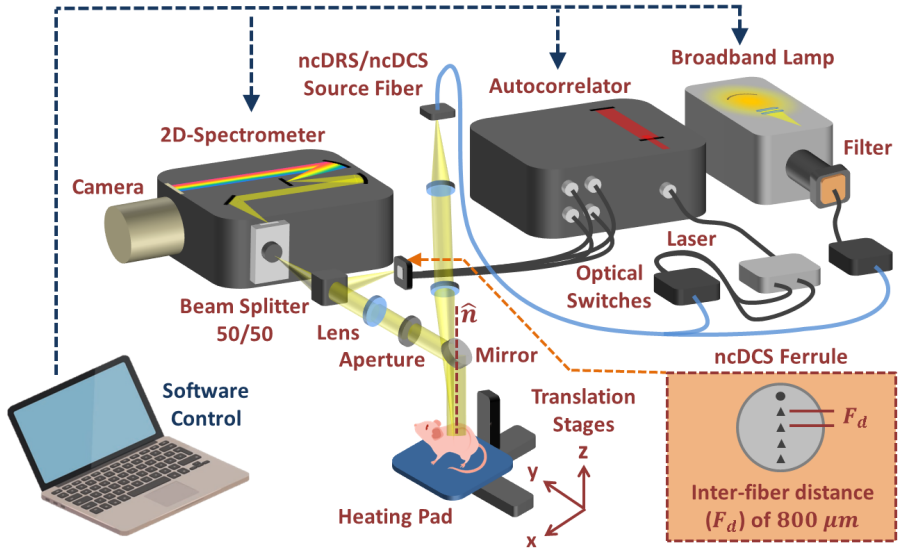

Figure 7.2: Hybridization of the ncDRS/ncDCS optical techniques. The source light of both techniques is delivered at a given position into the tissue surface and collected in a multi-distance scheme. The retrieved light is processed by the corresponding device (either the two-dimensional spectrometer for ncDRS technique or the autocorrelator board for the ncDCS technique) for recording the optical data. The post-processing of the optical data is performed for obtaining the tissue optical properties, directly related to the tissue hemodynamic information.

7.1.1 *Non-contact diffuse reflectance spectroscopy system*

The ncDRS system is same one that was described in the previous Chapters but the detection path is altered by exposing the spectrophotometer slit to the optical path described below and changing the illumination.

For illumination, the fiber output is then used for delivering white light to the tissue when ncDRS data is acquired. The light is focused to an $\approx$ 0.5 mm diameter spot on the target surface via a pair of near-infrared achromatic doublet lenses with anti-reflectance coating (AC254-100-B - f = 100.0 mm, Ø1" Achromatic Doublet, Thorlabs GmbH, Germany), incising with an oblique angle ($\approx$ - 10°) with respect to the surface normal ($\hat{n}$) to avoid specular reflections.

The back-reflected light is then collected through a 45° angle mounted (H45, Thorlabs GmbH, Germany) silver mirror (PF10-03-P01, Thorlabs GmbH, Germany). Afterward, the light passes through an aperture (CP20S, Thorlabs GmbH, Germany) prior reaching a focusing achromatic doublet lens (AC254-100-B - f = 100.0 mm, Ø1" Achromatic Doublet, Thorlabs GmbH, Germany) for avoiding aberrations produced when hitting the lens edges. Later, the light is split into two branches, each of them corresponding to either the ncDRS or ncDCS techniques, using cage (CM1-4ER/M, Thorlabs GmnH, Germany) mounted 50/50 non-polarizing beamsplitter cube (10BC17MB.2, Oriel Instruments, Newport Corporation, USA).

The ncDRS branch light is focused to the pupil of the entrance slit ($\approx$ 100 μM) of a two-dimensional spectrometer (Acton InSight-EFP, Princeton Instruments, USA) while avoiding saturation or blooming. Once inside the spectrometer, the light is decomposed into its wavelength components using 150 $^{grooves}/_{mm}$ diffraction grating, achieving a 5 nm spectral resolution, and imaged by the same detection system shown previously. The maximum optical resolution of the ncDRS system, determined from the 60% contrast in a resolution target (R3L3S6P, Thorlabs GmbH, Germany), is of 9.6 $^{linepairs}/_{mm}$ corresponding to a linewidth of 52 μm. The collected light encompasses a wavelength range (λ) from 550 to 1050 nm. The total number of source-detector pairs available in the ncDRS device can be dynamically adapted by adjusting the system spatial resolution (s_r) [cm/pixel] and the pixel location of the incident light. In general, the collected light is arranged to incise around pixel index # 50; therefore a total of 350 detectors per

wavelength, corresponding to independent pixels of the CCD, can be obtained.

7.1.2 *Non-contact diffuse correlation spectroscopy system*

The ncDCS device uses the same backbone device described in the previous chapters. In the same manner as the ncDRS module, the back-scattered light is collected utilizing the same optical path described previously (Section 7.1.1).

7.1.3 *Scanning module*

A set of three software controlled translation stages (MTS50/M-Z8E, Throlabs GmbH, Germany) with 50 mm travel distance were mounted in an orthogonal geometry for three-dimensional (x,y,z) scanning. When the system was employed for acquiring data from mice (in a pointwise or scanning scheme), a heating pad with a rectal temperature sensor feedback (PS-03, PhysioSuite, MouseSTAT Pulse Oximeter, Kent Scientific, USA) was placed on the translation stages and used for controlling the mouse temperature during the experiment. A metallic frame was mounted for studying other sample types such as tissue-mimicking liquid phantoms. In both scenarios, the sample translation is performed when no data is being acquired, and hence, no light is incising on it. The setup allows a minimum scanning resolution of $\approx$ 1 μm whereas the translation speed can be adjusted by software. For our purposes, a scanning resolution $\geq$ 2 mm and translation speed of 2 mm s^{-1} were commonly employed.

7.1.4 *Data collection*

The ncDRS and ncDCS data acquisition is software controlled and performed in a tandem fashion. The controlling software synchronizes

the switching of the proper light source depending on the data type to be acquired (ncDRS or ncDCS). By activating the corresponding optical switches, the light is delivered to the tissue through the shared source fiber and light delivery optical path during specific exposure time (T). A schematic describing the timing for the data acquisition of both techniques is shown in Figure 7.3.

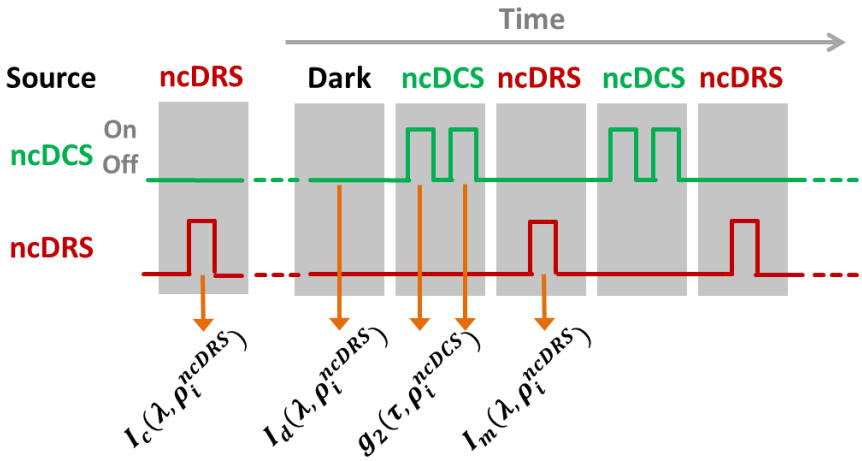

Figure 7.3: The hybrid ncDRS/ncDCS data acquisition timeline. Prior to the data acquisition, a calibration image for the ncDRS device ($I_c(\lambda, \rho_i^{ncDRS})$) utilizing the white light source and consisting on an even illumination of a 99% diffuse reflectance standard is acquired. During the optical data acquisition, the dark intensity $I_d(\lambda, \rho_i^{ncDRS})$ is acquired with the camera shutter closed, then two repeated ncDCS measurements ($g_2(\tau, \rho_i^{ncDCS})$) from the same location are acquired. Afterward, the ncDRS optical data ($I_m(\lambda, \rho_i^{ncDRS})$) is acquired. When performing pointwise measurements (at a static position), this procedure is repeated for acquiring one calibration image, one dark image and the desired amount of ncDRS/ncDRS files. The same procedure applies during the data collection through a scanning approach; deferring in that the sample is first translated to the next sampling location before data collection.

Further details of the instrumentation and analysis methods are described in Ref. [112] and are included as an annex to this Chapter.

7.2 METHODS AND PROTOCOLS

This study consists of a set of three different experiments, which are described in details in the following sections.

7.2.1 *Tissue-mimicking liquid phantoms protocol: in vitro validation*

The scanning approach of the hybrid ncDRS/ncDCS device was validated *in vitro* on a set of five tissue-mimicking liquid phantoms. The phantoms were mixed with varying amounts of scattering emulsion (Lipofundin 20%, B. Braun Melsungen AG, Germany), Milli-Q water and blue ink (Brillian Blue FCF food colouring E133 Vahiné Azul, Vahiné Corp., France). Due to the high light absorption of the utilized blue ink, it was diluted to the 0.1% (1:1000) in Milli-Q water before characterizing its absorption spectrum with a UV-Vis absorption spectrometer (Synergy H1, BioTek Instruments Inc., USA). Three levels of scattering emulsion, Milli-Q water, and 0.1% diluted blue ink were utilized for setting the optical properties - reduced scattering (μ_s') and absorption (μ_a) coefficients - of the mixed liquid phantoms. In this regard, it has been demonstrated that the absorption coefficient can be tuned independently from the reduced scattering coefficient by varying the amount of absorbers in the mixture [249].

A set of five different tissue-mimicking liquid phantoms were mixed according to Table 7.1.

In the utilized scattering emulsion (Lipofundin 20%, B. Braun Melsungen AG, Germany), the 20% of the solution is composed by scatterers - named as the solid part - whereas the rest corresponds mainly to water; the same statement holds for the 0.1% diluted Blue Ink which. This water amount adds to the previously calculated water percentage in Table 7.1. Therefore the total percentage of water content is expected to be of $\approx$ 99% in each liquid phantom. On the other hand, since the unique external absorber in the mixture - beyond the Mili-Q water - is the 0.1% Blue Ink, the recovered concentration percentage of

Phantom #	Lipofundin 20% [%]	Milli-Q water [%]	0.1% Blue Ink [%]
1	2.5	92.5	5
2	2.5	82.5	15
3	5	85.0	10
4	7.5	87.5	5
5	7.5	77.5	15

Table 7.1: The validation tissue-mimicking liquid phantoms. A set of five liquid phantoms were mixed with different amounts of Lipofundin 20% as scattering agent and Milli-Q water and blue ink as absorbers. By varying the amount of each element the optical properties ($\mu_s^{'}$ and μ_a) at different wavelengths can be tuned.

the 0.1% Blue Ink and the reduced scattering coefficient at 785 nm are employed as the expected values for validation.

The expected chromophores (Milli-Q water and blue ink) concentration percentage and the expected reduced scattering coefficent ($\mu_s^{'}$) from each of the mixed tissue-mmimicking liquid phantoms are given in Table 7.2:

Phantom #	Mili-Q water [%]	0.1% Blue Ink [%]	$\mu_s^{'}$ [cm^{-1}] @785 nm
1	$\approx$ 99	5 $\pm$ 0.05	4.15 $\pm$ 0.07
2	$\approx$ 99	15 $\pm$ 0.15	4.15 $\pm$ 0.07
3	$\approx$ 99	10 $\pm$ 0.10	8.30 $\pm$ 0.14
4	$\approx$ 99	5 $\pm$ 0.05	12.45 $\pm$ 0.21
5	$\approx$ 99	15 $\pm$ 0.15	12.45 $\pm$ 0.21

Table 7.2: The expected values of the tissue-mimicking liquid phantoms. The variation in the concentration percentage of the scattering emulsion in each liquid phantom, allows us to vary the reduced scattering coefficient ($\mu_s^{'}$). In addition, the variation in the concentration percentage of the absorbing chromophores (Milli-Q water and Blue Ink) allows us to tune the expected absorption coefficient (μ_a). The liquid phantom ingredients are mainly composed by water, hence the expected water percentage is of about the 99% in all of them.

In the reduced scattering coefficient ($\mu_s^{'}$), the estimated errors were calculated according to the methods reported by Cortese *et.al.* [250]; whereas for the 0.1% Blue Ink, an error of about 1% of the expected value was considered due to pipetting variations.

A region of interest (ROI) of 1×1 cm^2 in steps of 2 mm for a total of 6×6 assessed points, was scanned on each of the mixed liquid phantoms for estimating the optical properties (Figure 7.4). For the ncDRS optical data analysis, a total of twelve source-detector separations (ρ^{ncDRS}) ranging from 0.2 to 0.5 cm were employed over a wavelength range from 550 to 1000 nm. In parallel, the ncDCS device utilized a total of four source-detector separations (ρ^{ncDCS}) within the same range. The timing for acquiring both ncDRS and ncDCS optical data from each tissue-mimicking liquid phantom was of about 3 minutes.

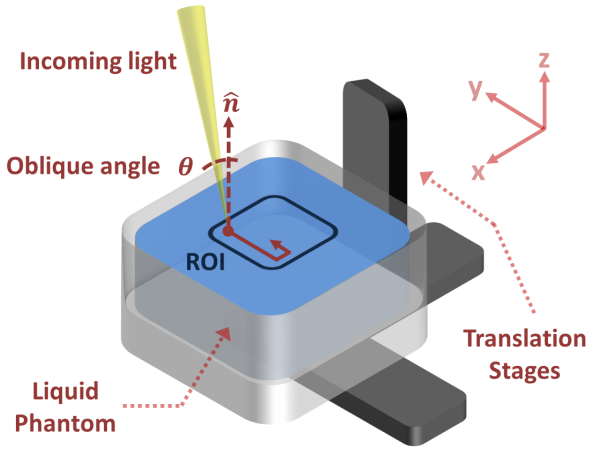

Figure 7.4: The tissue-mimicking liquid phantoms scanning protocol. Each of the mixed liquid phantoms was scanned using the ncDRS/ncDCS device for acquiring optical data. The container with the liquid phantom was mounted on a x,y,z translation stages module to displace the measured location over a region of interest (ROI) of 1×1 cm^2 in steps of 2 mm for a total of 6×6 assessed points.

7.2.2 *Arterial cuff occlusion protocol: in vivo validation*

The pointwise (static location) approach of the hybrid ncDRS/ncDCS device was validated *in vivo* by acquiring optical data from the blood-rich palmar side of the index fingertip during an arterial arm cuff occlusion in an adult. The procedure was approved by the ethical committee of the Bellvitge Biomedical Research Institute - IDIBELL (CEIC - Comité Ético de Investigaciíon Clínica del Hospital Universitario de Bellvitge) and the subject signed an informed consent before the procedure.

The measurement protocol (Figure 7.5) consisted of the ncDRS/ncDCS optical data acquisition during two minutes as a baseline value. Afterward, the arteries of the arm arteries were occluded through an inflatable cuff at 180 mmHg during three minutes. Finally, the cuff pressure was released and measurements proceeded during three more minutes as a recovery period. For the ncDRS data processing, a total of twelve source-detector separations (ρ^{ncDRS}) ranging from 0.2 to 0.5 cm were employed and data was collected from a wavelength range from 600 to 1000 nm. On the other hand, a total of four source-detector separations (ρ^{ncDCS}) were employed from collecting ncDCS signals; however, due to motion artifacts of the probe sample, the source-detector separations were observed to range within 0.17 to 0.63 cm.

7.2.3 *Tissue hemodynamics assessment protocol by contact and non-contact diffuse optical techniques: in vivo results*

A set of seven male athymic nude mice (Harlan Laboratories, Spain, weight: 26.7 - 33.5 g, age: 5 weeks) with xenograft clear cell renal cell carcinoma (ccRCC) implanted tumors were employed for contrasting the retrieved results of the contact and non-contact hybrid diffuse optical systems. The procedure was approved by the ethical committee of the Bellvitge Biomedical Research Institute - IDIBELL (CEIC - Comité Ético de Investigaciíon Clínica del Hospital Universitario

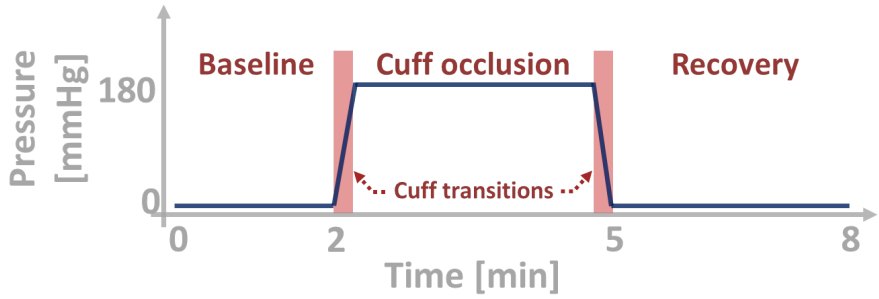

Figure 7.5: Arterial cuff occlusion protocol. A pointwise (static position) acquisition of nc-DRS/ncDCS optical data was performed. The baseline values were acquired during 2 minutes, afterward the arm arteries by occluded by an inflatable cuff with a pressure of 180 mmHg during 3 minutes. Finally, the pressure was released and the recovery period was followed by 3 minutes.

de Bellvitge) and accepted by the local Catalan government (Generalitat de Catalunya, Departament de Medi Ambient i Habitatge, Direcció General del Medi Natural, Protocol number: 4899, PI: Oriol Casanovas).

A summary with a detailed description of both the contact and non-contact hybrid systems is given in Table 7.3.

7.2.3.1 *Orthotopic implantation of ccRCC tumors*

A primary host athymic mouse underwent a surgical procedure for exteriorizing the left flank kidney. A total of $\approx 1\times10^6$ clear cell renal cell carcinoma 786O- type cells were injected into the kidney cortex; then the organ was returned to the abdominal cavity. The skin and muscle were sutured using surgical staples, and the tumor was left to grow. Once the tumor reached a volume of $\approx$ 1500 mm^3 - about three weeks after inoculation - the host mouse was sacrificed, and the tumor was excised. The most viable part of the extracted tumor - avoiding the necrotic and hemorrhagic zones - was sectioned into pieces of $\approx$ $2\times2\times2$ mm and frozen at - 80°C.

Parameter	Contact	Non-Contact	
	Used	Used	Max. or Min. allowed
DRS systems description			
Independent bandwith [nm]	610 - 900	610 - 900	550 - 1050
Wavelength resolution [nm]	5	5	5
Optical Resolution (OR) [μM]	–	200	74
Source-detector separations [cm]	0.2 - 0.5	0.2 - 0.5	†
Number of source-detector pairs	6	12	†
Dynamic range [dB]	96	96	96
Spot size on the object [cm]	0.02	<0.1	–
Depth of focus [cm]	–	$\pm$ 0.4	$\pm$ 0.4
Field of View (FOV) [cm]	–	$\approx 45\times20$	‡
Scanning resolution [cm]	–	<0.2	0.02
Exposure time per frame [s]	4	2	>0.1
DCS systems description			
Source wavelength [nm]	785	785	785
Source-detector separations [cm]	0.2 - 0.5	$\approx$ 0.1 - 0.7	†
Number of source-detector pairs	6	4	4
Integration time per frame [s]	3	3	>0.1
DRS + DCS data acquisition			
Total time per data acquisition cycle			
Pointwise [s]	8	6	1
Scanning* [s]	20	8	3

Table 7.3: Summary of the contact and non-contact systems for the DRS-DCS measurements. Symbols represents: a) †: Dynamic parameter that depends on the system spatial resolution; b) ‡: Dynamic parameter that depends on the sample size and c) *: Probe replacement for contact system and translation for scanning system, respectively. Data reprinted with permission from Ref. [112], Biomed. Opt. Express.

The set of studied mice (N = 7), followed the same surgical procedure for exposing the left kidney. The preserved tumor samples from the host mouse were sutured to the exteriorized kidney; then the organ was returned to the abdominal cavity. The skin and muscles were sutured with surgical staples. Once the wound healed, the staples

were removed. The tumors were left to grow to a volume of ≈1000 mm^3 - about two weeks after implantation - before starting the measurements. The details about tumor implantation can be found in Ref. [7].

7.2.3.2 *Measurement protocol*

The studied mice (N = 7) were assessed by both the contact DRS/DCS and the ncDRS/DCS devices described in details in Chapter 3 and Section 7.1, respectively. During the optical measurements, the mice were kept anesthetized with a mixture of isoflurane and oxygen (4% isoflurane and 2 $^{L}/_{min}$ of oxygen for induction and 2% isoflurane and 2 $^{L}/_{min}$ of oxygen for maintaining) and their body temperature remained stabilized at 37°C and monitored by means of heating blanket feedback with a rectal temperature sensor feedback (Homeothermic Blanket Systems, Harvard Apparatus, USA).

As a first step, contact DRS/DCS optical data was collected from each mouse in three different locations: 1) Foreleg; 2) Hindleg and 3) Tumor. In the first two locations, a series of five repeated measures were performed on each of them. In the tumor location, the probe was placed over five different positions where the last position corresponds to the probe placed on the top center of the tumor and the rest to the cardinal points with respect to it. The DRS optical data was acquired at six source-detector distances ranging from 0.2 to 0.5 cm over the wavelength range of 610 to 900 nm. The DCS optical data was acquired from a set of six source-detector separations ranging within the same detection range as the ncDRS device. The data acquisition from all locations lasted ≈ 7 minutes per mouse.

After the contact DRS/DCS measurements, the mice were allowed to rest for about three hours to let them recover from the inhaled anesthesia. In the meantime, the non-contact device was set and calibrated following the procedures described in Sections 7.6.2.1 and 7.6.2.2 for the ncDRS and ncDCS systems, respectively.

Thc ncDRS data was acquired from a set of twelve source-detector separations ranging from 0.2 to 0.5 cm over a wavelength range from 610 to 900 nm. Thc ncDCS data was acquired at four detection distances ranging from $\approx$ 0.1 to 0.7 cm due to variations in the height of the sample.

The ncDRS/ncDCS optical data acquisition relies on the scanning of a region of interest (ROI) comprising the foreleg, tumor and hindleg parts on the left flank side of each mouse. The scanned ROI differs among mice due to the animal size; however, areas of about 4.6×2 cm^2 were scanned in steps of 2 mm for a total of 24×11 assessed points in general. The collection of optical data from an area of that size is of about $\approx$ 40 min.

7.2.4 *Data processing*

Data reprinted with permission from Ref. [112],Biomed. Opt. Express. In the data analysis, the measured Blue Ink absorption spectrum, water (H_2O) absorption spectrum [50], and the molar absorption coefficients of the oxy- (HbO_2) and deoxy (Hb) hemoglobin (600 - 650 nm [49], 651 - 1000 nm [50, 51]) were employed for retrieving the chromophore concentrations from the corresponding experiment. To this end, numerical fitting was done for the A_0, b and c_i coefficients using a non-linear least square minimization method (LSQNONLIN with Levenberg-Marqardt algorithm, MATLAB, The MathWorks Inc., USA). The ncDRS data was processed in the same manner as the contact DRS acquired data. For a detailed description of the optical data processing method, please see Section 7.6.3.

In the ncDCS optical data processing, the β and D_b parameters were numerically fit for retrieving the flow information by the same non-linear least square minimization method (LSQNONLIN with Levenberg-Marqardt algorithm, MATLAB, The MathWorks Inc., USA) as the ncDRS data. The ncDCS data was processed in the same manner as the

contact DCS acquired data. For a detailed description of the optical data processing method, please see Section 7.6.4.

7.3 RESULTS

7.3.1 *Tissue-mimicking liquid phantoms*

The results from the scanning ncDRS/ncDCS measurements on the set of five tissue-mimicking liquid phantoms are shown in Figure 7.6. In Figure 7.6a, the estimated absorption coefficients (μ_a) are shown to be in acceptable agreement with the expected values; retrieving average underestimated values of $\approx$ 10% (rangie: 4% to 16%) for the 0.1% Blue Ink in some liquid phantoms. On the other hand, the estimated reduced scattering coefficient (μ_s') is shown to be underestimated for liquid phantoms with large concentration of scatterers.

Regarding the retrieved flow information (Figure 7.6b), the scanned liquid phantoms were expected to have similar flow dynamics since all of them were measured at room temperature and no variations in viscosity are induced during the mixing process. In this context, none of the scanned liquid phantoms show any statistically significant difference with respect to the other, denoting good agreement with the expected behavior. A mean D_b value of 2.7×10^{-8} [$cm^2\ s^{-1}$] and average standard deviation of 0.15×10^{-8} [$cm^2\ s^{-1}$] was recovered from the ncDCS scanning measurements. Overall, the results are comparable in their relationship to the parameters reported by the contact device [1] in previous validation studies.

7.3.2 *Arterial arm cuff-occlusion*

The results from the pointwise ncDRS/ncDCS measurement on the index finger tip during an arterial arm cuff-occlusion test are shown in Figure 7.7. A relatively stable Total Hemoglobin Concentration (THC)

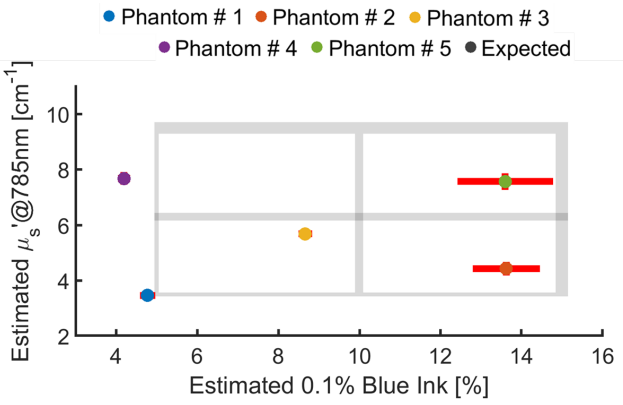

(a) Estimated μ_s' and 0.1% Blue Ink.

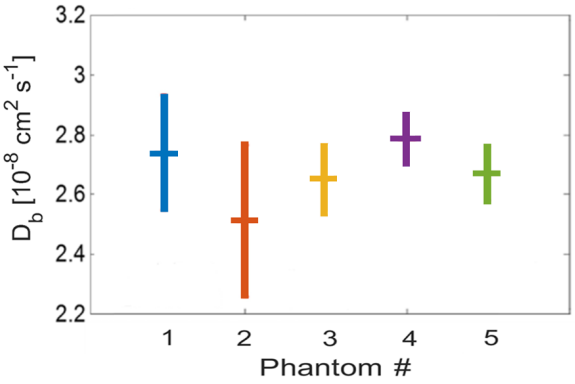

(b) Estimated D_b parameter.

Figure 7.6: Tissue-mimicking liquid phantoms scanning results. The estimated mean values or distributions are denoted by colors associated to the results from a given liquid phantom. The error bars represents the standard deviation over scanned positions. The gray shadowed lines (a) represents the reported expected errors in the targeted values. a) The estimated and expected reduce scattering coefficient (μ_s') at 785 nm and 0.1% Blue Ink from each scanned liquid phantom and b) The estimated flow (D_b) on each scanned liquid phantom. Data adapted with permission from Ref. [112], Biomed. Opt. Express.

was observed during the whole arterial arm cuff-occlusion (Figure 7.7a blue line) with mean values and standard deviations of 79.42 $\pm$ 11.21

[μM] in the baseline, 91.28 $\pm$ 12.63 [μM] during the cuff-occlusion and 78.94 $\pm$ 8.81 [μM] during the recovery period. These results are in agreement with expectations due to the blockage of incoming and outcoming blood from the occluded body part. In parallel, a gradual decay in the Oxygen Saturation (SO_2) was observed due to the oxygen consumption from the accumulated blood in the occluded body part (Figure 7.7a orange line) with a mean values and standard deviation of 75.08 $\pm$ 4.72 [%] and 76.85 $\pm$ 3.86 [%] in the baseline and recovery periods, respectively. During the occlusion period, a drop in the Oxygen Saturation of $\Delta SO_2 \approx 12\%$ was recovered. On the other hand, the Blood Flow Index (BFI) showed a drop during the cuff-occlusion due to the blockage of blood flowing into the probed body part (Figure 7.7b). The estimated BFI during the recovery period showed some sharp peaks, which might be associated with motion artifacts of the subject. In this regard, BFI mean and standard deviation values of 8.76 $\pm$ 4.62 [10^{-8} cm^2 s^{-1}] and 9.06 $\pm$ 5.14 [10^{-8} cm^2 s^{-1}] during the baseline and recovery period were recorded, respectively. In the cuff-occlusion period, a BFI of $\approx$ 0.09 $\pm$ 0.02 [10^{-8} cm^2 s^{-1}] was retrieved. The recovered kinetics of tissue hemodynamics (THC,SO_2 and BFI) are in agreement with the reported parameters in the literature [251–253]

7.3.3 *Tissue hemodynamics assessed in vivo by contact and non-contact diffuse optical techniques*

The recovered tissue hemodynamics from both the DRS/DCS and the ncDRS/ncDCS devices from regions of interest of about 0.5 to 1.5 cm^2 over the tumor, hindleg and foreleg locations of the whole set of experimental mice (N = 7) are shown in Figure 7.8. In general, a good agreement between the retrieved parameters from both measurement approaches was observed. The foreleg and hindleg locations show statistically significant lower hemodynamic values with respect to the tumor location ($p < 0.05$). Such difference can be explained by the heterogeneity and enhanced metabolism proper of a tumor, hence provid-

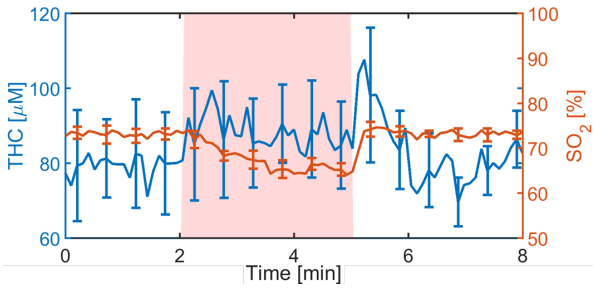

(a) Total Hemoglobin Concentration(THC) and Oxygen Saturation (SO_2).

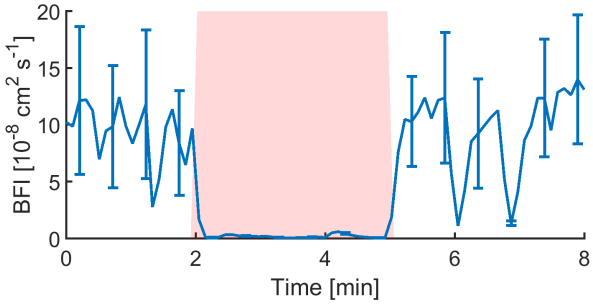

(b) Blood Flow Index (BFI)

Figure 7.7: Arterial arm cuff-occlusion pointwise results. The estimated tissue hemodynamics from the arterial cuff-occlusion test are shown, where the red shadowed zone corresponds to the cuff-occlusion period (3 min): a) The Total Hemoglobin Concentration (THC) is shown to remain relatively stable, whereas the Oxygen Saturation (SO_2) had a gradual decay due to the oxygen extraction from the accumulated blood; b) The Blood Flow Index (BFI) was observed to be diminished during the cuff-occlusion period due to the blockage of incoming blood. Fluctuation in the estimated BFI values might be caused by movement artifacts. Data adapted with permission from Ref. [112], Biomed. Opt. Express.

ing the capability to non-invasively discriminate between healthy and tumor regions. In this regard, the estimated values of the Oxygen Saturation (SO_2) were observed to be particularly elevated, possibly due to the arteriovenous shunts and altered metabolism. Finally, the Blood Flow Index (BFI) in the tumor location was observed to be slightly

lower in the non-contact assessment, albeit not statistically significant difference, when assessed by the contact approach.

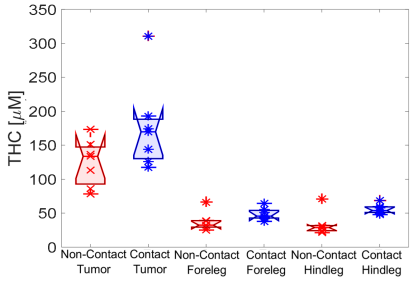

(a) Total Hemoglobin Concentration (THC).

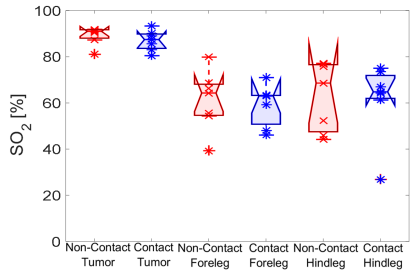

(b) Oxygen Saturation (SO_2).

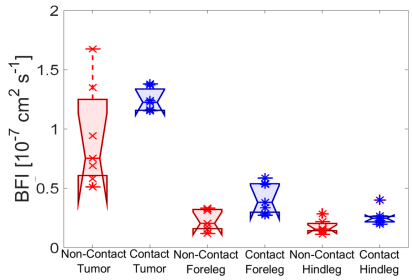

(c) Blood Flow Index (BFI).

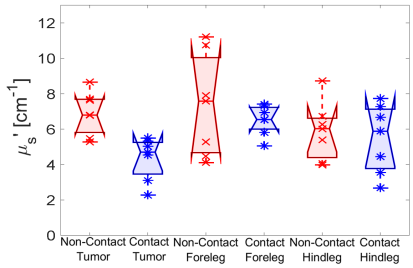

(d) Reduced scattering coefficient (μ_s').

Figure 7.8: The *in vivo* tissue hemodynamics retrieved by the contact and non-contact devices. The estimated tissue hemodynamics from the contact - blue - and non-contact - red - diffuse optical devices over N = 7 mice for a) total hemoglobin concentration (THC), b) oxygen saturation (SO_2), c) blood flow index (BFI) and d) reduced scattering coefficient at 785 nm (μ_s'). Data adapted with permission from Ref. [112], Biomed. Opt. Express.

The summarized results comparing both the contact and non-contact systems are shown in Table 7.4, whereas the statistical results of the inter-system parameters for each measurement method are shown in Table 7.5.

A representative mouse of the recovered topographic map with the overlapped tissue hemodynamic parameters is shown in Figure 7.9.

Population (N = 7)	Contact		Non-Contact		
	Mean	± std between mice	Mean	± std between mice	p-value
Tumor					
BFI [10^{-7} cm^2 s^{-1}]	1.24	0.10	0.93	0.43	0.10
THC [μM]	176	65	125	24	0.054
SO2 [%]	87	4	89	4	0.08
musp @785 nm [cm^{-1}]	4.34	1.21	6.91	1.22	0.004
Hindleg					
BFI [10^{-7} cm^2 s^{-1}]	0.26	0.07	0.17	0.06	0.048
THC [μM]	56	7	33	17	0.01
SO2 [%]	62	16	63	15	0.81
musp @785 nm [cm^{-1}]	5.46	1.94	5.88	1.64	0.61
Foreleg					
BFI [10^{-7} cm^2 s^{-1}]	0.42	0.13	0.23	0.09	0.03
THC [μM]	49	9	37	14	0.12
SO2 [%]	59	9	61	13	0.71
musp @785 nm [cm^{-1}]	6.52	0.84	7.33	2.89	0.52

Table 7.4: Summary of the *in vivo* results retrieved by the contact and non-contact systems. Data adapted with permission from Ref. [112], Biomed. Opt. Express.

	Contact			Non-Contact		
	T - HL	T - FL	HL - FL	T - HL	T - FL	HL - FL
BFI [10^{-7} cm^2 s^{-1}]	<0.01	0.01	0.11	<0.01	<0.01	0.58
THC [μM]	<0.01	<0.01	0.72	<0.01	<0.01	0.29
SO2 [%]	<0.01	<0.01	0.32	<0.01	<0.01	0.44
musp @785 nm [cm^{-1}]	0.33	0.06	0.97	0.53	0.70	0.74

Table 7.5: Summary of the *in vivo* intra-system and inter-position statistic. A two-samples t-test statistical comparison of the retrieved hemodynamic values between measured positions (inter-positions) by a given technology (intra-system). The parameters T, HL and FL refers to the tumor, hindleg and foreleg, respectively.

The blood-rich region corresponding to the tumor location is distinguished from the rest of the scanned healthy areas.

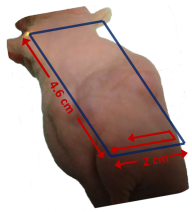

(a) Scanned ROI.

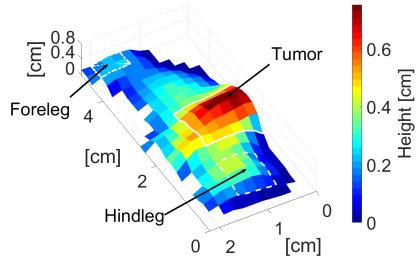

(b) Topographic surface map.

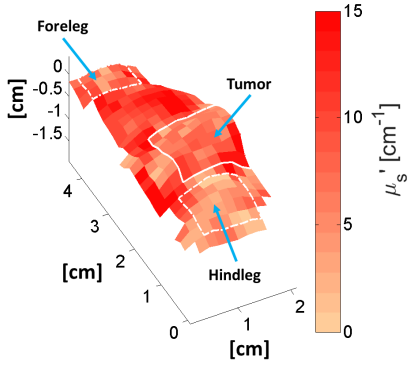

(c) Reduced scattering coefficient (μ_s').

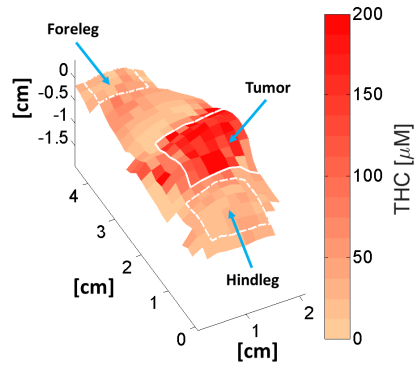

(d) Total Hemoglobin Concentration (THC).

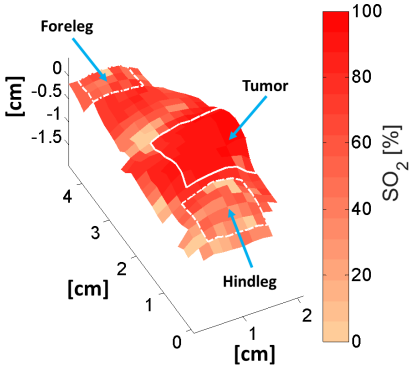

(e) Oxygen Saturation (SO_2).

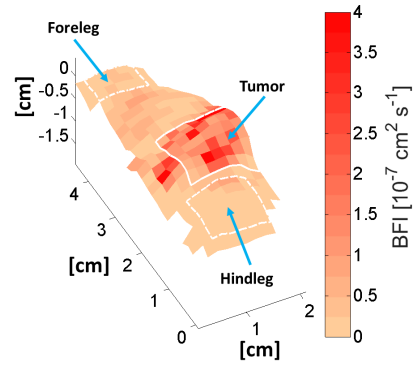

(f) Blood Flow Index (BFI).

Figure 7.9: Illustrative *in vivo* scanning results retrieved by the ncDRS/ncDCS device. The recovered topographic map (b) retrieved from the scanned region of interest (a) is shown to corregister with the tissue hemodynamic parameters estimated by the ncDRS/ncDCS device. The reduced scattering coefficient (c) is shown to be relatively homogeneous over the whole scanned area. The Total Hemoglobin Concentration (d), Oxygen Saturation (e) and Blood Flow Index (f) parameters are shown to be elevated in the tumor area with respect to the healthy regions. Data adapted with permission from Ref. [112], Biomed. Opt. Express.

7.4 DISCUSSION

A non-contact scanning device, combining diffuse correlation spectroscopy and pushbroom hyperspectral diffuse reflectance spectroscopy have been introduced for small animal imaging. The device was validated both *in vitro* by scanning a set of five tissue-mimicking liquid phantoms with different tissue optical properties and *in vivo* by a point-wise measurement on a human fingertip during an arterial arm cuff-occlusion. Furthermore, the non-contact system was demonstrated to retrieved tissue hemodynamic parameters in agreement with the contact version of the device, previously applied in pre-clinical studies in Chapter 5 and 6.

The ncDRS/ncDCS setup was based on a set of translation stages as a scanning module, due to the feasibility to integrate both diffuse optical techniques into a single optical collection path. Besides, by implementing an oblique angle of incidence, specular reflections from the sample can be avoided; hence eliminating the necessity of cross-polarize the back-reflected light [40] for their removal, which might drastically diminish the amount of collected light, hindering the retrieval of deep tissue information. An optional approach that can be further implemented in this device would be the usage of optical elements for scanning the sample. In this regard, traditional scanning approaches employ optical elements for translating the light source along the sample' surface [242, 254, 255], shifting the optical light collection path simultaneously. Such mechanical approaches can be further implemented in the ncDRS/ncDCS setup, although with extra complexity due to the usage of a pushbroom method for acquiring light, which implies the movement of the detection parts (e.g. 2D-spectrometer). However, snapshot imaging technologies have started to rise as a promising method for simplifying the data acquisition. This technology has already been implemented for the study of the human brain [256]. However current snapshot technologies allow for the acquisition of few wavelengths ($\approx$ 25 channels), which represents a

harsh compromise for the implementation of the here developed data processing method (Section 4.1).

On the other hand, a benefit of implementing a pushbroom approach relies on the acquisition optical data from an aligned array of detectors over a large number of wavelengths. Furthermore, the number of detectors can be tuned by the adjustment of the camera field-of-view (FOV), whereas the wavelength range and resolution can be adjusted by the specifications of the diffraction grating and the size of the spectrometer entrance slit, respectively. This feature provides us with a rich data set that might improve the retrieval of quantitative results by providing more information that aims to better constrain the fitting problem. Moreover, this approach paves the way for potential applications in three-dimensional diffuse optical tomography.

The implemented non-contact system demonstrated to recover good quantitative results with respect to the contact version while surpassing the main artifacts related to the probe-based systems (e.g. probe size, time-consuming location and probe pressure influences in the results). However, the non-contact system suffers from another type of artifacts that might mislead the recovered results, especially at long source-detector separations. For instance, the presence of stray light in the recorded images compromise the accurate quantification of chromophore concentrations, especially at the wavelength regions where the CCD detector has poor quantum efficiencies. However, several implementations have been developed to correct for the presence of stray light [257, 258], which can further be implemented during the data post-processing. Another limitation, proper of the non-contact system is the shadowing of some regions while scanning due to the surface curvature, especially in tumor samples; hence presenting difficulties to provide optical data from the whole scanned region. In this regard, the implementation of two-sides illumination can be beneficial, albeit compromising the speed in the data acquisition.

The employment of the recovered topographic map of the sample' surface can be employed to further account for the tissue curvature,

modifying the source-detector separation, during the data processing [259]. Additionally, more advanced photon transport models or Monte Carlo simulations can be implemented by taking advantage of the recovered sample's height map, allowing to generate realistic geometry models [260].

Regarding the recovered results from the set of tissue-mimicking liquid phantoms (Figure 7.6), they were observed to be in good agreement with previously reported contact DRS systems; were estimated errors of $\approx$ 10% were also found [107, 261]. Besides, the retrieved tissue hemodynamic changes from the arm cuff-occlusion test were observed to agree with reported values in the literature [251–253]. The estimated Oxygen Saturation (StO_2) values were shown to be elevated in the fingertip during the baseline and recovery period, although in agreement with the literature [262]. This characteristic might be associated to the presence of arterio-venous anastomoses [263], which assists in regulating the body temperature by shunting superficial blood directly from the arteries to the veins and thus bypassing the oxygen-extracting capillary network. Both results suggest the feasibility of the non-contact device to monitor the optical properties, associated with the tissue physiology, with reasonable accuracy.

Furthermore, the gathered results from the *in vivo* scanning approach on a xenograft ccRCC mouse model (Figure 7.9) were also observed to agree with the reported parameters in the literature. Baran *et.al.* [264] reported $\mu_s^{'}$ values at 780 nm - ours is reported at 785 nm, although values should be comparable - ranging from 5 to 19 [cm^{-1}] over several positions of a freshly excised human kidney tumor, which are in is agreement with our findings. Moreover, Kienle *et.al.* [75] and Xia *et.al.* [265] have characterized muscle tissue (such as the here probed hindleg and foreleg) to have reduced scattering coefficients of around 5 cm^{-1}, in agreement with the ncDRS estimated values. The scanned tumors were observed to have high blood content. The ccRCC tumor type characterizes for relying on reduced mitochondrial activity [266], employing glycolysis as the main metabolic mechanism and

hence, not extracting much oxygen from the blood. This factor can probably explain the high estimated Oxygen Saturation (Figure 7.9) values, which are also in agreement with our results found in another study utilizing the contact DRS/DCS device [2].

7.5 CONCLUSION

In this chapter, we have developed, validate and demonstrate a hybrid ncDRS/ncDCS device to be suitable for *in vitro* and *in vivo* applications. The device has been demonstrated to be a feasible solution for monitoring not only longitudinal hemodynamic changes but also to resolve the spatial distribution of chromophores. This device provides the capability to acquire a significant amount of information that might be beneficial for more robust estimation of the optical properties of the probed sample. Moreover, this feature might be translatable into future tomographic approaches for allowing a three-dimensional reconstruction of the tissue hemodynamics. Finally, the device was demonstrated to provide valuable complementary information for developing novel data processing techniques that would allow to further improve the here reported methods for data acquisition and processing.

7.6 ANNEX: FURTHER DETAILS OF THE ACQUISITION AND ANALYSIS METHODS

7.6.1 *Further details of the data acquisition*

7.6.1.1 *ncDRS data collection*

During the ncDRS data acquisition a set of three images, shown in Figure 7.10, are recorded:

1. The calibration intensity ($I_c(\lambda, \rho_i^{ncDRS})$): An image of the reflected light from an even illumination of a 99% diffuse reflectance standard (SRS-99-010 Spectralon, Labsphere Inc., USA) is acquired. This image allows the correction of the differences in sensitivity among pixels (Fig. 7.10a) and must be taken using the same exposure time as the rest of images (See points 2 and 3). By using a homogeneous illumination, the light counts would be low, and hence the recorded image would have low quality. However, several repetitions of the image can be acquired and averaged to improve the Signal-to-Noise Ratio (SNR).

2. The dark intensity ($I_d(\lambda, \rho_i^{ncDRS})$): Records the intensity counts read by the CCD sensor when isolated from any incoming light by keeping the camera shutter closed (Fig. 7.10b).

3. The main intensity ($I_m(\lambda, \rho_i^{ncDRS})$: A spectral and spatial image of the back-reflected light from the probed sample. Since the maximum light intensity peak is located at a certain pixel position on the CCD surface - commonly around pixel index # 50 -, the rest of the pixels would be utilized as detectors. This characteristic allows the high-density recovery of the exponential decay of light over distance at a manifold of wavelengths (Fig. 7.10c).

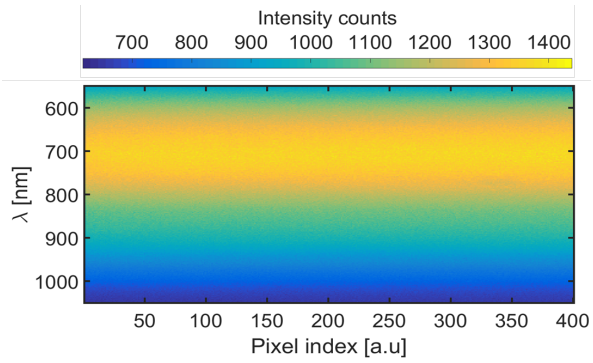

(a) $I_c(\lambda, \rho_i^{ncDRS})$

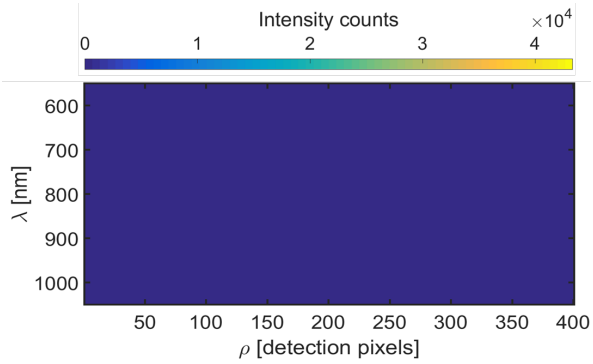

(b) $I_d(\lambda, \rho_i^{ncDRS})$

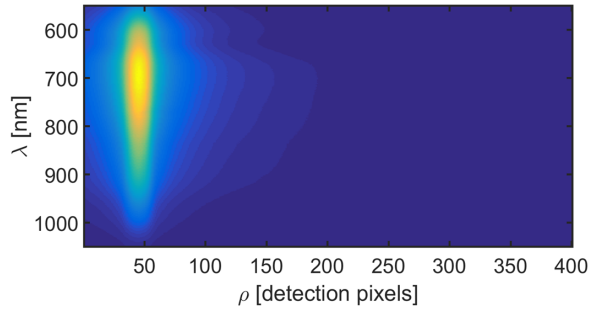

(c) $I_m(\lambda, \rho_i^{ncDRS})$

Figure 7.10: The set of images collected by the ncDRS device. An optical path is employed for delivering light to the tissue. The diffuse reflected light is collected through another optical path and imaged by a CCD camera at a manifold of source-detector distances and wavelengths. a) The calibration light intensity retrieved from an even illumination of a 99% diffuse reflectance standard; b) The light intensity when the the camera shutter is closed and c) The main light intensity when the ncDRS source is occupied to irradiate the tissue.

In the ncDRS data acquisition, the amount of collected images (apart from the calibration intensity image) would depend on the measurement protocol. In general, when performing pointwise measurements (at a static position), the amount of ncDRS images would depend either on the timing (e.g. during cuff occlusion tests) or on the desired signal quality for averaging over several acquired images for improving the Signal-to-Noise ratio (SNR). On the other hand, while collecting data from multiple locations in a scanning fashion; the number of acquired images would be given by the desired spatial discretization. However, repeated measures on a given location can also be acquired before translating the sample to the next sampling location for averaging the images and improving the SNR.

7.6.1.2 *ncDCS data collection*

For the ncDCS data acquisition, a text file containing four tabulated intensity autocorrelation curves and the shared time delay vector (τ) are stored for each repeated measure. Given the fact that the ncDCS signals are self-normalized with respect to their light intensity, the dependence of the autocorrelation curve with respect to the detection distance (ρ_i^{ncDCS}) is recovered by using a multi-distance detection scheme as modeled previously in Figure 2.9a of the Section 2.5.2. An illustration of a representative set of real ncDCS normalized intensity autocorrelation curves (g_2) is shown in Figure 7.11.

In the ncDCS data acquisition, the total amount of collected autocorrelation functions would have the same dependence as the ncDRS explained earlier. The repeated normalized intensity autocorrelation curves provide the feasibility to average over repetitions for improving the Signal-to-Noise Ratio (SNR).

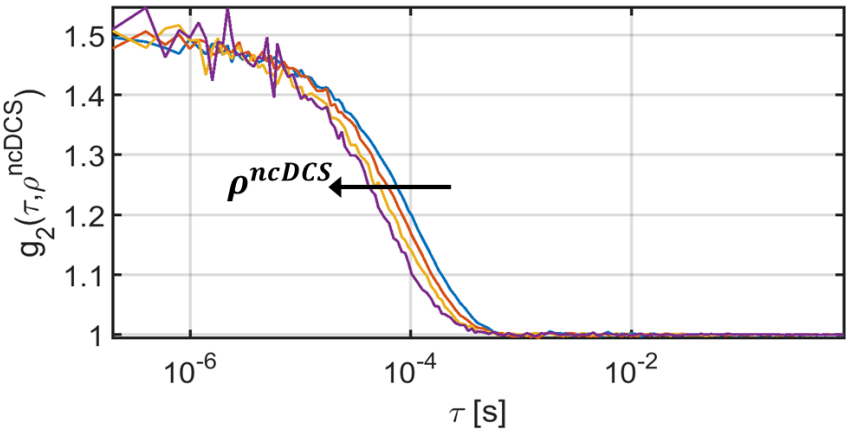

Figure 7.11: The set of normalized intensity autocorrelation functions (g_2) retrieved from the ncDCS measurements. The dependence of the decorrelation time of the signal with respect to the source-detector separation is illustrated, the longest the source-detector separation the fastest the intensity autocorrelation function decay.

7.6.2 *Further details on data processing*

The set of collected images and files from the hybrid ncDRS/ncDCS device describes the optical properties of the probed media. However, in contrast with the data collected by the contact setup, the ncDRS/ncDCS information is inherently associated with the optical settings of the system. Thus, by adjusting the optics in the collection path, the focal plane and the spatial resolution (s_r) of the system can be modified according to the desired field-of-view (FOV). This feature provides the possibility to address optical information from a wide variety of source-detector separations in both techniques. Furthermore, by exploiting the use of an oblique angle of incidence to irradiate the sample, the topographic map of the sample' surface can be reconstructed when performing a scanning measurement.

In the ncDRS/ncDCS device, the source-detector separation are determined by the resolution of the system. Therefore, a spatial cali-

bration of both techniques needs to be done from a series of images collected prior the data acquisition.

In the following sections, a detailed description of the spatial calibration of both the ncDRS and the ncDCS, the data processing and the reconstruction of the topological surface map data is discussed.

7.6.2.1 *ncDRS spatial calibration*

The determination of the source-detector separations in the ncDRS device (ρ_i^{ncDRS}), where i stands for the i^{th} source-detector separation, requires the acquisition of a spatial reference image (Figure 7.17b) with well distributed spatial markers. To this end, an image of a back-illuminated resolution target (R3L3S6P Positive NBS 1952, Throlabs GmbH, Germany) (Figure 7.17a) is acquired. The resolution target contains groups of equally spaced lines with different line-widths. For our purposes, the group of lines with a resolution of 0.48 $^{linepairs}/_{mm}$ and a $\approx$ 0.1 cm inter-line separation is employed (Figure 7.17b).

The ncDRS device allows for imaging a line - due to the spectrometer slit - over the probed surface, therefore, the resolution target is placed orthogonally to the entrance slit of the spectrometer. In this manner, the line pattern of the resolution target would be imaged as a set of squared-pulse signals (Figure 7.17b), where the inter-pulse separation are proportional to the physical inter-line separation in the resolution target. Besides, since the maximum quantum efficiency of the CCD camera is located at 683 nm, the spatial information of that wavelength from the spatial reference image is employed for processing the acquired signal.

The spatial resolution (s_r) [cm/pixel] represents the number of pixels between the falling and rising edges of the acquired signal that are proportional to the physical inter-line separation ($\approx$ 0.1 cm) in the resolution target.

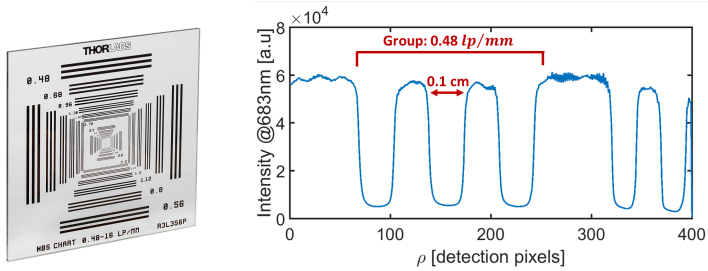

(a) Resolution target **(b)** Calibration image from the resolution target

Figure 7.12: The ncDRS resolution target and the calibration image. The analysis of the spatial reference image of the ncDRS device. a) The resolution target used for acquiring the ncDRS calibration image. Illustration taken from thorlabs.com; b) The spatial reference image of the group of lines with a 0.48 $^{linepairs}/_{mm}$ - around 0.1 cm inter-line separations- resolution taken from the resolution target.

The spatial resolution estimation can be improved by taking the derivative of the squared signal (Figure 7.13). There, the inter-line distance is represented by the number of pixels between the minimum and maximum signal peaks. Since the resolution target has a set of three inter-line separations, the S_r is given by the mean distance between the minimum and maximum peaks corresponding to each separation.

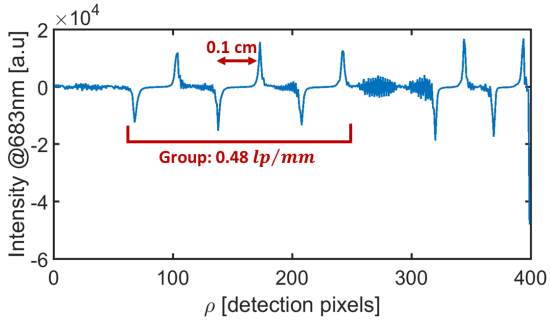

Figure 7.13: The derivative of the ncDRS calibration image. The maximum and minimum peaks, associated to the falling and rising edges of the square signal, provides a more robust determination of the number of pixels between the imaged lines with respect to the physical inter-line separation ($\approx$ 0.1 cm) in the resolution target.

Once the spatial resolution of the ncDRS device has been calculated, the source-detector separations (ρ_i^{ncDRS}) can be estimated for each of the acquired optical data images. To this end, the pixel location of the maximum intensity peak at the highest quantum efficiency wavelength (683 nm) has to be determined. Such position is related to source incidence location on the sample' surface and hence to the zero source-detector separation. From that reference point, the source-detector separations can be determined through the knowledge of the recently computed spatial resolution (S_r) of the system which refers to the number of pixels proportional to $\approx$ 0.1 cm (Figure 7.14).

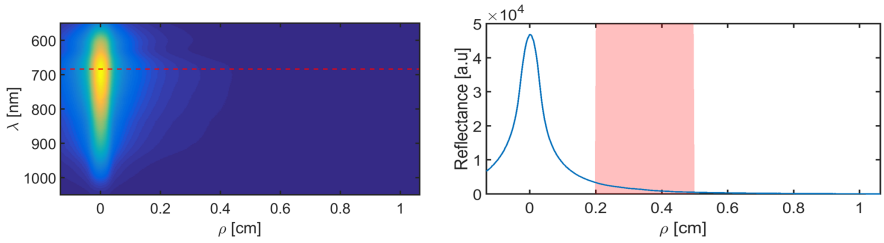

(a) Spatially calibrated ncDRS image **(b)** Spatially calibrated ncDRS signal

Figure 7.14: The ncDRS spatially calibrated image. An illustrative example of the spatial calibration of the ncDRS data. a) The spatially calibrated ncDRS, where the horizontal red dotted line refers to the data at 683 nm (the highest quantum efficiency); b) The spatially calibrated ncDRS signal at 683 nm. The red area denotes the region with source-detector separations (ρ_i^{ncDRS}) ranging from 0.2 cm to 0.5 cm.

7.6.2.2 *ncDCS spatial calibration*

The determination of the source-detector separations in the ncDCS device (ρ_i^{ncDCS}) requires a series of steps. First, a 99% diffuse reflectance standard (SRS-99-010 Spectralon, Labsphere Inc., USA) is placed at the focal plane of the ncDRS CCD camera. Then, highly attenuated laser light ($\approx$ 45 dB) is emitted through the calibration source fiber of the ncDCS ferrule (Figure 7.2), reaching the reflectance standard through the light collection optical path. At the same time, white light from the ncDRS setup is irradiated through the main ncDRS/ncDCS source fiber, reaching the reflectance standard through the emission optical path. The two light spots, focused on the surface of the reflectance standard, are made to overlap. To this end, the position of the ncDCS ferrule is adjusted through the translation mount (CXYZ1/M, Thorlabs GmbH, Germany) in which it is attached to displace the laser spot over the reflectance standard surface. To warranty their overlap, a set of images from the laser and white light are taken in a tandem fashion with the 2D-spectrometer of the ncDRS device. The controlling software displays on the screen the pixel location of the maximum peak intensity of the detected signal at a given wave-

length (in this case 785 nm), allowing the correct positioning of the ncDCS ferrule to achieve the overlapping of the light spots.

Afterwards, the same highly attenuated laser light is delivered through any of the ncDCS detection fibers. The ncDRS device images the back-reflected light, and again, the pixel location of the maximum peak intensity is displayed. Taking advantage of the previously known spatial resolution term (S_r) the source-detector separations of the ncDCS device (ρ_i^{ncDCS}) can be estimated (Figure 7.17). Since the ncDCS detection fibers are equally spaced in the ferrule, by knowing the detection distances of two ncDCS detection fibers with respect to the incidence of the light (red line in Figure 7.17a), the rest can be estimated. Therefore, the most convenient source-detector separations can be selected.

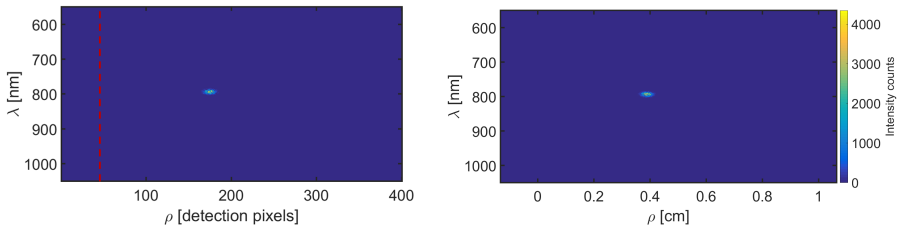

(a) ncDCS calibration raw image **(b)** Spatially calibrated ncDCS image

Figure 7.15: The ncDRS spatial calibration. An illustrative example of the spatial calibration of the ncDCS data when the laser and broadban light spots are overlapping. a) The acquired image of the laser light by the ncDRS device shows the spatial location of the spot on the CCD surface, which is proportional to the physical distance from the source position (vertical red dotted line at pixel index # 50); b) By knowing the spatial resolution of the system (S_r) the corresponding distance of the ncDCS spot with respect to the source (ρ_i^{ncDCS}) can be estimated for a given ncDCS detection fiber.

It is important to note that the ncDCS calibration is based only on the displacement of the ncDCS ferrule for overlapping both the laser and broadband light spots. This procedure is necessary since by moving the optics in the light collection path, the spatial resolution of the

system would be modified, and hence, a re-calibration of the ncDRS setup would be needed.

7.6.3 *ncDRS data processing*

Given the fact that at the moment that the ncDRS/ncDCS device was being developed and validated, the previously introduced algorithm (Chapter 4) was not yet fully developed, the previous data processing approach employed by the group was utilized for processing the non-contact data. This method of processing the data is here below introduced and further details can be found in the previous group publications [2, 112].

As a first step, similar to the new approach introduced earlier (Section 4.1), the dark intensity $I_d(\lambda, \rho_i^{ncDRS})$ is subtracted from both, the measured main source intensities and from the calibration image acquired prior the data acquisition to account for any background light:

$$I_m^{'}(\lambda, \rho_i^{ncDRS}) = I_m(\lambda, \rho_i^{ncDRS}) - I_d(\lambda, \rho_i^{ncDRS})$$
$$I_c^{'}(\lambda, \rho_i^{ncDRS}) = I_c(\lambda, \rho_i^{ncDRS}) - I_d(\lambda, \rho_i^{ncDRS})$$

Here we note the absence of the *source* and *detector coupling coefficients* due to the usage of the same optical path for delivering and collecting light.

Afterwards, the dark subtracted main source light intensity, denoted by $I_m^{'}(\lambda, \rho_i^{ncDRS})$, was divided by its corresponding dark subtracted calibration image, represented by $I_c^{'}(\lambda, \rho_i^{ncDRS})$. This procedures allows the correction of the sensitivity variations among pixels for harvesting light. The resulting self-calibrated light intensity, $I_{sc}(\lambda, \widetilde{\rho}_i^{ncDRS})$ where the term $\widetilde{\rho}_i^{ncDRS}$ refers to the i^{th} self-calibrated detector, is depicted as:

$$I_{sc}(\lambda, \widetilde{\rho}_i^{ncDRS}) = \frac{I_m^{'}(\lambda, \rho_i^{ncDRS})}{I_c^{'}(\lambda, \rho_i^{ncDRS})}$$

During the rest of the data analysis, a total of N = 12 source-detector separations ranging between 0.2 to 0.5 cm, the same range as in the contact device, were employed. For improving the signal-to-noise ratio (SNR), seven pixel were average on the spatial dimension, corresponding the spatial bands of around 0.2 mm.

The following step consisted on the calculation of the ratio between two of these signals, which allows to account for the spectral shape of the CCD quantum efficiency and the lamp spectral emission efficiency. Here we note that, when employing the contact probe under this procedure, a further calibration was done by a source fiber located equidistant to all detector fibers in order to take into account the differences in light transmission between the fibers and differences in their coupling to the tissue.

The employed signal ratios (i, j) arise from the signals located at distances within 0.4 to 0.5 cm as numerators (represented by $\overset{*}{i}$) and within 0.2 to 0.3 cm as denominators (represented by $\overset{*}{j}$) of the fraction; regardless the employed system (contact or non-contact). In this manner, the signal ratios being employed in the DRS analysis (I^{DRS}) for recovering the tissue optical properties and hence, the hemodynamics parameters can be expressed by:

$$I^{DRS}(\lambda, \widetilde{\rho}^{ncDRS}_{\overset{*}{i}}, \widetilde{\rho}^{ncDRS}_{\overset{*}{j}}) = \frac{I_{sc}(\lambda, \widetilde{\rho}^{ncDRS}_{\overset{*}{i}})}{I_{sc}(\lambda, \widetilde{\rho}^{ncDRS}_{\overset{*}{j}})} \tag{7.1}$$

Similarly, the same signal ratios can be applied to the Green's function (G^{DRS}) solution to the photon diffusion equation (Equation 2.9), being expressed as:

$$G^{DRS}(\lambda, \widetilde{\rho}^{ncDRS}_{\overset{*}{i}}, \widetilde{\rho}^{ncDRS}_{\overset{*}{j}}) = \frac{G(\lambda, \widetilde{\rho}^{ncDRS}_{\overset{*}{i}})}{G(\lambda, \widetilde{\rho}^{ncDRS}_{\overset{*}{j}})} \tag{7.2}$$

By numerically Equation 7.1 to Equation 7.2 for each signal ratio $\overset{*}{i},\overset{*}{j}$ independently using a non-linear least square minimization method (LSQNONLIN with Levenberg-Marqardt algorithm, MATLAB, The MathWorks Inc., USA), the parameters A_0, b and c_i (See Chapter 2), representing the componentes of the reduced scattering (μ_s') and absorption (μ_a) coefficients can be obtained through the following objective function:

$$\chi^2 = \sum_{k=1}^{N_\lambda} \left[G^{DRS}(\lambda, \widetilde{\rho}_{\overset{*}{i}}^{ncDRS}, \widetilde{\rho}_{\overset{*}{j}}^{ncDRS}) - I^{DRS}(\lambda, \widetilde{\rho}_{\overset{*}{i}}^{ncDRS}, \widetilde{\rho}_{\overset{*}{j}}^{ncDRS}) \right]^2$$

Where N_λ represent the total number of adjusted wavelengths. This approach provide hence an independent result for each $\overset{*}{i},\overset{*}{j}$ pair, therefore, the mean value over the recovered set values is reported.

7.6.4 *ncDCS data processing*

The collected ncDCS signals (N = 4) comprises a set of self-normalized intensity autocorrelation functions ($g_2^m(\tau, \rho_i^{ncDCS})$), where m stands for the measured data, τ is the decorrelation time and the term ρ_i^{ncDCS} represents the measured signal at the i^{th} detection distance. Since these signals are self-normalized, no further calibration needs to be performed.

How ever, the g_2^m signals need to be converted into the measured normalized electric field autocorrelation function g_1^m in order to match the theoretical model. To this end, the Siegert relation [97] is employed:

$$g_1^m(\tau, \rho_i^{nbDCS}) = \sqrt{\frac{g_2^m(\tau, \rho_i^{nbDCS}) - 1}{\beta_i}} \tag{4.15}$$

Where the system constant $\beta_i \approx 0.5$ needs to be estimated for each measured signal. The resulting g_1^m signals can be fit to the theoreti-

cal self-normalized electric field autcorrelation function (g_1^t), repeated below to remind the reader, to obtain the dynamic information of the probed media:

$$g_1^t(\tau, \rho_i^{ncDCS}) = \frac{\left[\frac{exp[-K(\tau)r_1]}{r_1} - \frac{exp[-K(\tau)r_b]}{r_b}\right]}{\left[\frac{exp[-K(\tau=0)r_1]}{r_1} - \frac{exp[-K(\tau=0)r_b]}{r_b}\right]} \tag{2.15}$$

with

$$K(\tau) = \sqrt{3\mu_s'\mu_a + 6k_0^2\mu_s'^2\alpha D_b\tau}$$

Where the tissue optical properties (μ_s' and μ_a) were previously estimated through the ncDRS analysis and fed into the model.

In this manner, numerical fitting of Equation 4.15 to Equation 2.15 using a non-linear least square minimization method (LSQNONLIN with Levenberg-Marqardt algorithm, MATLAB, The MathWorks Inc., USA) can provide the optimum values for the β_i and D_{bi} parameters for signal detected at the i^{th} detection distance simultaneously through a the following objective function:

$$\chi^2 = \sum_{j=1}^{N_\tau} \left[g_1^t(\tau_j, \rho_i^{ncDCS}) - g_1^m(\tau_j, \rho_i^{ncDCS}) \right]^2 \tag{7.3}$$

Where N_τ represents the total number of sampled time points. This approach provide hence an independent flow value D_{bi} for each measured signal, therefore, the magnitude of the flow in the probed medium is given by the mean value of the recovered parameters.

7.6.5 *Reconstruction of the topological surface map*

During the ncDRS optical data acquisition in a scanning fashion, complementary information to the tissue optical properties such as

the topological sample' surface map can be recovered. To this end, the usage of an oblique angle of incidence for irradiating light into the tissue is exploited. Therefore, by tracking the maximum intensity peak at a given wavelength in the collected ncDRS images, commonly that with the maximum quantum efficiency (e.i. 683 nm), the differences in height due to physical displacement of the sample (Δx) would be reflected into variations in the pixel position (Δp) of the maximum intensity peak.

Hence, by knowing the spatial resolution (S_r) of the device as well as the angle of incidence of the incoming light ($\theta \approx$ -10°), the magnitude of the displacement in pixels can be related to the difference in height (Δh) of the sample as:

$$\Delta h = -\frac{S_r \times \Delta p}{tan(\theta)} \tag{7.4}$$

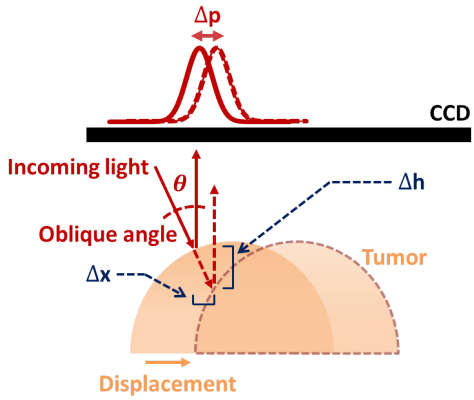

Figure 7.16: Theoretical reconstruction of the topographic map. The reconstruction of the topographic surface' sample map relies on the usage of incoming light with an oblique angle of incidence ($\theta \approx$ -10°) on the tissue in addition to the knowledge of the spatial resolution (S_r) of the device. The spatial displacement (Δx) of the sample (e.g. tumor) causes a variation in the pixel position of the maximum intensity peak in the recorded image. Therefore, by using a trigonometric approach while keeping track of the pixel displacement (Δp) of the intensity peak, the reconstruction of the topographic map is achieved.

An illustration of a recovered topographic map from a scanned region of interest (ROI) of a *in vivo* measurement in contrast with the real scanned surface is shown below:

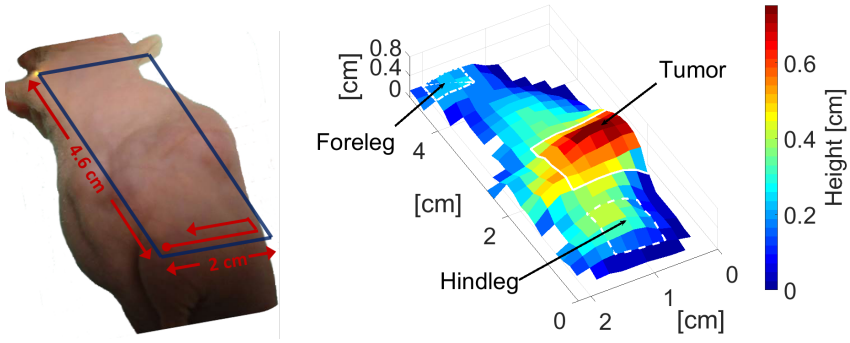

(a) Scanned ROI **(b)** Recovered topographic map

Figure 7.17: Illustration of an *in vivo* recovery of a topographic map. An illustrative example of the recovery of a topographich map from *in vivo* experimental measurements. a) The scanned region of interest (ROI) over the mouse left side; b) The recovered height map corresponding to the scanned ROI.

Beyond the reconstruction of the topographic map, the tracking of the maximum intensity peak pixel position allows to further implement other functionalities. For instance, by setting an initial height location associated with a particular pixel position of the maximum intensity peak, an auto-focusing of the system can be achieved. To this end, the displacement in pixels of the maximum peak intensity is backward associated to a change in height. Therefore, by translating the sample in the z-axis the proportional height change but in the opposite direction, the sample can be replaced on the system's focal plane for collecting optical data. This functionality has also been implemented in this setup although results are not shown.

8

CONCLUSIONS & OUTLOOK

The bulk of this dissertation focused on the pre-clinical investigation of the renal cell carcinoma which, despite not being one of the most common cancers worldwide and hence barely explored, represents one of the most challenging cancer types due to the high prevalence of tumor resistance. In a multi-disciplinary collaboration involving groups in medical optics, plasmon nano-photonics and cancer biology, I have further develop a non-invasive, optical platform that could, in principle be translated to human use, for the study of an anti-angiogenic therapy (Sunitinib) on this model. I have also introduced the same platform for the in vivo characterization of the gold nanorod concentration and its effects on tumor hemodynamics, hence paving the way towards the development of a heuristic approach for plasmon enhanced photothermal therapy.

I have taken advantage of a combination of two diffuse optical techniques, broadband diffuse reflectance spectroscopy (DRS) and diffuse correlation spectroscopy (DCS) that have been incorporated into a platform with a convenient, compact, contact probe for these measurements (Chapter 3). I have had to overcome challenges about the preprocessing of the raw data and its modeling which has enabled me to achieve robust and repeatable results. This comprehensive approach for processing the data has been developed and introduced to account for several artifacts which turned out to be fundamental for a proper estimation of the tissue physiology (Chapter 4). The proposed method comprises a series of steps that accounts for each of the artifacts that disrupt the collected signals, minimizing their effects. This methodology facilitates the retention of the maximum amount of data for extracting the most reliable information. Moreover, the new algorithm

allows for a dynamic and unattended optical data processing, being capable to adapt to the static and dynamic properties of the probed tissue; hence, being suitable for longitudinal therapy monitoring with potential translatability for the study of other pre-clinical models and to the clinics. The advantages of the hybrid contact DRS/DCS device and the developed data processing method were shown throughout the studies presented in Chapter 5 and in Chapter 6.

In Chapter 5, the estimated tumor hemodynamics (THC, SO_2 and BFI) were demonstrated to be a potential set biomarkers capable to predict the tumor resistance to Sunitinib (an anti-angiogenic drug) from the pre-treatment measurements. This finding, if confirmed in larger and more heterogeneous studies, would represent a key advance in the translational oncology field towards the understanding of the tumor intrinsic resistance mechanisms as well as for the development of personalized treatments. In addition, the longitudinally monitored tissue hemodynamics were demonstrated to be predictive of the therapy effects (final micro vessel density and tumor weight) from the early (within days) observed changes; and in the long-term, to allow the distinction of the therapy outcome (responder or non-responder). This should enable the early adjustment of the therapy strategies to fit the needs of an individual patient, possibly allowing for earlier action, reduced morbidity and suffering.

In Chapter 6, diffuse optical methods were demonstrated to be a suitable tool-box for the quantitative evaluation of the potential interactions of the circulating gold nanoparticles in the blood-stream with the tissue hemodynamics. In this regard, the main challenging aspect of the experiment arose from the broad light-absorption spectrum proper of the PEGylated gold nanorods (AuNRs-PEG), which is coupled into the coverage of the spectral features of the existing chromophores in the probed tissue; therefore, preventing the proper estimation of the tissue hemodynamics. I have demonstrated that the new algorithm that I have developed is capable of decoupling the contribution of the hemodynamics from that of an inorganic contrast agent

(i.e. AuNRs-PEG) by enhancing their corresponding spectral features and adapting the optimum wavelength bands for a better disentanglement of both parameters. This meant that we are now able to to quantify simultaneously, for the first time, the *in vivo* tissue hemodynamics and the AuNR-PEG concentration in a non-invasive and longitudinal fashion. This was applied to the study of the same tumor and we have concluded that the gold nanorods do not interact significantly with the tissue physiology, In this context, our findings represents a suitable method to study the toxicity and side-affects derived from the usage of gold nanoparticles; although they can potentially be translated to the study of other contrast agents in a manifold of nanomedical platforms, from the pre-clinics to the clinics. On top of that, this work, by allowing the *in vivo* characterization of the gold nanorod concentration in deeper tissue layers, provides a method for exploiting their theranostic capabilities as contrast agents for imaging tissue structures, nanovectors for deploying drug payloads and therapeutic agents for performing thermal-based therapies. Among these applications of the gold nanorods, the plasmon-based photo-thermal therapies are of particular interest as niche for the enhancement of the current cancer therapies. In a yet unfinished study, I am working with collaborators using this new platform and the algorithms during pilot studies of photothermal therapy. Initial results are quite promising and demonstrate the utility of this platform. They will be the topic of future monographs and publications.

Beyond the demonstrated potential of the contact hybrid DRS/DCS device to provide valuable information in several research fields, some artifacts and limitations associated to its inherent nature of requiring an optimum tissue-probe contact and pressure as well as the manual relocation of the probe onto the tissue, might prevent it from collecting large amount of information in a reliable manner. To this end, I have collaborated with others [112] on the design and instrumentation of a novel non-contact, scanning hybrid DRS/DCS device to further enhance the demonstrated capabilities of the diffuse optical methods

(Chapter 7). The device was validated on tissue simulating phantoms and testing as a 2D scanning platform *in vivo* for recovering the tissue hemodynamics from a set of mice with ccRCC tumors, the same mice were also probed with the contact DRS/DCS device in order to contrast the recovered results from both approaches. The estimated tissue hemodynamics from the non-contact device were observed to be in agreement with those obtained by the contact version, demonstrating the feasibility to overcome the previously introduced artifacts while retaining an accurate quantification of the parameters. Furthermore, the flexibility of the non-contact device to spatially resolve with a high-density of detectors, open the door to the further improvement of the device by developing a tomographic approach for collecting and processing the data.

Overall, in this dissertation the frontiers of the translational oncology and nanobiophotonics fields have been pushed by providing relevant insights towards the development of future applications of diffuse optical technologies. These results present an initial step towards the development of future theranostic approaches to therapies by accomplishing a better understanding of these fields.

BIBLIOGRAPHY

1. Farzam, P. *Hybrid diffuse optics for monitoring of tissue hemodynamics with applications in oncology* PhD thesis (ICFO - The Institute of Photonic Sciences, 2014) (cit. on pp. 1, 27, 28, 30, 37, 136).
2. Farzam, P., Johansson, J., Mireles, M., Jiménez-Valerio, G., Martínez-Lozano, M., Choe, R., Casanovas, O. & Durduran, T. Pre-clinical longitudinal monitoring of hemodynamic response to anti-vascular chemotherapy by hybrid diffuse optics. *Biomed. Opt. Express* **8,** 2563 (2017) (cit. on pp. 1, 37, 38, 70, 122, 146, 156).
3. Siemann, D. W., Chaplin, D. J. & Horsman, M. R. Vascular-targeting therapies for treatment of malignant disease. *Cancer* **100,** 2491–2499 (2004) (cit. on pp. 1, 2, 70).
4. Baudino, T. Targeted Cancer Therapy: The Next Generation of Cancer Treatment. *Curr. Drug Discov. Technol.* **12,** 3–20 (2015) (cit. on pp. 1, 2).
5. Moserle, L., Jimenez-Valerio, G. & Casanovas, O. Antiangiogenic Therapies: Going beyond Their Limits. *Cancer Discov.* **4,** 31–41 (2014) (cit. on pp. 1, 69).
6. Casanovas, O. Cancer: Limitations of therapies exposed. *Nature* **484,** 44–46 (2012) (cit. on p. 1).
7. Jiménez-Valerio, G. *et al.* Resistance to Antiangiogenic Therapies by Metabolic Symbiosis in Renal Cell Carcinoma PDX Models and Patients. *Cell Rep.* **15,** 1134–1143 (2016) (cit. on pp. 1, 69, 72, 94, 96, 104, 134).

8. Duran, I., Lambea, J., Maroto, P., González-Larriba, J. L., Flores, L., Granados-Principal, S., Graupera, M., Sáez, B., Vivancos, A. & Casanovas, O. Resistance to Targeted Therapies in Renal Cancer: The Importance of Changing the Mechanism of Action. *Target. Oncol.* **12,** 19–35 (2017) (cit. on pp. 1, 2, 69).
9. Namakydoust, A, Holle, L & Clement, J. M. Current therapeutic approaches to renal cell carcinoma. *J. Clin. Outcomes Manag.* **23,** 370–384 (2016) (cit. on p. 1).
10. Koul, H., Huh, J.-S., Rove, K. O., Crompton, L., Koul, S., Meacham, R. B. & Kim, F. J. Molecular aspects of renal cell carcinoma: a review. *Am. J. Cancer Res.* **1,** 240–254 (2011) (cit. on pp. 1, 2).
11. Butler, B. P., Novick, A. C., Miller, D. P., Campbell, S. A. & Licht, M. R. Management of small unilateral renal cell carcinomas: Radical versus nephron-sparing surgery. *Urology* **45,** 34–40 (1995) (cit. on p. 2).
12. Yagoda, A, Petrylak, D & Thompson, S. Cytotoxic chemotherapy for advanced renal cell carcinoma. *The Urologic clinics of North America* **20,** 303—321 (1993) (cit. on p. 2).
13. Motzer, R. J. & Russo, P. Systemic therapy for renal cell carcinoma. *J. Urol.* **163,** 408–417 (2000) (cit. on p. 2).
14. Rini, B. I., Weinberg, V. & Small, E. J. A Phase I trial of fixed dose rate gemcitabine and capecitabine in metastatic renal cell carcinoma. *Cancer* **103,** 553–558 (2005) (cit. on p. 2).
15. Stadler, W. M., Halabi, S., Rini, B., Ernstoff, M. S., Davila, E., Picus, J., Barrier, R. & Small, E. J. A phase II study of gemcitabine and capecitabine in metastatic renal cancer. *Cancer* **107,** 1273–1279 (2006) (cit. on p. 2).
16. Posadas, E. M., Limvorasak, S. & Figlin, R. A. Targeted therapies for renal cell carcinoma. *Nat. Rev. Nephrol.* **13,** 496–511 (2017) (cit. on p. 2).

17. Ellis, L. M. & Hicklin, D. J. VEGF-targeted therapy: mechanisms of anti-tumour activity. *Nat. Rev. Cancer* **8,** 579–591 (2008) (cit. on pp. 2, 69, 70).

18. Powles, T., Chowdhury, S., Jones, R., Mantle, M., Nathan, P., Bex, A., Lim, L. & Hutson, T. Sunitinib and other targeted therapies for renal cell carcinoma. *Br. J. Cancer* **104,** 741–745 (2011) (cit. on p. 2).

19. Papaetis, G. S. & Syrigos, K. N. Sunitinib: a multitargeted receptor tyrosine kinase inhibitor in the era of molecular cancer therapies. *BioDrugs* **23,** 377–89 (2009) (cit. on pp. 2, 69, 93).

20. O'Farrell, A.-M. *et al.* SU11248 is a novel FLT3 tyrosine kinase inhibitor with potent activity in vitro and in vivo. *Blood* **101,** 3597–605 (2003) (cit. on p. 2).

21. Robinson, S. P., Boult, J. K., Vasudev, N. S. & Reynolds, A. R. Monitoring the Vascular Response and Resistance to Sunitinib in Renal Cell Carcinoma In Vivo with Susceptibility Contrast MRI. *Cancer Res.* **77,** 4127–4134 (2017) (cit. on pp. 2, 96).

22. Santos, C. D., Tijeras-Raballand, A., Serova, M., Sebbagh, S., Slimane, K., Faivre, S., de Gramont, A & Raymond, E. Effects of preset sequential administrations of sunitinib and everolimus on tumour differentiation in Caki-1 renal cell carcinoma. *Br. J. Cancer* **112,** 86–94 (2015) (cit. on p. 2).

23. Coppin, C., Kollmannsberger, C., Le, L., Porzsolt, F. & Wilt, T. J. Targeted therapy for advanced renal cell cancer (RCC): a Cochrane systematic review of published randomised trials. *BJU Int.* **108,** 1556–1563 (2011) (cit. on pp. 2, 69).

24. Motzer, R. J. *et al.* Sunitinib versus Interferon Alfa in Metastatic Renal-Cell Carcinoma. *N. Engl. J. Med.* **356,** 115–124 (2007) (cit. on p. 2).

25. Lim, S. H., Hwang, I. G., Ji, J. H., Oh, S. Y., Yi, J. H., Lim, D. H., Lim, H. Y., Lee, S. J. & Park, S. H. Intrinsic resistance to sunitinib in patients with metastatic renal cell carcinoma. *Asia. Pac. J. Clin. Oncol.* **13,** 61–67 (2017) (cit. on pp. 2, 93).

26. Ferrari, M. Cancer nanotechnology: opportunities and challenges. *Nat. Rev. Cancer* **5,** 161–171 (2005) (cit. on pp. 2, 100).

27. Thakor, A. S. & Gambhir, S. S. Nanooncology: The future of cancer diagnosis and therapy. *CA. Cancer J. Clin.* **63,** 395–418 (2013) (cit. on pp. 2, 100).

28. Hartshorn, C. M., Bradbury, M. S., Lanza, G. M., Nel, A. E., Rao, J., Wang, A. Z., Wiesner, U. B., Yang, L. & Grodzinski, P. Nanotechnology Strategies To Advance Outcomes in Clinical Cancer Care. *ACS Nano* **12,** 24–43 (2018) (cit. on pp. 2, 100).

29. Huang, X., Jain, P. K., El-Sayed, I. H. & El-Sayed, M. A. Plasmonic photothermal therapy (PPTT) using gold nanoparticles. *Lasers Med. Sci.* **23,** 217–228 (2008) (cit. on pp. 2, 3, 100).

30. Brongersma, M. L., Halas, N. J. & Nordlander, P. Plasmon-induced hot carrier science and technology. *Nat. Nanotechnol.* **10,** 25–34 (2015) (cit. on pp. 2, 100).

31. Baffou, G. & Quidant, R. Thermo-plasmonics: using metallic nanostructures as nano-sources of heat. *Laser Photon. Rev.* **7,** 171–187 (2013) (cit. on pp. 2, 100).

32. Sanchot, A., Baffou, G., Marty, R., Arbouet, A., Quidant, R., Girard, C. & Dujardin, E. Plasmonic Nanoparticle Networks for Light and Heat Concentration. *ACS Nano* **6,** 3434–3440 (2012) (cit. on pp. 2, 100).

33. Kennedy, L. C., Bickford, L. R., Lewinski, N. A., Coughlin, A. J., Hu, Y., Day, E. S., West, J. L. & Drezek, R. A. A New Era for Cancer Treatment: Gold-Nanoparticle-Mediated Thermal Therapies. *Small* **7,** 169–183 (2011) (cit. on pp. 2, 100).

34. Abadeer, N. S. & Murphy, C. J. Recent Progress in Cancer Thermal Therapy Using Gold Nanoparticles. *J. Phys. Chem. C* **120,** 4691–4716 (2016) (cit. on pp. 3, 100).

35. Dolmans, D. E., Fukumura, D. & Jain, R. K. Photodynamic therapy for cancer. *Nat. Rev. Cancer* **3,** 380–387 (2003) (cit. on p. 3).

36. Wang, H.-w., Putt, M. E., Emanuele, M. J., Shin, D. B., Glatstein, E., Yodh, A. G. & Busch, T. M. Treatment-induced changes in tumor oxygenation predict photodynamic therapy outcome. *Cancer Res.* **64,** 7553–61 (2004) (cit. on pp. 3, 27, 121).

37. Wang, H.-W. *et al.* Quantitative comparison of tissue oxygen and motexafin lutetium uptake by ex vivo and noninvasive in vivo techniques in patients with intraperitoneal carcinomatosis. *J. Biomed. Opt.* **12,** 034023 (2007) (cit. on p. 3).

38. Mesquita, R. C., Han, S. W., Miller, J., Schenkel, S. S., Pole, A., Esipova, T. V., Vinogradov, S. A., Putt, M. E., Yodh, A. G. & Busch, T. M. Tumor Blood Flow Differs between Mouse Strains: Consequences for Vasoresponse to Photodynamic Therapy. *PLoS One* **7** (ed Hamblin, M.) e37322 (2012) (cit. on pp. 3, 122).

39. Busch, T. M., Xing, X., Yu, G., Yodh, A., Wileyto, E. P., Wang, H.-W., Durduran, T., Zhu, T. C. & Wang, K. K.-H. Fluence rate-dependent intratumor heterogeneity in physiologic and cytotoxic responses to Photofrin photodynamic therapy. *Photochem. Photobiol. Sci.* **8,** 1683 (2009) (cit. on pp. 3, 121).

40. Yu, G., Durduran, T., Zhou, C., Wang, H.-w., Putt, M. E., Saunders, H. M., Sehgal, C. M., Glatstein, E., Yodh, A. G. & Busch, T. M. Noninvasive monitoring of murine tumor blood flow during and after photodynamic therapy provides early assessment of therapeutic efficacy. *Clin. Cancer Res.* **11,** 3543–52 (2005) (cit. on pp. 3, 121, 122, 143).

41. Durduran, T, Choe, R, Baker, W. B. & Yodh, a. G. Diffuse optics for tissue monitoring and tomography. *Reports Prog. Phys.* **73,** 076701 (2010) (cit. on pp. 5, 11, 16, 101, 121).

42. Yodh, A. & Chance, B. Spectroscopy and Imaging with Diffusing Light. *Phys. Today* **48,** 34–40 (1995) (cit. on pp. 5, 101).

43. Chance B, A. R. *Proceedings of Optical Tomography, Photon Migration, and Spectroscopy of Tissue and Model Media: Theory, Human Studies, and Instrumentation* 2379 (SPIE, 1995) (cit. on p. 5).

44. Niemz, M. H. *Laser-Tissue Interactions* (Springer Berlin Heidelberg, 2002) (cit. on p. 5).

45. Kulikov, K. *Laser Interaction with Biological Material* (Springer International Publishing, 2014) (cit. on p. 5).

46. Zhou, C. *In-vivo optical imaging and spectroscopy of cerebral hemodynamics* PhD thesis (University of Pennsylvania, 2007) (cit. on pp. 6, 19, 62).

47. Yodh A.G, B. D. *Functional Imaging with Diffusing Light* 1–45 (CRC Press, 2003) (cit. on p. 5).

48. Jobsis, F. Noninvasive, infrared monitoring of cerebral and myocardial oxygen sufficiency and circulatory parameters. *Science (80-.).* **198,** 1264–1267 (1977) (cit. on p. 6).

49. Prahl, S. *Values compiled by Scott Prahl with data provided by W. B. Gratzer, Med. Res. Council Labs, Holly Hill, London; N. Kollias, Wellman Laboratories, Harvard Medical School, Boston, and others* `https://omlc.org/spectra/hemoglobin/index.html` (cit. on pp. 7, 74, 109, 135).

50. Matcher, S. J., Cope, M & Delpy, D. T. Use of the water absorption spectrum to quantify tissue chromophore concentration changes in near-infrared spectroscopy. *Phys. Med. Biol.* **39,** 177–196 (1994) (cit. on pp. 7, 74, 109, 135).

51. Matcher, S., Elwell, C., Cooper, C., Cope, M. & Delpy, D. Performance Comparison of Several Published Tissue Near-Infrared Spectroscopy Algorithms. *Anal. Biochem.* **227** (eds Chance, B. & Alfano, R. R.) 54–68 (1995) (cit. on pp. 7, 74, 109, 135).

52. Van Veen, R. L. P., Sterenborg, H. J.C. M., Pifferi, A., Torricelli, A., Chikoidze, E. & Cubeddu, R. Determination of visible near-IR absorption coefficients of mammalian fat using time- and spatially resolved diffuse reflectance and transmission spectroscopy. *J. Biomed. Opt.* **10,** 054004 (2005) (cit. on p. 7).

53. Durduran, T., Yu, G., Burnett, M. G., Detre, J. a., Greenberg, J. H., Wang, J., Zhou, C. & Yodh, A. G. Diffuse optical measurement of blood flow, blood oxygenation, and metabolism in a human brain during sensorimotor cortex activation. *Opt. Lett.* **29,** 1766–8 (2004) (cit. on p. 7).

54. Tuchin, V. V. *Tissue optics: light scattering methods and instruments for medical diagnosis* 2nd ed., 882 (SPIE Press, 2007) (cit. on p. 8).

55. Jacques, S. L. Corrigendum: Optical properties of biological tissues: a review. *Phys. Med. Biol.* **58,** 5007–5008 (2013) (cit. on p. 8).

56. Heino, J., Arridge, S., Sikora, J. & Somersalo, E. Anisotropic effects in highly scattering media. *Phys. Rev. E* **68,** 031908 (2003) (cit. on p. 8).

57. Cheong, W., Prahl, S. & Welch, A. A review of the optical properties of biological tissues. *IEEE J. Quantum Electron.* **26,** 2166–2185 (1990) (cit. on p. 8).

58. Furutsu, K. Diffusion equation derived from space-time transport equation. *J. Opt. Soc. Am.* **70,** 360 (1980) (cit. on p. 9).

59. Ishimaru, A. Wave propagation and scattering in random media and rough surfaces. *Proc. IEEE* **79,** 1359–1366 (1991) (cit. on p. 9).

60. Groenhuis, R. A. J., Ferwerda, H. A. & Ten Bosch, J. J. Scattering and absorption of turbid materials determined from reflection measurements 1: Theory. *Appl. Opt.* **22,** 2456 (1983) (cit. on p. 9).

61. Durduran, T., Yodh, A. G., Chance, B. & Boas, D. A. Does the photon-diffusion coefficient depend on absorption? *J. Opt. Soc. Am. A* **14,** 3358 (1997) (cit. on p. 10).

62. Delpy, D. T., Cope, M., van der Zee, P, Arridge, S, Wray, S & Wyatt, J. Estimation of optical pathlength through tissue from direct time of flight measurement. *Phys. Med. Biol.* **33,** 1433–1442 (1988) (cit. on p. 10).

63. Jacques, S. Time-resolved reflectance spectroscopy in turbid tissues. *IEEE Trans. Biomed. Eng.* **36,** 1155–1161 (1989) (cit. on p. 10).

64. Patterson, M. S., Chance, B & Wilson, B. C. Time resolved reflectance and transmittance for the noninvasive measurement of tissue optical properties. *Appl. Opt.* **28,** 2331 (1989) (cit. on p. 10).

65. Andersson-Engels, S, Jarlman, O, Berg, R & Svanberg, S. Time-resolved transillumination for medical diagnostics. *Opt. Lett.* **15,** 1179 (1990) (cit. on p. 10).

66. Patterson, M. S., Moulton, J. D., Wilson, B. C., Berndt, K. W. & Lakowicz, J. R. Frequency-domain reflectance for the determination of the scattering and absorption properties of tissue. *Appl. Opt.* **30,** 4474 (1991) (cit. on p. 11).

67. Lakowicz, J. R., Laczko, G., Gryczynski, I., Szmacinski, H. & Wiczk, W. New trends in photobiology: Gigahertz frequency-domain fluorometry: Resolution of complex decays, picosecond processes and future developments. *J. Photochem. Photobiol. B Biol.* **2,** 295–311 (1988) (cit. on p. 11).

68. Pogue, B. W. & Patterson, M. S. Frequency-domain optical absorption spectroscopy of finite tissue volumes using diffusion theory. *Phys. Med. Biol.* **39,** 1157–1180 (1994) (cit. on p. 11).

69. Chance, B., Cope, M., Gratton, E., Ramanujam, N. & Tromberg, B. Phase measurement of light absorption and scatter in human tissue. *Rev. Sci. Instrum.* **69,** 3457–3481 (1998) (cit. on p. 11).

70. Fishkin, J. B. & Gratton, E. Propagation of photon-density waves in strongly scattering media containing an absorbing semi-infinite plane bounded by a straight edge. *J. Opt. Soc. Am. A* **10,** 127 (1993) (cit. on p. 11).

71. Nichols, M. G., Hull, E. L. & Foster, T. H. Design and testing of a white-light, steady-state diffuse reflectance spectrometer for determination of optical properties of highly scattering systems. *Appl. Opt.* **36,** 93 (1997) (cit. on pp. 12, 27).

72. Mourant, J. R., Fuselier, T., Boyer, J., Johnson, T. M. & Bigio, I. J. Predictions and measurements of scattering and absorption over broad wavelength ranges in tissue phantoms. *Appl. Opt.* **36,** 949 (1997) (cit. on p. 12).

73. Doornbos, R. M. P., Lang, R, Aalders, M. C., Cross, F. W. & Sterenborg, H. J.C. M. The determination of in vivo human tissue optical properties and absolute chromophore concentrations using spatially resolved steady-state diffuse reflectance spectroscopy. *Phys. Med. Biol.* **44,** 967–981 (1999) (cit. on p. 12).

74. Farrell, T. J., Patterson, M. S. & Wilson, B. A diffusion theory model of spatially resolved, steady-state diffuse reflectance for the noninvasive determination of tissue optical properties in vivo. *Med. Phys.* **19,** 879–888 (1992) (cit. on p. 12).

75. Kienle, a, Lilge, L, Patterson, M. S., Hibst, R, Steiner, R & Wilson, B. C. Spatially resolved absolute diffuse reflectance measurements for noninvasive determination of the optical scattering and absorption coefficients of biological tissue. *Appl. Opt.* **35,** 2304–14 (1996) (cit. on pp. 12, 145).

76. Sharpless, N. E. & DePinho, R. A. The mighty mouse: genetically engineered mouse models in cancer drug development. *Nat. Rev. Drug Discov.* **5,** 741–754 (2006) (cit. on p. 12).

77. Cheon, D.-J. & Orsulic, S. Mouse Models of Cancer. *Annu. Rev. Pathol. Mech. Dis.* **6,** 95–119 (2011) (cit. on p. 12).

78. Haskell, R. C., Svaasand, L. O., Tsay, T.-T., Feng, T.-C., Tromberg, B. J. & McAdams, M. S. Boundary conditions for the diffusion equation in radiative transfer. *J. Opt. Soc. Am. A* **11,** 2727 (1994) (cit. on p. 14).

79. Aronson, R. Boundary conditions for diffusion of light. *J. Opt. Soc. Am. A* **12,** 2532 (1995) (cit. on p. 14).

80. Kim, M. N. *Applications of Hybrid Diffuse Optics for Clinical Management of Adults after Brain Injury* PhD thesis (University of Pennsylvania, 2013), 283 (cit. on p. 15).

81. Jacques, S. L. & Pogue, B. W. Tutorial on diffuse light transport. *J. Biomed. Opt.* **13,** 041302 (2008) (cit. on p. 16).

82. Seventh Edition (eds Arfken, G. B., Weber, H. J. & Harris, F. E.) 1181 –1205. ISBN: 978-0-12-384654-9 (Academic Press, Boston, 2013) (cit. on p. 16).

83. Barton, G. *Elements of Green's functions and propagation : potentials, diffusion, and waves* ISBN: 9780198519980 (Clarendon Press Oxford University Press, Oxford New York, 1989) (cit. on p. 16).

84. Berne, B. & Pecora, R. *Dynamic light scattering with applications to chemistry, biology, and physics* ISBN: 0486411559 (Dover Publications, Mineola, N.Y, 2000) (cit. on p. 17).

85. Brown, W. *Dynamic light scattering : the method and some applications* ISBN: 978-0198539421 (Clarendon Press Oxford University Press, Oxford England New York, 1993) (cit. on p. 17).

86. Chu, B. *Laser light scattering : basic principles and practice* ISBN: 978-0486457987 (Dover Publications, Mineola, N.Y, 2007) (cit. on p. 17).

87. Briers, J. D. Laser Doppler, speckle and related techniques for blood perfusion mapping and imaging. *Physiol. Meas.* **22,** R35–R66 (2001) (cit. on p. 17).

88. Riva, C, Ross, B & Benedek, G. B. Laser Doppler measurements of blood flow in capillary tubes and retinal arteries. *Invest. Ophthalmol.* **11,** 936–44 (1972) (cit. on p. 17).

89. Stern, M. D., Lappe, D. L., Bowen, P. D., Chimosky, J. E., Holloway, G. A., Keiser, H. R. & Bowman, R. L. Continuous measurement of tissue blood flow by laser-Doppler spectroscopy. *Am. J. Physiol. Circ. Physiol.* **232,** H441–H448 (1977) (cit. on p. 17).

90. Boas, D. A. & Yodh, A. G. Spatially varying dynamical properties of turbid media probed with diffusing temporal light correlation. *J. Opt. Soc. Am. A* **14,** 192 (1997) (cit. on p. 17).

91. Boas, D. *Diffuse photon probes of structural and dynamical properties of turbid media: Theory and biomedical application* PhD thesis (1996), 260. ISBN: 9780591019735 0591019736 (cit. on p. 17).

92. Boas, D. A., Campbell, L. E. & Yodh, A. G. Scattering and Imaging with Diffusing Temporal Field Correlations. *Phys. Rev. Lett.* **75,** 1855–1858 (1995) (cit. on pp. 17, 121).

93. Carp, S. A., Roche-Labarbe, N., Franceschini, M.-A., Srinivasan, V. J., Sakadžić, S. & Boas, D. A. Due to intravascular multiple sequential scattering, Diffuse Correlation Spectroscopy of tissue primarily measures relative red blood cell motion within vessels. *Biomed. Opt. Express* **2,** 2047 (2011) (cit. on p. 18).

94. Boas, D. A., Sakadžic, S., Selb, J., Farzam, P., Franceschini, M. A. & Carp, S. A. Establishing the diffuse correlation spectroscopy signal relationship with blood flow. *Neurophotonics* **3,** 031412 (2016) (cit. on p. 18).

95. Tang, J., Erdener, S. E., Li, B., Fu, B., Sakadzic, S., Carp, S. A., Lee, J. & Boas, D. A. Shear-induced diffusion of red blood cells measured with dynamic light scattering-optical coherence tomography. *J. Biophotonics* **11,** e201700070 (2018) (cit. on p. 18).

96. Sakadžic, S., Boas, D. A. & Carp, S. A. Theoretical model of blood flow measurement by diffuse correlation spectroscopy. *J. Biomed. Opt.* **22,** 027006 (2017) (cit. on p. 18).

97. Lemieux, P.-A. & Durian, D. J. Investigating non-Gaussian scattering processes by using nth -order intensity correlation functions. *J. Opt. Soc. Am. A* **16,** 1651 (1999) (cit. on pp. 19, 158).

98. Maret, G. & Wolf, P. E. Multiple light scattering from disordered media. The effect of brownian motion of scatterers. *Zeitschrift fur Phys. B Condens. Matter* **65,** 409–413 (1987) (cit. on p. 19).

99. Pusey, P. N., Vaughan, J. M. & Willetts, D. V. Effect of spatial incoherence of the laser in photon-correlation spectroscopy. *J. Opt. Soc. Am.* **73,** 1012 (1983) (cit. on p. 19).

100. Bellini, T., Glaser, M. A., Clark, N. A. & Degiorgio, V. Effects of finite laser coherence in quasielastic multiple scattering. *Phys. Rev. A* **44,** 5215–5223 (1991) (cit. on p. 19).

101. Wilson, B. C. *An optical fiber-based diffuse reflectance spectrometer for non-invasive investigation of photodynamic sensitizers in vivo* in *Futur. Dir. Appl. Photodyn. Ther.* (ed Gomer, C. J.) **10306** (1990), 103060H (cit. on p. 27).

102. Hull, E. L., Nichols, M. G. & Foster, T. H. Quantitative broadband near-infrared spectroscopy of tissue-simulating phantoms containing erythrocytes. *Phys. Med. Biol.* **43,** 3381–3404 (1998) (cit. on p. 27).

103. Weersink, R. A., Hayward, J. E., Diamond, K. R. & Patterson, M. S. Accuracy of Noninvasive in vivo Measurements of Photosensitizer Uptake Based on a Diffusion Model of Reflectance Spectroscopy. *Photochem. Photobiol.* **66,** 326–335 (1997) (cit. on p. 27).

104. Solonenko, M., Cheung, R., Busch, T. M., Kachur, A., Griffin, G. M., Vulcan, T., Zhu, T. C., Wang, H.-W., Hahn, S. M. & Yodh, A. G. In vivo reflectance measurement of optical properties, blood oxygenation and motexafin lutetium uptake in canine large bowels, kidneys and prostates. *Phys. Med. Biol.* **47,** 857–73 (2002) (cit. on pp. 27, 121).

105. Hull, E. L., Conover, D. L. & Foster, T. H. Carbogen-induced changes in rat mammary tumour oxygenation reported by near infrared spectroscopy. *Br. J. Cancer* **79,** 1709–1716 (1999) (cit. on pp. 27, 121).

106. Yeganeh, H. Z., Toronov, V., Elliott, J. T., Diop, M., Lee, T.-Y. & St. Lawrence, K. Broadband continuous-wave technique to measure baseline values and changes in the tissue chromophore concentrations. *Biomed. Opt. Express* **3,** 2761 (2012) (cit. on pp. 27, 38, 56).

107. Wang, H.-W. *et al.* Broadband reflectance measurements of light penetration, blood oxygenation, hemoglobin concentration, and drug concentration in human intraperitoneal tissues before and after photodynamic therapy. *J. Biomed. Opt.* **10,** 14004 (2005) (cit. on pp. 27, 121, 145).

108. Zonios, G., Perelman, L. T., Backman, V., Manoharan, R., Fitzmaurice, M., Van Dam, J. & Feld, M. S. Diffuse reflectance spectroscopy of human adenomatous colon polyps in vivo. *Appl. Opt.* **38,** 6628 (1999) (cit. on pp. 27, 121).

109. Sunar, U., Makonnen, S., Zhou, C., Durduran, T., Yu, G., Wang, H.-W., Lee, W. M. & Yodh, A. G. Hemodynamic responses to antivascular therapy and ionizing radiation assessed by diffuse optical spectroscopies. *Opt. Express* **15,** 15507 (2007) (cit. on pp. 27, 70).

110. Diop, M., Kishimoto, J., Toronov, V., Lee, D. S. C. & St. Lawrence, K. Development of a combined broadband near-infrared and

diffusion correlation system for monitoring cerebral blood flow and oxidative metabolism in preterm infants. *Biomed. Opt. Express* **6,** 3907 (2015) (cit. on pp. 27, 56, 122).

111. Zhou, C. *et al.* Diffuse optical monitoring of blood flow and oxygenation in human breast cancer during early stages of neoadjuvant chemotherapy. *J. Biomed. Opt.* **12,** 051903 (2014) (cit. on p. 27).

112. Johansson, J. D., Mireles, M., Morales-Dalmau, J., Farzam, P., Martínez-Lozano, M., Casanovas, O. & Durduran, T. Scanning, non-contact, hybrid broadband diffuse optical spectroscopy and diffuse correlation spectroscopy system. *Biomed. Opt. Express* **7,** 481–98 (2016) (cit. on pp. 37, 121, 127, 133, 135, 137, 139–142, 156, 165).

113. Dehghani, H., Leblond, F., Pogue, B. W. & Chauchard, F. Application of spectral derivative data in visible and near-infrared spectroscopy. *Phys. Med. Biol.* **55,** 3381–3399 (2010) (cit. on pp. 37, 56).

114. Farzam, P. & Durduran, T. Multidistance diffuse correlation spectroscopy for simultaneous estimation of blood flow index and optical properties. *J. Biomed. Opt.* **20,** 055001 (2015) (cit. on p. 38).

115. Marois, M., Jacques, S. & Paulsen, K. Optimal wavelength selection for optical spectroscopy of hemoglobin and water within a simulated light-scattering tissue. English (US). *Journal of Biomedical Optics* **23** (July 2018) (cit. on p. 38).

116. Farzam, P., Tamborini, D., Zimmermann, B., Wu, K. C., Boas, D. A. & Franceschini, M. A. *Novel Diffuse Correlation Spectroscopy for Simulations Estimation of Hemoglobin Concentration, Oxygen saturation, and Blood flow* in *Biophotonics Congress: Biomedical Optics Congress 2018 (Microscopy/Translational/Brain/OTS)* (Optical Society of America, 2018), JTh3A.33 (cit. on p. 38).

117. Shah, N., Cerussi, A. E., Jakubowski, D., Hsiang, D., Butler, J. & Tromberg, B. J. Spatial variations in optical and physiological properties of healthy breast tissue. *J. Biomed. Opt.* **9,** 534 (2004) (cit. on p. 44).

118. Chen, Y. *et al.* Metabolism-enhanced tumor localization by fluorescence imaging: in vivo animal studies. *Opt. Lett.* **28,** 2070–2 (2003) (cit. on p. 44).

119. Fidler, I. J. Tumor heterogeneity and the biology of cancer invasion and metastasis. *Cancer Res.* **38,** 2651–60 (1978) (cit. on p. 44).

120. Reya, T., Morrison, S. J., Clarke, M. F. & Weissman, I. L. Stem cells, cancer, and cancer stem cells. *Nature* **414** (eds Teicher, B. A. & Bagley, R. G.) 105–11 (2001) (cit. on p. 44).

121. Cook, R. D. Detection of Influential Observation in Linear Regression. *Technometrics* **19,** 15 (1977) (cit. on p. 46).

122. Cook, R. D. & Weisberg, S. *Residuals and Influence in Regression* 413. ISBN: 041224280X (1982) (cit. on p. 46).

123. Jain, A. K. & Dubes, R. C. *Algorithms for Clustering Data (Prentice Hall Advanced Reference Series : Computer Science)* ISBN: 013022278X (Pearson College Div, 1988) (cit. on p. 50).

124. Jain, A. K., Murty, M. N. & Flynn, P. J. Data clustering: a review. *ACM Comput. Surv. Lecture Notes in Computer Science* **31** (eds Murgante, B., Misra, S., Rocha, A. M.A. C., Torre, C., Rocha, J. G., Falcão, M. I., Taniar, D., Apduhan, B. O. & Gervasi, O.) 264–323 (1999) (cit. on p. 50).

125. Fraley, C. How Many Clusters? Which Clustering Method? Answers Via Model-Based Cluster Analysis. *Comput. J.* **41,** 578–588 (1998) (cit. on p. 50).

126. Day, W. H. E. & Edelsbrunner, H. Efficient algorithms for agglomerative hierarchical clustering methods. *J. Classif.* **1,** 7–24 (1984) (cit. on p. 50).

127. Benesty, J., Chen, J., Huang, Y. & Cohen, I. *Pearson Correlation Coefficient* 1–4 (Springer Berlin Heidelberg, 2009) (cit. on p. 51).

128. Sokal, R. R. & Michener, C. D. *A Statistical Method for Evaluating Systematic Relationships* 1409–1438. ISBN: 0001948000237 (1958) (cit. on p. 51).

129. Mojena, R. Hierarchical grouping methods and stopping rules: an evaluation. *Comput. J.* **20,** 359–363 (1977) (cit. on p. 52).

130. Sebert, D. M., Montgomery, D. C. & Rollier, D. A. A clustering algorithm for identifying multiple outliers in linear regression. *Comput. Stat. Data Anal.* **27,** 461–484 (1998) (cit. on p. 53).

131. Arridge, S. R. & Lionheart, W. R. B. Nonuniqueness in diffusion-based optical tomography. *Opt. Lett.* **23,** 882 (1998) (cit. on p. 55).

132. Corlu, A., Durduran, T., Choe, R., Schweiger, M., Hillman, E. M. C., Arridge, S. R. & Yodh, A. G. Uniqueness and wavelength optimization in continuous-wave multispectral diffuse optical tomography. *Opt. Lett.* **28,** 2339–41 (2003) (cit. on p. 56).

133. Corlu, A., Choe, R., Durduran, T., Lee, K., Schweiger, M., Arridge, S. R., Hillman, E. M. C. & Yodh, A. G. Diffuse optical tomography with spectral constraints and wavelength optimization. *Appl. Opt.* **44,** 2082–93 (2005) (cit. on p. 56).

134. Eames, M. E., Wang, J., Pogue, B. W. & Dehghani, H. Wavelength band optimization in spectral near-infrared optical tomography improves accuracy while reducing data acquisition and computational burden. *J. Biomed. Opt.* **13,** 054037 (2008) (cit. on p. 56).

135. Srinivasan, S., Pogue, B. W., Jiang, S., Dehghani, H. & Paulsen, K. D. Spectrally constrained chromophore and scattering near-infrared tomography provides quantitative and robust reconstruction. *Appl. Opt.* **44,** 1858 (2005) (cit. on p. 56).

136. Xu, H., Pogue, B. W., Springett, R. & Dehghani, H. Spectral derivative based image reconstruction provides inherent insensitivity to coupling and geometric errors. *Opt. Lett.* **30,** 2912–2914 (2005) (cit. on p. 56).

137. Li, A., Zhang, Q., Culver, J. P., Miller, E. L. & Boas, D. a. Reconstructing chromosphere concentration images directly by continuous-wave diffuse optical tomography. *Opt. Lett.* **29,** 256 (2004) (cit. on p. 56).

138. Savitzky, A. & Golay, M. J. E. Smoothing and Differentiation of Data by Simplified Least Squares Procedures. *Anal. Chem.* **36,** 1627–1639 (1964) (cit. on p. 58).

139. Dong, L., He, L., Lin, Y., Shang, Y. & Yu, G. Simultaneously Extracting Multiple Parameters via Fitting One Single Autocorrelation Function Curve in Diffuse Correlation Spectroscopy. *IEEE Trans. Biomed. Eng.* **60,** 361–368 (2013) (cit. on p. 63).

140. Carmeliet, P. & Jain, R. K. Angiogenesis in cancer and other diseases. *Nature* **407,** 249–57 (2000) (cit. on p. 69).

141. Folkman, J. What Is the Evidence That Tumors Are Angiogenesis Dependent? *JNCI J. Natl. Cancer Inst.* **82,** 4–7 (1990) (cit. on p. 69).

142. Folkman, J. Angiogenesis in cancer, vascular, rheumatoid and other disease. *Nat. Med.* **1,** 27–30 (1995) (cit. on p. 69).

143. Valastyan, S. & Weinberg, R. A. Tumor Metastasis: Molecular Insights and Evolving Paradigms. *Cell* **147,** 275–292 (2011) (cit. on p. 69).

144. Ferrara, N. VEGF and the quest for tumour angiogenesis factors. *Nat. Rev. Cancer* **2,** 795–803 (2002) (cit. on pp. 69, 93).

145. Neufeld, G, Cohen, T, Gengrinovitch, S & Poltorak, Z. Vascular endothelial growth factor (VEGF) and its receptors. *FASEB J.* **13,** 9–22 (1999) (cit. on pp. 69, 96).

146. Folkman, J. Angiogenesis: an organizing principle for drug discovery? *Nat. Rev. Drug Discov.* **6,** 273–286 (2007) (cit. on p. 69).

147. Hlatky, L. Clinical Application of Antiangiogenic Therapy: Microvessel Density, What It Does and Doesn't Tell Us. *CancerSpectrum Knowl. Environ.* **94,** 883–893 (2002) (cit. on p. 69).

148. Rini, B. I. Vascular endothelial growth factor-targeted therapy in metastatic renal cell carcinoma. *Cancer* **115,** 2306–2312 (2009) (cit. on p. 69).

149. Grimaldi, A., Guida, T., D'Attino, R., Perrotta, E., Otero, M., Masala, A. & Carteni, G. Sunitinib: bridging present and future cancer treatment. *Ann. Oncol.* **18,** vi31–vi34 (2007) (cit. on pp. 69, 93).

150. Pichler, R. & Heidegger, I. Novel concepts of antiangiogenic therapies in metastatic renal cell cancer. *memo - Mag. Eur. Med. Oncol.* **10,** 206–212 (2017) (cit. on p. 69).

151. De Bock, K., Mazzone, M. & Carmeliet, P. Antiangiogenic therapy, hypoxia and metastasis: risky liaisons, or not? *Nat. Rev. Clin. Oncol.* **8,** 393–404 (2011) (cit. on p. 69).

152. Bergers, G. & Hanahan, D. Modes of resistance to anti-angiogenic therapy. *Nat. Rev. Cancer* **8,** 592–603 (2008) (cit. on pp. 69, 93, 94).

153. Casanovas, O., Hicklin, D. J., Bergers, G. & Hanahan, D. Drug resistance by evasion of antiangiogenic targeting of VEGF signaling in late-stage pancreatic islet tumors. *Cancer Cell* **8,** 299–309 (2005) (cit. on p. 69).

154. Kerbel, R. & Folkman, J. Clinical translation of angiogenesis inhibitors. *Nat. Rev. Cancer* **2,** 727–739 (2002) (cit. on p. 69).

155. Pàez-Ribes, M., Allen, E., Hudock, J., Takeda, T., Okuyama, H., Viñals, F., Inoue, M., Bergers, G., Hanahan, D. & Casanovas, O. Antiangiogenic Therapy Elicits Malignant Progression of Tumors to Increased Local Invasion and Distant Metastasis. *Cancer Cell* **15,** 220–231 (2009) (cit. on p. 69).

156. Rini, B. I. & Atkins, M. B. Resistance to targeted therapy in renal-cell carcinoma. *Lancet Oncol.* **10,** 992–1000 (2009) (cit. on pp. 70, 94).

157. Sessa, C., Guibal, A., Del Conte, G. & Rüegg, C. Biomarkers of angiogenesis for the development of antiangiogenic therapies in oncology: tools or decorations? *Nat. Clin. Pract. Oncol.* **5,** 378–391 (2008) (cit. on p. 70).

158. Sawyers, C. Targeted cancer therapy. *Nature* **432,** 294–297 (2004) (cit. on p. 70).

159. Jain, R. K., Duda, D. G., Willett, C. G., Sahani, D. V., Zhu, A. X., Loeffler, J. S., Batchelor, T. T. & Sorensen, A. G. Biomarkers of response and resistance to antiangiogenic therapy. *Nat. Rev. Clin. Oncol.* **6,** 327–38 (2009) (cit. on p. 70).

160. Ramirez, G *et al.* Chemotherapeutic drug-specific alteration of microvascular blood flow in murine breast cancer as measured by diffuse correlation spectroscopy. *Biomed. Opt. Express* **7,** 3610 (2016) (cit. on pp. 70, 122).

161. Menon, C. *et al.* An integrated approach to measuring tumor oxygen status using human melanoma xenografts as a model. *Cancer Res.* **63,** 7232–40 (2003) (cit. on pp. 70, 119).

162. Capellá, G, Farré, L, Villanueva, A, Reyes, G, García, C, Tarafa, G & Lluís, F. Orthotopic models of human pancreatic cancer. *Ann. N. Y. Acad. Sci.* **880,** 103–9 (1999) (cit. on pp. 71, 93).

163. Reyes, G., Villanueva, A., García, C., Sancho, F. J., Piulats, J., Lluís, F. & Capellá, G. Orthotopic xenografts of human pancreatic carcinomas acquire genetic aberrations during dissemination in nude mice. *Cancer Res.* **56,** 5713–9 (1996) (cit. on pp. 71, 93).

164. Garber, K. Personal Mouse Colonies Give Hope for Pancreatic Cancer Patients. *JNCI J. Natl. Cancer Inst.* **99,** 105–107 (2007) (cit. on pp. 71, 93).

165. R Core Team. *R: A Language and Environment for Statistical Computing* R Foundation for Statistical Computing (Vienna, Austria, 2016) (cit. on pp. 75, 109).

166. Busch, D. R. *et al.* Computer aided automatic detection of malignant lesions in diffuse optical mammography. *Med. Phys.* **37,** 1840–1849 (2010) (cit. on p. 85).

167. Vickers, M. M. *et al.* Clinical Outcome in Metastatic Renal Cell Carcinoma Patients After Failure of Initial Vascular Endothelial Growth Factor-Targeted Therapy. *Urology* **76,** 430–434 (2010) (cit. on p. 93).

168. Busch, J., Seidel, C., Weikert, S., Wolff, I., Kempkensteffen, C., Weinkauf, L., Hinz, S., Magheli, A., Miller, K. & Grünwald, V. Intrinsic resistance to tyrosine kinase inhibitors is associated with poor clinical outcome in metastatic renal cell carcinoma. *BMC Cancer* **11,** 295 (2011) (cit. on p. 93).

169. Huang, D., Ding, Y., Zhou, M., Rini, B. I., Petillo, D., Qian, C.-N., Kahnoski, R., Futreal, P. A., Furge, K. A. & Teh, B. T. Interleukin-8 Mediates Resistance to Antiangiogenic Agent Sunitinib in Renal Cell Carcinoma. *Cancer Res.* **70,** 1063–1071 (2010) (cit. on pp. 93, 96).

170. Takahashi, A, Sasaki, H, Kim, S. J., Tobisu, K, Kakizoe, T, Tsukamoto, T, Kumamoto, Y, Sugimura, T & Terada, M. Markedly increased amounts of messenger RNAs for vascular endothelial growth factor and placenta growth factor in renal cell carcinoma associated with angiogenesis. *Cancer Res.* **54,** 4233–7 (1994) (cit. on p. 94).

171. Tran, W. T. *et al.* Predicting breast cancer response to neoadjuvant chemotherapy using pretreatment diffuse optical spectroscopic texture analysis. *Br. J. Cancer* **116,** 1329–1339 (2017) (cit. on p. 95).

172. Zhou, Q., Guo, P. & Gallo, J. M. Impact of Angiogenesis Inhibition by Sunitinib on Tumor Distribution of Temozolomide. *Clin. Cancer Res.* **14,** 1540–1549 (2008) (cit. on p. 96).

173. Ferrara, N. & Davis-Smyth, T. The Biology of Vascular Endothelial Growth Factor. *Endocr. Rev.* **18,** 4–25 (1997) (cit. on p. 96).

174. Sunar, U. *et al.* Noninvasive diffuse optical measurement of blood flow and blood oxygenation for monitoring radiation therapy in patients with head and neck tumors: a pilot study. *J. Biomed. Opt.* **11,** 064021 (2006) (cit. on p. 97).

175. Dong, L. *et al.* Diffuse optical measurements of head and neck tumor hemodynamics for early prediction of chemoradiation therapy outcomes. *J. Biomed. Opt.* **21,** 085004 (2016) (cit. on p. 97).

176. Yu, G., Durduran, T., Zhou, C., Zhu, T. C., Finlay, J. C., Busch, T. M., Malkowicz, S. B., Hahn, S. M. & Yodh, A. G. Real-time In Situ Monitoring of Human Prostate Photodynamic Therapy with Diffuse Light. *Photochem. Photobiol.* **82,** 1279 (2006) (cit. on p. 97).

177. Choe, R. & Durduran, T. Diffuse Optical Monitoring of the Neoadjuvant Breast Cancer Therapy. *IEEE J. Sel. Top. Quantum Electron.* **18,** 1367–1386 (2012) (cit. on p. 97).

178. Zhou, C. *et al.* Diffuse optical monitoring of blood flow and oxygenation in human breast cancer during early stages of neoadjuvant chemotherapy. *J. Biomed. Opt.* **12,** 051903 (2007) (cit. on p. 97).

179. Eustis, S. & El-Sayed, M. A. Why gold nanoparticles are more precious than pretty gold: Noble metal surface plasmon resonance and its enhancement of the radiative and nonradiative properties of nanocrystals of different shapes. *Chem. Soc. Rev.* **35,** 209–217 (2006) (cit. on p. 100).

180. Daniel, M.-C. & Astruc, D. Gold nanoparticles: assembly, supramolecular chemistry, quantum-size-related properties, and applications toward biology, catalysis, and nanotechnology. *Chem. Rev.* **104,** 293–346 (2004) (cit. on p. 100).

181. Jain, K. K. in *Adv. Exp. Med. Biol.* 37–43 (2009). ISBN: 9781441911315 (cit. on p. 100).

182. Zhang, L, Gu, F., Chan, J., Wang, A., Langer, R. & Farokhzad, O. Nanoparticles in Medicine: Therapeutic Applications and Developments. *Clin. Pharmacol. Ther.* **83,** 761–769 (2008) (cit. on p. 100).

183. Boisselier, E. & Astruc, D. Gold nanoparticles in nanomedicine: preparations, imaging, diagnostics, therapies and toxicity. *Chem. Soc. Rev.* **38,** 1759 (2009) (cit. on p. 100).

184. Dreaden, E. C., Alkilany, A. M., Huang, X., Murphy, C. J. & El-Sayed, M. A. The golden age: gold nanoparticles for biomedicine. *Chem. Soc. Rev.* **41,** 2740–2779 (2012) (cit. on p. 100).

185. Yeh, Y.-C., Creran, B. & Rotello, V. M. Gold nanoparticles: preparation, properties, and applications in bionanotechnology. *Nanoscale* **4,** 1871–1880 (2012) (cit. on p. 100).

186. Sperling, R. A., Rivera Gil, P., Zhang, F., Zanella, M. & Parak, W. J. Biological applications of gold nanoparticles. *Chem. Soc. Rev.* **37,** 1896 (2008) (cit. on p. 100).

187. Huang, X., Jain, P. K., El-Sayed, I. H. & El-Sayed, M. A. Gold nanoparticles: interesting optical properties and recent applications in cancer diagnostics and therapy. *Nanomedicine* **2,** 681–693 (2007) (cit. on p. 100).

188. Cai, W. Applications of gold nanoparticles in cancer nanotechnology. *Nanotechnol. Sci. Appl.* **Volume 1,** 17–32 (2008) (cit. on p. 100).

189. Jain, S, Hirst, D. G. & O'Sullivan, J. M. Gold nanoparticles as novel agents for cancer therapy. *Br. J. Radiol.* **85,** 101–113 (2012) (cit. on p. 100).

190. Brigger, I., Dubernet, C. & Couvreur, P. Nanoparticles in cancer therapy and diagnosis. *Adv. Drug Deliv. Rev.* **64,** 24–36 (2012) (cit. on p. 100).

191. Dreaden, E. C., Austin, L. A., Mackey, M. A. & El-Sayed, M. A. Size matters: gold nanoparticles in targeted cancer drug delivery. *Ther. Deliv.* **3,** 457–478 (2012) (cit. on p. 100).

192. Wilhelm, S. *et al.* Analysis of nanoparticle delivery to tumours. *Nat. Rev. Mater.* **1,** 16014 (2016) (cit. on pp. 100, 118, 119).

193. Maeda, H., Wu, J., Sawa, T., Matsumura, Y. & Hori, K. Tumor vascular permeability and the EPR effect in macromolecular therapeutics: A review. *J. Control. Release* **65,** 271–284 (2000) (cit. on pp. 100, 118).

194. Maeda, H. Macromolecular therapeutics in cancer treatment: The EPR effect and beyond. *J. Control. Release* **164,** 138–144 (2012) (cit. on p. 100).

195. Niidome, T., Yamagata, M., Okamoto, Y., Akiyama, Y., Takahashi, H., Kawano, T., Katayama, Y. & Niidome, Y. PEG-modified gold nanorods with a stealth character for in vivo applications. *J. Control. Release* **114,** 343–347 (2006) (cit. on pp. 100, 117, 118).

196. Huang, X., Peng, X., Wang, Y., Wang, Y., Shin, D. M., El-Sayed, M. A. & Nie, S. A reexamination of active and passive tumor targeting by using rod-shaped gold nanocrystals and covalently conjugated peptide ligands. *ACS Nano* **4,** 5887–96 (2010) (cit. on p. 100).

197. Gao, H. Progress and perspectives on targeting nanoparticles for brain drug delivery. *Acta Pharm. Sin. B* **6,** 268–286 (2016) (cit. on p. 100).

198. Gu, F. X., Karnik, R., Wang, A. Z., Alexis, F., Levy-Nissenbaum, E., Hong, S., Langer, R. S. & Farokhzad, O. C. Targeted nanoparticles for cancer therapy. *Nano Today* **2,** 14–21 (2007) (cit. on p. 100).

199. Wei, X., Chen, X., Ying, M. & Lu, W. Brain tumor-targeted drug delivery strategies. *Acta Pharm. Sin. B* **4,** 193–201 (2014) (cit. on p. 100).

200. Brannon-Peppas, L. & Blanchette, J. O. Nanoparticle and targeted systems for cancer therapy. *Adv. Drug Deliv. Rev.* **64,** 206–212 (2012) (cit. on p. 100).

201. Peer, D., Karp, J. M., Hong, S., Farokhzad, O. C., Margalit, R. & Langer, R. Nanocarriers as an emerging platform for cancer therapy. *Nat. Nanotechnol.* **2,** 751–760 (2007) (cit. on p. 100).

202. Haley, B. & Frenkel, E. Nanoparticles for drug delivery in cancer treatment. *Urol. Oncol. Semin. Orig. Investig.* **26,** 57–64 (2008) (cit. on p. 100).

203. De Jong, W. H. & Borm, P. J. A. Drug delivery and nanoparticles:applications and hazards. *Int. J. Nanomedicine* **3,** 133–49 (2008) (cit. on p. 100).

204. Amendola, V., Pilot, R., Frasconi, M., Maragò, O. M. & Iatì, M. A. Surface plasmon resonance in gold nanoparticles: a review. *J. Phys. Condens. Matter* **29,** 203002 (2017) (cit. on p. 100).

205. Govorov, A. O. & Richardson, H. H. Generating heat with metal nanoparticles. *Nano Today* **2,** 30–38 (2007) (cit. on p. 100).

206. Shilo, M., Reuveni, T., Motiei, M. & Popovtzer, R. Nanoparticles as computed tomography contrast agents: current status and future perspectives. *Nanomedicine* **7,** 257–269 (2012) (cit. on p. 100).

207. Zhang, Q., Iwakuma, N., Sharma, P., Moudgil, B. M., Wu, C., McNeill, J., Jiang, H. & Grobmyer, S. R. Gold nanoparticles as a contrast agent for in vivo tumor imaging with photoacoustic tomography. *Nanotechnology* **20,** 395102 (2009) (cit. on p. 100).

208. Blasiak, B., van Veggel, F. C.J. M. & Tomanek, B. Applications of Nanoparticles for MRI Cancer Diagnosis and Therapy. *J. Nanomater.* **2013,** 1–12 (2013) (cit. on p. 100).

209. Li, W. & Chen, X. Gold nanoparticles for photoacoustic imaging. *Nanomedicine* **10,** 299–320 (2015) (cit. on p. 100).

210. Park, J. *et al.* Two-photon-induced photoluminescence imaging of tumors using near-infrared excited gold nanoshells. *Opt. Express* **16,** 1590–9 (2008) (cit. on p. 100).

211. Hainfeld, J. F., Slatkin, D. N., Focella, T. M. & Smilowitz, H. M. Gold nanoparticles: a new X-ray contrast agent. *Br. J. Radiol.* **79,** 248–253 (2006) (cit. on p. 100).

212. Yang, X., Stein, E. W., Ashkenazi, S. & Wang, L. V. Nanoparticles for photoacoustic imaging. *Wiley Interdiscip. Rev. Nanomedicine Nanobiotechnology* **1,** 360–368 (2009) (cit. on p. 100).

213. Huang, X., El-Sayed, I. H., Qian, W. & El-Sayed, M. a. Cancer Cell Imaging and Photothermal Therapy in the Near-Infrared Region by Using Gold Nanorods. *J. Am. Chem. Soc.* **128,** 2115–2120 (2006) (cit. on p. 100).

214. Wang, Y. *et al.* Comparison Study of Gold Nanohexapods, Nanorods, and Nanocages for Photothermal Cancer Treatment. *ACS Nano* **7,** 2068–2077 (2013) (cit. on pp. 100, 117).

215. Mackey, M. A., Ali, M. R. K., Austin, L. A., Near, R. D. & El-Sayed, M. A. The Most Effective Gold Nanorod Size for Plasmonic Photothermal Therapy: Theory and In Vitro Experiments. *J. Phys. Chem. B* **118,** 1319–1326 (2014) (cit. on p. 100).

216. Morales-Dalmau, J., Vilches, C., De Miguel, I., Sanz, V. & Quidant, R. Optimum morphology of gold nanorods for light-induced hyperthermia. *Nanoscale* (2017) (cit. on p. 100).

217. Guo, J., Rahme, K., He, Y., Li, L.-L., Holmes, J. & O'Driscoll, C. Gold nanoparticles enlighten the future of cancer theranostics. *Int. J. Nanomedicine* **Volume 12,** 6131–6152 (2017) (cit. on p. 100).

218. Akhter, S., Ahmad, M. Z., Ahmad, F. J., Storm, G. & Kok, R. J. Gold nanoparticles in theranostic oncology: current state-of-the-art. *Expert Opin. Drug Deliv.* **9,** 1225–1243 (2012) (cit. on p. 100).

219. Hornos Carneiro, M. F. & Barbosa, F. Gold nanoparticles: A critical review of therapeutic applications and toxicological aspects. *J. Toxicol. Environ. Heal. Part B* **19,** 129–148 (2016) (cit. on p. 101).

220. Khlebtsov, N. & Dykman, L. Biodistribution and toxicity of engineered gold nanoparticles: a review of in vitro and in vivo studies. *Chem. Soc. Rev.* **40,** 1647–1671 (2011) (cit. on p. 101).

221. Elsaesser, A. & Howard, C. V. Toxicology of nanoparticles. *Adv. Drug Deliv. Rev.* **64,** 129–137 (2012) (cit. on p. 101).

222. Nikoobakht, B. & El-Sayed, M. A. Preparation and Growth Mechanism of Gold Nanorods (NRs) Using Seed-Mediated Growth Method. *Chem. Mater.* **15,** 1957–1962 (2003) (cit. on p. 102).

223. Pérez-Juste, J, Pastoriza-Santos, I, Liz-Marzán, L & Mulvaney, P. Gold nanorods: Synthesis, characterization and applications. *Coord. Chem. Rev.* **249,** 1870–1901 (2005) (cit. on p. 102).

224. Williams, D. B. & Carter, C. B. *Transmission Electron Microscopy* (Springer US, 2009) (cit. on p. 103).

225. Greenfield, S. Inductively coupled plasmas in atomic fluorescence spectrometry. A review. *J. Anal. At. Spectrom.* **9,** 565 (1994) (cit. on pp. 109, 110).

226. Martin, R. F. General deming regression for estimating systematic bias and its confidence interval in method-comparison studies. *Clin. Chem.* **46,** 100–4 (2000) (cit. on pp. 109, 110).

227. Akiyama, Y., Mori, T., Katayama, Y. & Niidome, T. The effects of PEG grafting level and injection dose on gold nanorod biodistribution in the tumor-bearing mice. *J. Control. Release* **139,** 81–84 (2009) (cit. on p. 118).

228. Mesquita, R. C., Durduran, T., Yu, G., Buckley, E. M., Kim, M. N., Zhou, C., Choe, R., Sunar, U. & Yodh, A. G. Direct measurement of tissue blood flow and metabolism with diffuse optics. *Philos. Trans. A. Math. Phys. Eng. Sci.* **369,** 4390–406 (2011) (cit. on p. 121).

229. Hirosawa, N., Sakamoto, Y., Katayama, H., Tonooka, S. & Yano, K. In vivo investigation of progressive alterations in rat mammary gland tumors by near-infrared spectroscopy. *Anal. Biochem.* **305,** 156–65 (2002) (cit. on p. 121).

230. Buckley, E. M., Patel, S. D., Miller, B. F., Franceschini, M. A. & Vannucci, S. J. In vivo Monitoring of Cerebral Hemodynamics in the Immature Rat: Effects of Hypoxia-Ischemia and Hypothermia. *Dev. Neurosci.* **37,** 407–416 (2015) (cit. on p. 122).

231. Buckley, E. M., Miller, B. F., Golinski, J. M., Sadeghian, H., McAllister, L. M., Vangel, M., Ayata, C., Meehan, W. P., Franceschini, M. A. & Whalen, M. J. Decreased Microvascular Cerebral Blood Flow Assessed by Diffuse Correlation Spectroscopy after Repetitive Concussions in Mice. *J. Cereb. Blood Flow Metab.* **35,** 1995–2000 (2015) (cit. on p. 122).

232. Cheng, R., Zhang, X., Daugherty, A., Shin, H. & Yu, G. Noninvasive quantification of postocclusive reactive hyperemia in mouse thigh muscle by near-infrared diffuse correlation spectroscopy. *Appl. Opt.* **52,** 7324–30 (2013) (cit. on p. 122).

233. Giovannella, M., Ibañez, D., Gregori-Pla, C. & Kacprzak, M. Concurrent measurement of cerebral hemodynamics and electroencephalography during transcranial direct current stimulation. *Neurophotonics* **5,** 1 (2018) (cit. on p. 122).

234. Lindner, C., Mora, M., Farzam, P., Squarcia, M., Johansson, J., Weigel, U. M., Halperin, I., Hanzu, F. A. & Durduran, T. Diffuse Optical Characterization of the Healthy Human Thyroid Tissue and Two Pathological Case Studies. *PLoS One* **11** (ed Georgakoudi, I.) e0147851 (2016) (cit. on p. 122).

235. Mesquita, R. C., Skuli, N., Kim, M. N., Liang, J., Schenkel, S., Majmundar, A. J., Simon, M. C. & Yodh, A. G. Hemodynamic and metabolic diffuse optical monitoring in a mouse model of

hindlimb ischemia. *Biomed. Opt. Express* **1,** 1173–1187 (2010) (cit. on p. 122).

236. Cheung, C, Culver, J. P., Takahashi, K, Greenberg, J. H. & Yodh, a. G. In vivo cerebrovascular measurement combining diffuse near-infrared absorption and correlation spectroscopies. *Phys. Med. Biol.* **46,** 2053–65 (2001) (cit. on p. 122).

237. Culver, J. P., Durduran, T., Cheung, C., Furuya, D., Greenberg, J. H. & Yodh, A. G. Diffuse optical measurement of hemoglobin and cerebral blood flow in rat brain during hypercapnia, hypoxia and cardiac arrest. *Adv. Exp. Med. Biol.* **510,** 293–7 (2003) (cit. on p. 122).

238. Culver, J. P., Durduran, T., Furuya, D., Cheung, C., Greenberg, J. H. & Yodh, A. G. Diffuse optical tomography of cerebral blood flow, oxygenation, and metabolism in rat during focal ischemia. *J. Cereb. Blood Flow Metab.* **23,** 911–24 (2003) (cit. on p. 122).

239. Zhou, C., Yu, G., Furuya, D., Greenberg, J. H., Yodh, A. G. & Durduran, T. Diffuse optical correlation tomography of cerebral blood flow during cortical spreading depression in rat brain. *Opt. Express* **14,** 1125 (2006) (cit. on p. 122).

240. Li, T., Lin, Y., Shang, Y., He, L., Huang, C., Szabunio, M. & Yu, G. Simultaneous measurement of deep tissue blood flow and oxygenation using noncontact diffuse correlation spectroscopy flow-oximeter. *Sci. Rep.* **3,** 1358 (2013) (cit. on p. 122).

241. Becker, T. L., Paquette, A. D., Keymel, K. R., Henderson, B. W. & Sunar, U. Monitoring blood flow responses during topical ALA-PDT. *Biomed. Opt. Express* **2,** 123–130 (2010) (cit. on p. 122).

242. Han, S., Johansson, J., Mireles, M., Proctor, A. R., Hoffman, M. D., Vella, J. B., Benoit, D. S. W., Durduran, T. & Choe, R. Non-contact scanning diffuse correlation tomography system for three-dimensional blood flow imaging in a murine bone graft model. *Biomed. Opt. Express* **6,** 2695–712 (2015) (cit. on pp. 122, 143).

243. Kester, R. T., Bedard, N., Gao, L. & Tkaczyk, T. S. Real-time snapshot hyperspectral imaging endoscope. *J. Biomed. Opt.* **16,** 056005 (2011) (cit. on p. 122).

244. Zuzak, K. J., Hariharan, S., Naik, S. C., Mandhale, M. & Livingston, E. H. *A Near-Infrared Hyperspectral Imaging System for Monitoring Wound Healing Post Amputation* in *2007 IEEE Dallas Eng. Med. Biol. Work.* (IEEE, 2007), 9–11. ISBN: 978-1-4244-1626-4 (cit. on p. 122).

245. Zuzak, K. J., Schaeberle, M. D., Lewis, E. N. & Levin, I. W. Visible Reflectance Hyperspectral Imaging: Characterization of a Noninvasive, in Vivo System for Determining Tissue Perfusion. *Anal. Chem.* **74,** 2021–2028 (2002) (cit. on p. 122).

246. Zuzak, K. J., Naik, S. C., Alexandrakis, G., Hawkins, D., Behbehani, K. & Livingston, E. H. Characterization of a Near-Infrared Laparoscopic Hyperspectral Imaging System for Minimally Invasive Surgery. *Anal. Chem.* **79,** 4709–4715 (2007) (cit. on p. 122).

247. Panasyuk, S. V., Yang, S., Faller, D. V., Ngo, D., Lew, R. A., Freeman, J. E. & Rogers, A. E. Medical hyperspectral imaging to facilitate residual tumor identification during surgery. *Cancer Biol. Ther.* **6,** 439–446 (2007) (cit. on p. 122).

248. Akbari, H., Halig, L. V., Schuster, D. M., Osunkoya, A., Master, V., Nieh, P. T., Chen, G. Z. & Fei, B. Hyperspectral imaging and quantitative analysis for prostate cancer detection. *J. Biomed. Opt.* **17,** 0760051 (2012) (cit. on p. 122).

249. Spinelli, L. *et al.* Determination of reference values for optical properties of liquid phantoms based on Intralipid and India ink. *Biomed. Opt. Express* **5,** 2037 (2014) (cit. on p. 128).

250. Cortese, L. *et al.* Liquid phantoms for near-infrared and diffuse correlation spectroscopies with tunable optical and dynamic properties. *Biomed. Opt. Express* **9,** 2068 (2018) (cit. on p. 130).

251. Bezemer, R., Lima, A., Myers, D., Klijn, E., Heger, M., Goedhart, P. T., Bakker, J. & Ince, C. Assessment of tissue oxygen saturation during a vascular occlusion test using near-infrared spectroscopy: the role of probe spacing and measurement site studied in healthy volunteers. *Crit. Care* **13,** S4 (2009) (cit. on pp. 138, 145).

252. Ferrari, M., Muthalib, M. & Quaresima, V. The use of near-infrared spectroscopy in understanding skeletal muscle physiology: recent developments. *Philos. Trans. R. Soc. A Math. Phys. Eng. Sci.* **369,** 4577–4590 (2011) (cit. on pp. 138, 145).

253. Yu, G., Floyd, T. F., Durduran, T., Zhou, C., Wang, J., Detre, J. A. & Yodh, A. G. Validation of diffuse correlation spectroscopy for muscle blood flow with concurrent arterial spin labeled perfusion MRI. *Opt. Express* **15,** 1064 (2007) (cit. on pp. 138, 145).

254. Hillman, E. M. C., Boas, D. A., Dale, A. M. & Dunn, A. K. Laminar optical tomography: demonstration of millimeter-scale depth-resolved imaging in turbid media. *Opt. Lett.* **29,** 1650 (2004) (cit. on p. 143).

255. Wardell, K., Jakobsson, A & Nilsson, G. Laser Doppler perfusion imaging by dynamic light scattering. *IEEE Trans. Biomed. Eng.* **40,** 309–316 (1993) (cit. on p. 143).

256. Giannoni, L., Lange, F. & Tachtsidis, I. Hyperspectral imaging solutions for brain tissue metabolic and hemodynamic monitoring: past, current and future developments. *J. Opt.* **20,** 044009 (2018) (cit. on p. 143).

257. Foschum, F, Jäger, M & Kienle, A. Fully automated spatially resolved reflectance spectrometer for the determination of the absorption and scattering in turbid media. *Rev. Sci. Instrum.* **82,** 103104 (2011) (cit. on p. 144).

258. Zong, Y., Brown, S. W., Johnson, B. C., Lykke, K. R. & Ohno, Y. Simple spectral stray light correction method for array spectroradiometers. *Appl. Opt.* **45,** 1111–9 (2006) (cit. on p. 144).

259. Johansson, J, Mireles, M, Farzam, P & Durduran, T. Practical height correction for diffuse optical spectroscopy to account for curved tissue surfaces. *Biomed. Opt. 2014,* BS3A.5 (2014) (cit. on p. 145).

260. Beop-Min Kim, Jacques, S., Rastegar, S., Thomsen, S. & Motamedi, M. Nonlinear finite-element analysis of the role of dynamic changes in blood perfusion and optical properties in laser coagulation of tissue. *IEEE J. Sel. Top. Quantum Electron.* **2,** 922–933 (1996) (cit. on p. 145).

261. Hull, E. L. & Foster, T. H. Steady-state reflectance spectroscopy in the P3 approximation. *J. Opt. Soc. Am. A* **18,** 584 (2001) (cit. on p. 145).

262. Nitzan, M., Babchenko, A., Khanokh, B. & Taitelbaum, H. Measurement of oxygen saturation in venous blood by dynamic near infrared spectroscopy. *J. Biomed. Opt.* **5,** 155 (2000) (cit. on p. 145).

263. Bergersen, T. K., Eriksen, M & Walløe, L. Local constriction of arteriovenous anastomoses in the cooled finger. *Am. J. Physiol.* **273,** R880–R886 (1997) (cit. on p. 145).

264. Baran, T. M., Wilson, J. D., Mitra, S., Yao, J. L., Messing, E. M., Waldman, D. L. & Foster, T. H. Optical property measurements establish the feasibility of photodynamic therapy as a minimally invasive intervention for tumors of the kidney. *J. Biomed. Opt.* **17,** 0980021 (2012) (cit. on p. 145).

265. Xia, J., Berg, E., Lee, J. & Yao, G. Characterizing beef muscles with optical scattering and absorption coefficients in VIS-NIR region. *Meat Sci.* **75,** 78–83 (2007) (cit. on p. 145).

266. Simonnet, H., Alazard, N., Pfeiffer, K., Gallou, C., Béroud, C., Demont, J., Bouvier, R., Schägger, H. & Godinot, C. Low mitochondrial respiratory chain content correlates with tumor aggressiveness in renal cell carcinoma. *Carcinogenesis* **23,** 759–68 (2002) (cit. on p. 145).